JAERI-M
8890

POWER BALANCE IN THE DIVERTOR-TOKAMAK DIVA

June 1980

Haruyuki KIMURA

日本原子力研究所
Japan Atomic Energy Research Institute

JAERI-M 8890

Power Balance in the Divertor-Tokamak DIVA

Haruyuki KIMURA

Division of Thermonuclear Fusion Research
Tokai Research Establishment, JAERI
(Received May 8, 1980)

Power balances of Ohmically and radio-frequency (RF) heated plasmas including a boundary (scrape-off layer) plasma are investigated in the divertor-tokamak DIVA.

First, methods of measurement of the boudary plasma are described. These are applied to the divertor plasma in the case of Ohmic heating. The results clarify characteristics of the boudary plasma of a conventional tokamak.

The scaling law for the boudary plasma is derived in consideration of the power balance including the boudary plasma. Heat flux to material surfaces is investigated in detail; the relationship between heat flux, particle flux and electron velocity distribution is clarified. Gross power balance is investigated by measurements of total heat flux to the wall and total radiation loss including charge-exchange loss. These results provide experimental evidence for the above scaling law.

Finally, power balance during the Ion-Cyclotron Range of Frequency (ICRF) heating is described. Optimum heating conditions of the ICRF heating in the two-ion hybrid regime are surveyed. For the optimum heating conditions, gross power balance including the boudary plasma is considered, in which the heating efficiency is derived. Radial profile of the RF-heating power, the ratio of the heating power to each species and the transport of RF-heated ions are clarified in the power balance.

Keywords: DIVA Tokamak, Divertor, Ohmic Heating, Power Balance, Scrape-off Layer, Heat Flux, Radiation Loss, Charge-exchange Loss, ICRF Heating, Two-ion Hybrid.

JAERI−M　8890

ダイバーター付きトカマクDIVAに於けるパワーバランス

日本原子力研究所東海研究所核融合研究部
木村　晴行

（1980年5月8日受理）

ダイバーター付きトカマクDIVAに於ける，オーム加熱時及び高周波加熱時の周辺（スクレープ・オフ層）プラズマを含めたパワーバランスについて述べる。

まず，周辺プラズマの計測方法について述べ，オーム加熱の場合にこれ等をダイバータープラズマに適用し，得られた測定結果から通常のトカマクの周辺プラズマの性質を明らかにする。

周辺プラズマの比例則を，周辺プラズマを含めたパワーバランスの考察から導く。金属壁へのプラズマの熱流束を詳細に調べ，熱流束と粒子束，粒子の速度分布との関係を示す。また，壁への全熱流束及び荷電交換損失を含めた全放射損失の測定により，全体のパワーバランスを明らかにする。これ等の結果は，上記の周辺プラズマの比例則に実験的根拠を与えるものである。

最後に，イオン−サイクロトロン周波数帯（ICRF）加熱の場合のパワーバランスについて述べる。まず，2−イオン・ハイブリッド領域でのICRF加熱の最適条件を明らかにする。次いで，最適な加熱条件に対して，周辺プラズマを含めたパワーバランスを考察し，加熱効率を導く。高周波パワーの径方向分布，各成分粒子への加熱パワーの比率及び加熱時のイオンの輸送をパワーバランスの観点から明らかにする。

CONTENTS

目　　次

1. INTRODUCTION

1.1 Present Status of the Tokamak Fusion Research

As the key subjects of the present-day tokamak fusion research [1], the following items are mentioned:

(1) Impurity control,
(2) Additional plasma heating,
(3) Stability of high-β plasma,

where β is (plasma internal energy)/(toroidal magnetic pressure).

Impurities such as O, C, N (light impurity), and Fe, Cr, Mo, W (metal impurity) give serious effects to the plasma confinement in the form of the radiation loss, i.e. the disruptive instability [2], the hollow-profile of the electron temperature [3] and a short confinement time, etc. The allowable density ratio of impurities in a self-sustaining fusion reactor is 3 ∿ 5 % for a light impurity and 0.1 ∿ 0.01 % for a metal impurity [4]. Therefore, intensive investigations have been concentrated to solve the impurity problem in the tokamaks of the world. The following results have been obtained: The light impurities are easily removed by baking of the vacuum vessel, the low temperature discharge cleaning (TDC) [5] and the Ti-gettering of the first wall [6]. The origin of metal impurities is due to sputtering by impurity ions accelerated by the sheath potential between a plasma and a wall [7]. Hence, it is necessary to reduce the electron temperature of the surface plasma in order to eliminate the metal impurity. A carbon-coated wall is proposed for the next-generation large machine [8].

It has been demonstrated that a divertor is useful to control impurities in DIVA [9] and DITE [10]. The divertor plays an essential role for plasma insulation from material surfaces and for impurity shielding.

The additional heating is necessary for ignition since the Ohmic heating is limited by the plasma resistivity and plasma current. At present, there are two heating methods. One is neutral beam injection (NBI) heating, and the other is radio frequency wave (RF) heating. NBI heating has been successful in many tokamaks. The neutral beam power of 2.4 MW was injected and the ion temperature increased to 6.5 keV in PLT [11]. It should be noted that no adverse effect such as the trapped ion instability [12] was observed in such high temperature

region, and that the transport of the ions is explained by the neo-classical theory [13] within a factor of three. A significant increase of the electron temperature was also observed. The success was ascribable to the progress in the understanding of the impurity control such as Ti-gettering and a carbon limiter, although more improvement must be necessary.

However, NBI heating may be ineffective for a large-scale and high-density plasma since the penetration length of the neutral beam into the plasma becomes shorter with increasing density, while the increase of the beam energy is limited by the decrease in the efficiency of charge-exchange in the neutralizer cell. RF heating is promising even for such a plasma.

RF heating is classified in various types according to the frequency range; electron cyclotron resonance heating (ECRH, $f \lesssim 150$ GHz), lower hybrid resonance heating (LHRH, $f \lesssim 2$ GHz) and ion cyclotron range of frequency heating (ICRF, $f \lesssim 75$ MHz), etc. In the early stage, RF heating was thought to be difficult because of serious impurity production during RF pulse, low heating efficiency and unresolved heating mechanism. At present, it has been found that if the first wall is well conditioned (e.g. Ti-gettering), the RF-power of 200 $\sim$ 300 kW can be successfully coupled to the plasma and significant plasma heating (e.g. 2.3 eV/kW for ICRF Heating, discussed in this thesis) is observed. The understanding of the heating mechanism is also progressing with the progress of the experiment. It is now under investigation to couple the RF power greater than 1 MW to the plasma, together with the development of high power klystrons for LHRH and gyrotrons for ECRH [14] (A 1 MW generator for ICRF has been commercially available).

If the impurity control and the additional heating go well, the equilibrium and stability of the high-β tokamak plasma become the next subject. The high-β tokamak is indispensable from a point of view of economic feasibility of a tokamak fusion reactor. One of the methods to attain the high-β tokamak is to realize a stable low-q (safety factor) discharge. In DIVA, β of 0.8 % at $q = 1.7$ has been successfully attained for a modest toroidal field after controlling radiation loss [15]. The investigation of the high-β tokamak plasma achieved by the high power NBI and/or RF heating will be a main current of the tokamak experiment in the near future.

1.2 Main Subject of the Thesis

A power balance study of a tokamak plasma is necessary to establish a scaling law of plasma parameters which is indispensable for the design of the tokamak fusion reactor. As yet, discussions of the power balance have been restricted only in a core plasma [16]. This paper deals with the power balance including a boundary plasma in Ohmically and radio-frequency wave (RF) heated tokamak plasmas.

In a tokamak, an input power (Ohmic heating power + additional heating power) is balanced with a sum of various power losses. Dominant channels of the power losses are as follows:

(a) Conduction-convection loss

A part of the energies of ions and electrons in the plasma core are carried away by thermal conduction and particle diffusion, and finally lost at the material surfaces such as a wall, a limiter and a neutralizer plate in the divertor. The plasma cross-section of a tokamak is determined by a limiter and/or a magnetic limiter. The plasma outside the limiter edge is called as a scrape-off layer plasma. The heat flux to the material surfaces is determined by the plasma parameters of the scrape-off layer plasma.

(b) Radiation loss

Impurities, especially metal impurities, are not perfectly ionized even in the hot core of the plasma, and the radiation loss due to them is serious as described in 1.1.

(c) Charge-exchange neutral loss

A part of the hot ions in the plasma core undergo the change-exchange with cold neutrals and then immediately escape to the walls. If the plasma density is sufficiently high, the charge-exchange loss is not dominant since a greater part of the hot neutrals are re-ionized until they escape from the plasma column.

DIVA [17] was the first tokamak with an axisymmetric poloidal divertor. The effectiveness of the divertor actions, i.e. (1) plasma insulation from the first wall and (2) shielding impurity influx has been successfully demonstrated [9]. In the work of DIVA, it was emphasized that the scrape-off layer plasma plays an important role in

releasing impurities from the wall and limiter, and that the study of the scrape-off layer plasma is indispensable for the impurity control. In DIVA, the scrape-off layer plasma was well guided into the divertor chamber, and the measurements of the scrape-off layer plasma were widely performed in the divertor chamber without adverse effects to the main plasma column. The measurements comprise the electron and ion temperatures, the electron velocity distribution, the particle flow velocity, the cross-field particle diffusion and the total particle efflux. On the basis of the results of the measurements, the properties of the scrape-off layer plasma are clarified, and the scaling law is derived for the parameters of the scrape-off layer plasma. We can predict the plasma parameters in the scrape-off layer of the future large machine and can consider relevant counterplans for the impurity problems associated with the plasma-wall interaction.

The thermal interaction between the scrape-off layer plasma and the material surfaces was investigated experimentally. This was made possible by the detailed measurements of the heat flux and the ion saturation current to the target as well as of the electron velocity distribution. It has been found that the heat flux is given by the product of the electron temperature, the ion saturation current and the heat transmission rate γ, where γ is derived from the sheath model including a secondary electron emission effect and the two-component Maxwell velocity distribution of the electrons.

The result is applicable to obtain the conduction-convection loss to the wall, the limiter and the divertor since we can measure the total particle flux to each part. Typically, 33 % of the total particle loss and 75 % of the conduction-convection loss are guided into the divertor [9].

The spatial distribution of the radiation loss including the charge-exchange loss was measured by scanning a pyroelectric detector, where the detector was calibrated by heavily contaminated resistive discharges. The charge-exchange loss power was calculated by a Monte-Carlo method for a cylindrical plasma. The calculated charge-exchange loss was a small fraction of the total power loss measured by the pyroelectric detector. Combined with spectroscopic data in the visible to vacuum ultra-violet, we discriminated between the radiation losses due to low-Z (gas) and high-Z (metal) impurities. It was shown that the radiation loss due to low-Z impurities does not play an important role, and that

due to high-Z impurities has a great effect in the radiation loss from the main plasma for the case of the gold wall.

Thus, the power balance has been clarified for the Ohmically heated tokamak plasma. Typical data shows that the percentages of the conduction-convection, radiation and charge-exchange losses to the Ohmic imput power are 60 %, 30 % and 10 %, respectively, for 10 kG, and 70 %, 23 % and 7 %, respectively, for 20 kG with divertor operations.

Next, we proceed to the power balance in RF-heated discharges. RF heating will be more available for a future large-scale and high-density plasma than NBI heating. Particularly, the ion cyclotron range of frequency (ICRF) heating in the two-ion hybrid regime [18] is very promising. The frequency is relatively low (20 $\sim$ 100 MHz), a high power generator ($\sim$1 MW) is presently available, and hence the cost is low.

As is the usual case, we deal with the plasma consisting of the majority deuterium and the minority hydrogen. The frequency was 25 MHz and the toroidal magnetic field was 17 $\sim$ 19 kG. They were chosen so that the frequency agreed with the second harmonic (fundamental) cyclotron frequency of deuterium (hydrogen). The electron density must be high enough for the fast magnetosonic wave to propagate. Typically, we chose the average electron density of $(3\sim4)\times10^{13}$ cm^{-3}. The excited magnetosonic wave propagates deeply into the plasma and is linearly mode-converted into the slow electrostatic mode at the two-ion hybrid resonance layer, which is located a little high field side of the cyclotron resonance layer [19]. The slow mode is strongly damped via the second harmonic cyclotron damping of deuterons, the fundamental cyclotron damping of protons and the electron Landau damping.

Thus, it is generally recognized that the heating mechanism of the ICRF heating in the two-ion hybrid regime is due to the mode conversion. However, the detail has not yet been clarified. Therefore, we first investigate the heating mechanism of the ICRF heating and then proceed to the discussion of the power balance during the heating. The optimum heating conditions were surveyed varying the proton-to-deuteron density ratio and the toroidal magnetic field, which decide the heating efficiency through the Budden tunneling parameter η [19]. It was shown that the results are well explained by the mode conversion [20].

In order to discuss the power balance during the heating, we must know first of all the RF power irradiated to the plasma, P_{Net}. P_{Net} is evaluated from $(R_S-R_C)(P_f-P_b)/R_S$, where R_S and R_C are antenna loading

impedances with an without the plasma, respectively, and P_f and P_b are incident and reflected powers, respectively. Actually, we confirmed that the estimated P_{Net} was roughly in agreement with the increase of the conduction-convection loss to the wall and the divertor.

The heating efficiency is defined as $\Sigma P_{rf}^{\sigma}/P_{Net}$, where P_{rf}^{σ} is the RF power absorbed by σ species in the plasma core (σ = e, D, H). The observed heating efficiency was only 20 $\sim$ 40 % as reported in ATC [21] and our first result [22]. The rest of the power goes to the edge plasma and does not contribute to the heating of the core plasma. In order to prevent the RF power to be lost to the surface plasma, we installed an electrostatic Faraday shield closely over the antenna ceramic cover. As a result, the RF power deposited directly to the surface plasma was reduced significantly and we succeeded in increasing the heating efficiency to more than 80 %. We observed $T_D \sim 430$ eV and $\langle T_H \rangle \sim 740$ eV from the base ion temperature of 160 eV in application of P_{Net} of 115 kW, where T_D and $\langle T_H \rangle$ are the deuteron temperature and the average proton temperature, respectively. It is of paramount importance to know the radial profile of the RF power deposition, its partition to each species and the transport of RF-heated ions from the point of view of the power balance. These are discussed in detail.

In Chapter 2, the DIVA tokamak device and the diagnostics for the main and scrape-off layer plasmas are briefly described. Then the development of the multigrid energy analyzer which is suitable for the measurement of the scrape-off layer plasma is described.

In Chapter 3, experimental results on the scrape-off layer plasma are presented, and the scaling law for the scrape-off layer plasma is derived.

In Chapter 4, the thermal interaction between the scrape-off layer plasma and the material surfaces is investigated experimentally.

In Chapter 5, the gross power balance in the Ohmically heated tokamak plasma is discussed on the basis of the measurements of loss powers including the conduction-convection loss to the wall and the divertor, the radiation loss and the charge-exchange neutral loss.

In Chapter 6, results of the ICRF heating are described emphasizing the optimization of the heating and the power balance.

References

[1] Murakami, M., Eubank, H.P., Physics Today, May (1979) 25.

[2] Furth, H.P., The 3rd International Symposium on Toroidal Plasma Confinement, March 1973 Garching, Paper B9-I.

[3] Berry, L.A., Bush, C.E., Callen, J.D., Colchin, R.J., Dunlap, J.L., in Plasma Physics and Controlled Nuclear Fusion Research (Proc. 6th Int. Conf., Berchtesgaden, 1976) Paper IAEA-CN-35/A4-1.

[4] Jensen, R.V., Post, D.E., Jassby, A.L., Princeton Plasma Physics Laboratory Report PPPL-1350 (1977).

[5] Taylor, R.J., Open, L., UCLA Report, PPG-294 UCLA (1977).

[6] Stott, P.E., Daughney, C.C., Ellis, R.A., Nucl. Fusion 15 (1975) 431.

[7] Ohasa, K., Maeda, H., Yamamoto, S., Nagami, M., Ohtsuka, H., et al., Nucl. Fusion 18 (1978) 872.

[8] Sengoku, S., Matsuda, T., Matsumoto, H., Ohtsuka, H., Arai, T., Characteristics of Carbon-Limiter Surface and Suppression of its Chemical Sputtering, JAERI-M 8465 (1979).

[9] DIVA Group, Nucl. Fusion 18 (1978) 1619; Nagami, M., Divertor Experiment for Impurity Control in DIVA, JAERI-M 8215 (1979).

[10] Fielding, S.J., Hobby, M., McCracken, G.M., Paul, J.W.M., Peacock, N.J., et al., in Controlled Fusion and Plasma Physics (Proc. 8th Europ. Conf. Prague, 1977) Vol.1 (1977) 36.

[11] Eubank, H., Goldston, R., Arunasalam, V., Bitter, M., Bol, K., in Plasma Physics and Controlled Nuclear Fusion Research (Proc. 7th Int. Conf., Innsbruck, 1978) Paper IAEA-CN-37-C-3.

[12] Kadomtsev, B.B., Pogutse, O.P., Nucl. Fusion 11 (1971) 67; Tang, W.N., Nucl. Fusion 18 (1978) 1089.

[13] Hinton, F.L., Hazeltine, R.D., Revs. Mod Phys. 48 (1976) 239.

[14] INTOR Group, Nucl. Fusion 20 (1980) 349.

[15] Maeda, H., Sengoku, S., Kimura, H., Ohtsuka, H., Ohasa, K., et al., in Plasma Physics and Controlled Nuclear Fusion Research (Proc. 7th Int. Conf., Innsbruck, 1978) Vol.1, IAEA, Vienna (1979) 377; DIVA Group, Study on Very-Low-q Discharges in DIVA, JAERI-M 8205 (1979).

[16] e.g. for an ohmic heated plasma, Brusati, M., Davis, S.L., Hosea, J.C., Strachan, J.D., Suckewer, S., Nucl. Fusion 18 (1978) 1205; for a NBI heated plasma, EQIPE TFR, Nucl. Fusion 18 (1978) 1271, and Ref. [11].

[17] Shimomura, Y., Maeda, H., Ohtsuka, H., Kitsunezaki, A., Nagashima, T.,

et al., Phys. Fluids 19 (1976) 1635, see also Ref. [9] and [15].

[18] See Ref. [5] ∿ [8] in Section 6.1.

[19] Swanson, D.G., Phys. Rev. Lett. 36 (1976) 316.

[20] Iizuka, S., Odajima, K., Kimura, H., Sengoku, S., Sugie, T., et al., Propagation and Absorption of the Fast Magnetosonic Wave Near a Two-Ion Hybrid Resonance Layer, JAERI-M 8595 (1979) [to be published in Phys. Rev. Lett.].

[21] See Ref. [8] in Section 6.1.

[22] Kimura, H., Odajima, K., Sengoku, S., Ohasa, K., Sugie, T., Nucl. Fusion 19 (1979) 1499 [Section 6.1 in this thesis].

2. DIVA TOKAMAK DEVICE AND DIAGNOSTICS

2.1 DIVA Tokamak Device [1]

Figure 1 (a) and (b) show cross-sectional views of the device. Basic machine parameters are as follows.

Major radius	R = 60 cm
Minor radius	a = 10 cm
Toroidal magnetic field	B_T = 8 - 20 kG
Plasma current	I_P = 10 - 80 kA

DIVA is a tokamak with a divertor hoop coil with a current capability of 60 kAT. The divertor hoop current is proportional to the plasma current and provides the axisymmetric magnetic limiter with a single null magnetic separatrix. The equilibrium of a plasma column with the magnetic limiter inside the shell has been established in the range of $0.7 \leq I_D/I_P \leq 1.8$, where I_D and I_P are respectively the divertor hoop current and the plasma current. Plasmas are produced inside the magnetic separatrix surface, and outgoing plasmas due to the diffusion process are partially guided into the burial chamber.

A brief description is given for each section.

(1) Shell; The plasma is enclosed in a copper shell which is divided into four sector pieces in the toroidal direction. Its surface was ion-plated with gold in 20 μm in thickness to reduce adsorption of gases. Later, the inner surface of the shell has been coated by titanium for the experiments of very-low-q discharge [2] and ICRF heating (see Chapter 6).

(2) Divertor hoop; A four-turn coil is encased in a vacuum-tight stainless-steel tube.

(3) Divertor plate; The outgoing plasma diffusing from the main plasma column is intersected by the divertor plate made of titanium.

(4) Protection plate; Three gold pieces as shown in Fig. 1 are manually movable as the protection plates of the shell surfaces.

(5) Gas feeder; The working gas is introduced into the vacuum chamber through 2 ∿ 4 fast-acting gas valves. Additional gas injection can be made with a programmable gas feeder (Veeco).

(6) Vacuum system; The vacuum chamber is made of stainless-steel with an insulating break, pumped by a turbo-molecular pump with an effective speed of 400 l/sec to a base pressure of $1.5 \sim 0.5 \times 10^{-7}$ Torr and bakeable at a temperature of 110 °C.

2.2 Diagnostics

Figure 2 is a top view of the device, showing the arrangement of the diagnostic instruments. They are listed as follows.

Main plasma

Electron temperature	(1) laser scattering (2) soft X-ray energy analyzer
Electron density	2 mm, 4 mm microwave interferometers
Ion temperature	(1) 10-ch charge-exchange neutral energy analyser (2) 1 m Czerny-Terner mounting vacuum monochromator
Spectroscopy	(1) 3 m grazing-incidence monochromator (10-1300 Å) (2) 25 cm, 1 m visible monochromators (3) 1 m Czerny-Terner mounting vacuum monochromator
Radiation loss	Pyroelectric detector
Fluctuation	(1) magnetic probe (2) PIN-diode

Scrape-off layer plasma

Electron temperature	Langmuir probe
Electron energy spectrum	Electrostatic energy analyser
electron density	(1) Langmuir probe (2) 4 mm microwave interferometer
Ion temperature	(1) Electrostatic energy analyser (2) Ion-sensitive probe

	(3) 1 m Czerny-Terner mounting vacuum monochromator
Flow velocity	Uni-directional probe
Heat flux	(1) thermo-couple
	(2) Ni-thin-film thermometer
Particle flux	Shell, divertor plate and limiter
Runaway electron	X-ray target
Poloidal magnetic field	(1) Hall element
	(2) magnetic probe

Typical plasma parameters in the main and scrape-off layer plasmas are as follows.

Main plasma

Central electron density	$n_{eo} = (2\text{-}14)\times10^{13}$ cm^{-3}
Central electron temperature	$T_{eo} = 200\text{-}700$ eV
Central ion temperature	$T_{io} = 70\text{-}300$ eV
Energy confinement time	$\tau_E = 0.8\text{-}5.7$ ms
Particle confinement time	$\tau_p = 0.5\text{-}4.0$ ms
Safety factor	$q_a = 1.3\text{-}6.0$
Ohmic heating power	$P_{in} = 40\text{-}200$ kW

Scrape-off layer plasma

Electron temperature	$T_{es} = 20\text{-}100$ eV
Ion temperature	$T_{is} = 20\text{-}70$ eV
Electron density	$n_{es} = (1\text{-}10)\times10^{12}$ cm^{-3}
Heat flux	$q = 0.2\text{-}2$ kW/cm^2

The electrostatic energy analyser plays an important role in the measurement of the scrape-off layer plasma. It gives informations of the ion temperature and the electron temperature including the velocity distribution. The next section describes the development of the analyser which can be used for the plasma with relatively high plasma parameters.

2.3 Development of Multigrid Energy Analyzer

A multigrid energy analyzer was used to measure the ion temperature in the scrape-off layer of DIVA, where the plasma parameters were relatively high, i.e. electron and ion temperatures T_e and $T_i \lesssim 60$ eV; electron density $n_e \lesssim 5 \times 10^{12}$ cm^{-3}; heat flux $q \lesssim 2$ kW/cm^2. It was found that to obtain the true ion temperature, the bias voltage V_E of the entrance apertures of the analyzer must be chosen so as to satisfy the criterion $e|V_S - V_P| \ll T_i$, where V_S and V_P are the plasma potentials before and after the entrance apertures, respectively.

The data were consistent with those obtained by other methods, i.e. the Doppler broadening of impurity lines and the Katsumata probe (ion-sensitive probe).

2.3.1 Introduction

A multigrid analyzer has usually been used for a plasma with a relatively low density and temperature [3,4]. In the scrape-off layer of DIVA, however, the plasma parameters are relatively high, i.e., T_e and $T_i \lesssim 60$ eV; and $n_e \lesssim 5 \times 10^{12}$ cm^{-3}, where T_e, T_i, and n_e are the electron and ion temperatures, and electron density, respectively. Measurement with a multigrid analyzer is rather difficult in such a plasma. First, there is relatively large heat flux in the scrape-off layer (typically 2 kW/cm^2). The external jacket of our analyzer is made of molybdenum and a mesh cannot be used as the entrance aperture of the analyzer. Instead, a molybdenum plate with small entrance apertures (0.1 mm in diameter) is used, which we shall call the front end of the analyzer.

However, the electron density in the scrape-off layer is relatively high. The Debye length λ_D calculated with typical data of the scrape-off layer plasma, i.e. $T_e \sim 50$ eV and $n_e \sim 5 \times 10^{12}$ cm^{-3}, is about 0.03 mm. It is difficult to make such a small hole in the metal plate. The minimum diameter of the aperture is 0.1 mm for a metal plate 0.1 mm thick. The entrance aperture is therefore not completely screened by a Debye layer, and particles flow into the analyzer in the plasma state. In addition, as the pitch angle of the entrance aperture is not small, ions with Larmor radii somewhat larger than the diameter of the entrance aperture can flow into the analyzer. Thus, the two-dimensional flow of ions in the analyzer must be taken into account. It is thought that the plasma potentials and ion temperatures are different before and after the entrance aperture.

This problem inevitably arises when the analyzer is applied to a scrape-off layer in a tokamak, where the plasma parameters are relatively high. However, the difficulty was solved experimentally by supplying an appropriate bias voltage to the front end of the analyzer.

In 2.3.2, the structure of the multigrid analyzer is described. In 2.3.3, we examine the characteristics of the analyzer, applying it to the moderate discharges of DIVA. An entrance aperture with a diameter several times larger than λ_D is used. According the difficulty mentioned above becomes more serious, though heat damage is completely suppressed. The relationship between (virtual) ion temperatures and the front end bias V_E is shown. Then the condition for obtaining the true ion temperature is discussed. In 2.3.4, the analyzer is applied to the full operations of DIVA. The result is checked using the criterion discussed in 2.3.3. In 2.3.5, the data from the multigrid analyzer is compared with that obtained by other methods, i.e. the Doppler broadening of impurity lines and the Katsumata probe (ion sensitive probe).

2.3.2 Structure of Multigrid Analyzer

Figure 3 shows the multigrid analyzer schematically. The design was somewhat modified from the previous design [5, 6]. The external jacket of the analyzer is made of molybdenum.

In front of the stainless-steel collector plate C, 5 mm in diameter, a molybdenum front end E and two stainless-steel grids (G_1, G_2) are placed 1 mm apart. The mesh grids G_1 and G_2 are of 50 μm wire and have a transparency of 0.44. The bias voltage of the front end can be varied with respect to the external jacket, which is at the same potential as the vacuum vessel. The front views of the entrance apertures are shown in Fig. 3. Type (a) is a slit 3 × 0.2 mm wide and 0.1 mm thick, used for moderate discharges. Type (b) consists of seven holes in line, each of which is 0.1 mm in diameter and 0.1 mm thick, used for full discharges.

2.3.3 Condition for Obtaining True Ion Temperature

The characteristics of the analyzer were investigated in detail for moderate discharges using the type (a) entrance aperture. The plasma parameters at the position of the analyzer were as follows: $n_e \sim 8 \times 10^{11}$ cm ^{3}, $T_e \sim 8$ eV from a Langmuir probe, and heat flux $q < 50$ w/cm^2 from an

Ni thin-film thermometer [5]. λ_D is calculated to be about 0.03 mm, while the width of the entrance channel is 0.2 mm. In this situation the second problem described in 2.3.1 was somewhat aggravated.

2.3.3.1 Experimental procedures

Figure 4 shows the cross-sectional view of DIVA. The analyzer was placed at R = 40 cm, Z = 4 cm, and the front end was almost perpendicular to the toroidal magnetic field to receive the plasma flow from the main plasma column along the field line. The toroidal field was fixed at 10 kG (R = 60 cm). The ratio of the divertor hoop current to the plasma current to the plasma current was 1.2, the latter being 14 kA with a flat top.

Figure 5 shows the potential distribution between the front end E, grids G_1 and G_2 and the collector to obtain the ion velocity distribution. The ion energy spectrum is obtained in a shot by supplying a fast sawtooth pulse with an amplitude of 200 V to the collector. The pulse width is 1 ms, which is short compared with the time for a significant change in the ion saturation current.

2.3.3.2 Results of measurements

Figure 5 shows oscillograms of the ion energy spectra. These were obtained 15 ms after starting the discharge for various bias voltages of the front end E with respect to the vacuum vessel. The bias voltages of grids G_1 and G_2 were -150 V and -200 V with respect to E, respectively. Each oscillogram was double-swept to show reproducibility between two successive discharges.

From these oscillograms it is found that the saturation level of the collector current, I_c, the potential difference V_P-V_E, where V_P is the potential from which ions are retarded, and the (virtual) ion temperature T_i depend on the front end potential V_E. These are plotted as a function of V_E in Figs. 6, 7 and 8, respectively. A floating potential V_f and the space potential V_S measured with a Langmuir probe are shown on each abscissa.

2.3.3.3 Discussions

The saturation level of collector current is a maximum at $V_E \approx V_S$ (Fig. 6). This indicates that if the front end is at the same potential as the plasma, a sheath is not formed in the entrance aperture and the

plasma particles flow freely into the analyzer. On the other hand, if the front end potential is respectively lower or higher than the plasma potential, an ion or electron sheath is formed in the entrance aperture and some portion of the plasma particles are respectively absorbed or repelled by the sheath.

The potential difference V_P-V_E is negative and its absolute value has a maximum in the neighbourhood of $V_E \simeq V_S$ (Fig. 7). It may be qualitatively understood as follows. The plasma which has passed through the entrance aperture is separated into ions and electrons by the electric field between the front end E and the grid G_1, where G_1 is at -150 V with respect to E. G_1 is screened by the ion sheath. The sheath thickness d is roughly calculated using the Child-Langmuir $\frac{3}{2}$ - power law as

$$d = \sqrt{5.4\times10^{-8} \frac{V^{3/2}}{j}} \quad (m),$$

for hydrogen plasma, where j is the ion saturation current density (A/m^2) and V the potential difference between plasma and electrode. j was measured by the Langmuir probe as 1.7×10^3 A/m^2. For V = 150 Volt, d = 0.24 mm, while the spacing between E and G_1 was 1 mm. The plasma entering the analyzer is separated into ions and electrons at about 0.7 mm from the entrance aperture.

However, the ion and electron Larmor radii are 0.3 mm and 0.005 mm, respectively, for T_i = 20 eV, T_e = 10 eV, and B_s = 15 kG (toroidal field at the position of the analyzer). The width of the entrance aperture is 0.2 mm, which is somewhat smaller than the ion Larmor radius. Unless the distance from the entrance aperture to the sheath edge is short enough compared with the ion Larmor radius, separation of the ion and electron components of the plasma can occur before they reach the sheath edge. The core of the plasma beam cut down by the entrance channel is electron-rich, while the outer region of the beam is ion-rich. Ions with large Larmor radii are likely to be lost to the mesh wire. Therefore ions which succeed in passing through the grids G_1 and G_2 and reach the collector C are mainly from the central electron-rich plasma. A schematic drawing of the phenomena near the entrance aperture is shown in Fig. 9.

For $V_E < V_S$, some of the electrons are repelled at the entrance channel. The plasma which has passed through the entrance aperture is less electron-rich. The difference $V_P - V_E$ decreases monotonically with

incresing V_E for $V_E < V_S$, and its absolute value has a maximum at $V_E = V_S$. When $V_E > V_S$, ions are repelled at the entrance aperture. Those which succeed in passing through the entrance aperture must have relatively small Larmor radii. The separation of ion and electron components is rather difficult. That is, $V_P - V_E$ again increases for $V_E > V_S$.

Ion temperatures are determined from the linear part of the semi-log plot of ion energy spectra in Fig. 5. They are plotted on Fig. 8 as a function of V_E. It should be noted that ion temperature decreases monotonically with increasing V_E for $V_E < V_S$, is kept constant for $V_S < V_E < 60$ V, and again increases for $V_E > 80$ V. Similar results are obtained for ion temperatures determined from the least square method using pitch angles of the entrance aperture in the range $30° \sim 60°$ [6].

The dependence of ion temperature on V_E can be understood as follows. Figure 10 shows the potential difference $V_S - V_P$ as a function of V_E. Figure 11 shows ion temperatures versus $|V_S - V_P|$. It is shown that the ion velocity distribution is distorted by the potential difference $|V_S - V_P|$. Although the detailed mechanism of the enhancement of ion temperature for large values of $|V_S - V_P|$ has not been made clear up to now, one possible explanation is as follows. Ions flowing into the entrance aperture are accelerated or retarded according to the sign of $V_S - V_P$. The acceleration or retardation is not necessarily uniform. Some ions of $V_\perp/V_\parallel \gtrsim 1$ from the edge of the plasma beam, which is cut out by the entrance aperture, are less accelerated or retarded than those from the center of the beam. This process gives rise to the distortion of the ion velocity distribution. On the other hand, if V_P is in accord with V_S, the ion velocity distribution cannot be distorted in principle. $Ti(V_E)$ must be a minimum under this condition. The condition $V_P = V_S$ is realized at $V_E \sim 50$ V (Fig. 10). $V_P = V_S$ is not obtained simply by setting the front end bias voltage to equal the space potential of the plasma before the entrance aperture. Figure 11 indicates that the condition for obtaining the true ion temperature is not rigorously $V_S = V_P$, but sufficient to be written as $e|V_S - V_P| \ll T_i$.

In contrast to the ion temperature, the electron temperature can be measured easily, since the electron Larmor radius is so small in comparison with the diameter of the entrance aperture that no distortion of the velocity distribution occurs. $T_e = 8$ eV from the analyzer with $V_E = 0$ V, which agrees with that from a Langmuir probe.

2.3.4 Application to Full Operations

The multigrid analyzer was applied to the full operation of DIVA. The discharge conditions were as follows. The toroidal magnetic field was 20 kG. The ratio of the divertor hoop current to the plasma current was 1.2, the latter being 40 kA with a flat top. The central electron and ion temperatures were 700 and 270 eV respectively from laser scattering, soft X-ray and charge-exchange neutrals, impurity Doppler broadening. The peak electron density was 8×10^{13} cm^{-3} measured with a 2 mm μ-wave interferometer.

The entrance channel of the analyzer was type (b) (see Fig. 3). The analyzer was placed at R = 40 cm, Z = -4.25 cm. The plasma parameters at this point were T_e = 26 eV and $n_e \sim 3 \times 10^{12}$ cm^{-3} from the multigrid analyzer and heat flux q = 1.2 kW/cm^2 from a thermocouple at 9 ms. Figure 12 shows oscillograms of the ion energy spectra 9 ms after starting discharge. Each oscillogram was double-swept to show shot-to-shot reproducibility. The upper trace was obtained by setting V_E to be a floating potential, about 30 V with respect to the vacuum vessel. The lower trace is for V_E = 140 V.

It is clear that the former has a longer tail than the latter. The ion temperatures determined from a semi-log plot of the energy spectra are 88 eV and 56 eV, respectively (see Fig. 13). Let us examine whether T_i = 56 eV is correct, using the criterion discussed in 2.3.3. The electron temperature and floating potential were 26 eV and 30 V, respectively. The space potential V_S was not measured in this case. However it can be estimated using the relationship between the space potential and the floating potential including the effects of the strong magnetic field and secondary electron emission [5]. The result is about 90 V. The plasma potential V_P determined from the ion energy spectrum is about 80 V for V_E = +140 V, so $|V_S - V_P| \sim 10$ V, which satisfies the condition for obtaining the true ion temperature, $e|V_S - V_P| \ll T_i$.

2.3.5 Comparison with Other Methods

The ion temperature measured with the multigrid analyzer was cross-checked by the Doppler broadening of impurity lines. Detailed descriptions of this method are given elsewhere [7]. The vacuum monochromator was connected to the R-Z scanning port. The mirror was scanned horizontally so that the plasma light from the divertor region was received by the

monochromator (see Fig. 4). The spatial resolution for this measurement was about 2 cm.

The observed broadening of the 5th order line of C V (2271 Å) and the 7th order line of C IV (1548 Å) provided temperatures of 85 eV and 42 eV at 9 ms respectively. The spectroscopic measurements [10] show that the main portion of the C^{4+} ions in the divertor region consists of those which diffuse out from the main plasma column, while the C^{3+} ions come directly from the outer region surrounding the main plasma column. The proton temperature obtained with the multigrid analyzer lies between the CV and CIV temperatures. All of these data obtained are consistent with each other.

The other cross-check was done with a Katsumata probe [8], from which the perpendicular ion temperature can be measured. It became evident that the ion temperature in the scrape-off layer is isotropic. The detailed results are reported in ref. 9.

2.3.6 Conclusion

The multigrid analyzer was successfully applied to the scrape-off layer plasma in DIVA, where the plasma parameters are relatively high, i.e. T_e, $T_i \lesssim 60$ eV, $n_e \lesssim 5 \times 10^{12}$ cm^{-3} and heat flux $q \lesssim 2$ kW/cm^2. The potential difference between the plasma before and after entering the entrance aperture affects the ion velocity distributions seriously. It was found that the front end bias must be chosen so as to satisfy the condition $e|V_S - V_P| \ll T_i$ in order to obtain the true ion temperature.

The data are consistent with other methods, i.e. the Doppler broadening of impurity lines and the Katsumata probe.

References

[1] Shimomura, Y., Maeda, H., Kitsunezaki, A., Nagashima, T., Ohtsuka, H., et al., An Outline of the JFT-2a device, JAERI-M 6135 (1975) [in Japanese].

[2] DIVA Group, Study on Very-Low-q Discharges in DIVA, JAERI-M 8205 (1979); DIVA Group, Nucl, Fusion 20 (1980) 271.

[3] Lobikov, E.A. and Nastyukha, A.I.; Sov. Phys. - Tech. Phys. 7 (1963) 903.

[4] Andersen, S.A., Jensen, V.O., Michelsen P. and Nielsen, P.; Phys. Fluids 14 (1971) 728.

[5] Kimura, H., Maeda, H., Ueda, N., Seki, M., Kawamura, H., Yamamoto, S., Nagami, M., Odajima, K., Sengoku, S. and Shimomura, Y.; Nucl. Fusion 18 (1978) 1195.

[6] Kimura, H., Ohtsuka, H., Maeda, H., Shimomura, Y., Yamamoto, S., Nagami, M., Odajima, K., Ueda, N. and Senogoku, S.; Report of Japan Atomic Energy Research Institute, JAERI-M 6861 (1977) [in Japanese]

[7] Sugie, T., Takeuchi, H., Kasai, S., Funahashi, A., Takahashi, K. and Kimura, H.; J. Phys. Soc. Jpn. 44 (1978) 1960.

[8] Katsumata, I. and Okazaki, M.; Jpn. J. Appl. Phys. 6 (1967) 123.

[9] Odajima, K., Kimura, H., Maeda, H. and Ohasa, K.; Jpn. J. Appl. Phys. 17 (1978) 1281.

[10] Nagami, M., Shimomura, Y., Maeda, H., Kasai, S., Yamauchi, T., Sengoku, S., Sugie, T., Yamamoto, S., Odajima, K., Kimura, H. and Ohasa, K.; Nucl. Fusion 18 (1978) 1347.

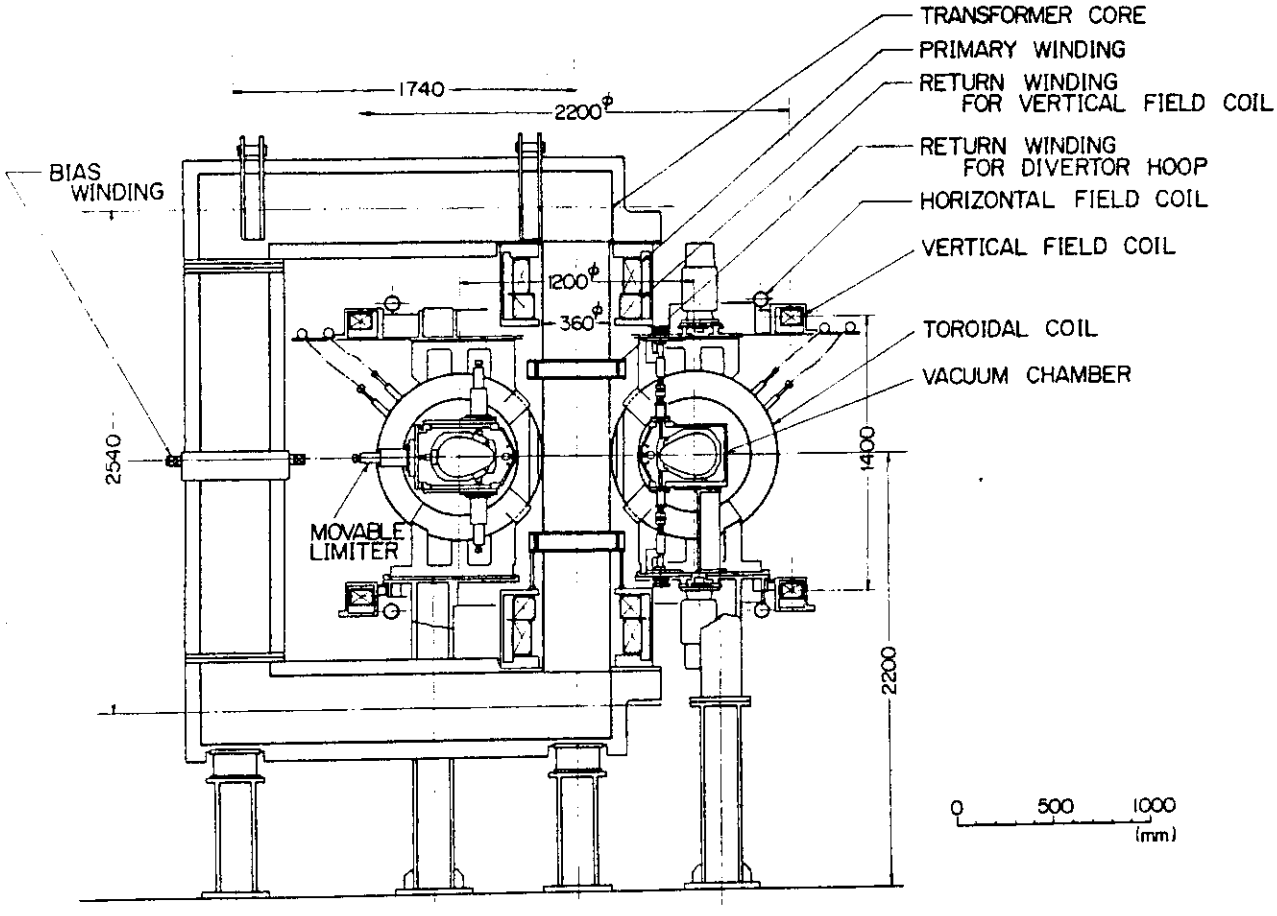

(a)

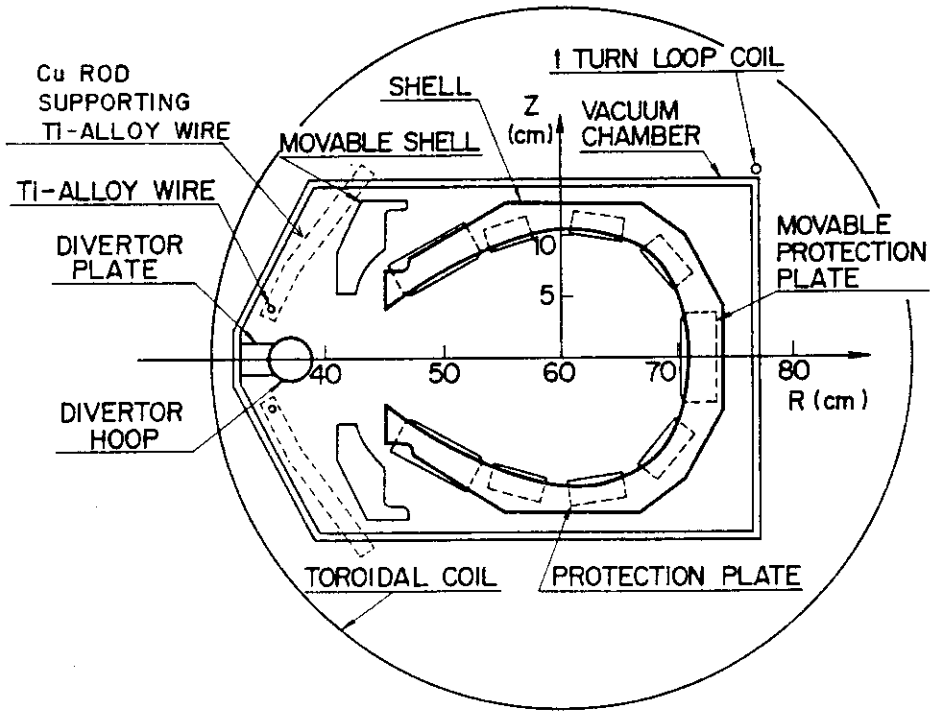

(b)

Fig. 1(a),(b) Cross-sectional view of DIVA.

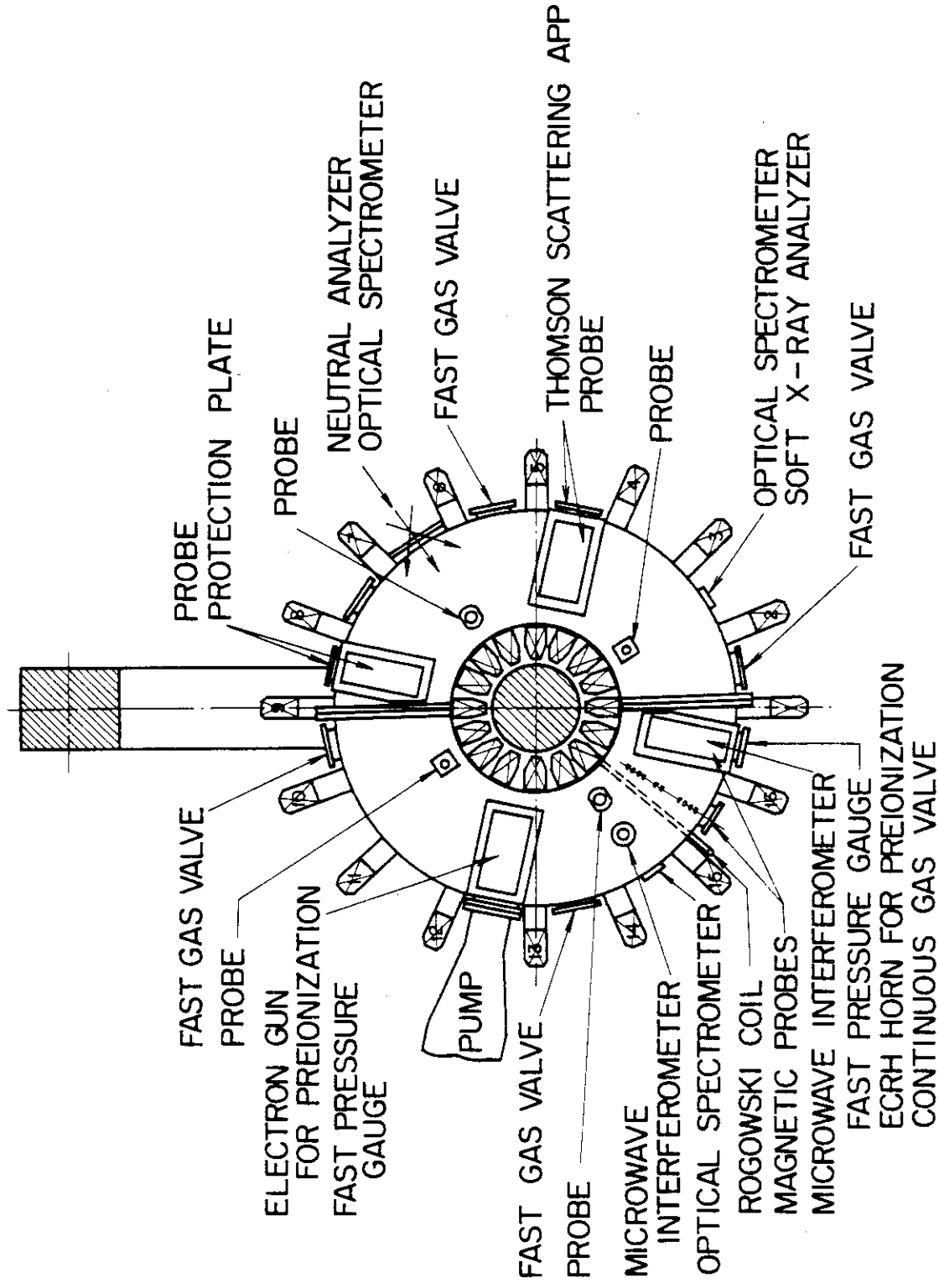

Fig. 2 Top view of the device and arrangement of the diagnostic instruments.

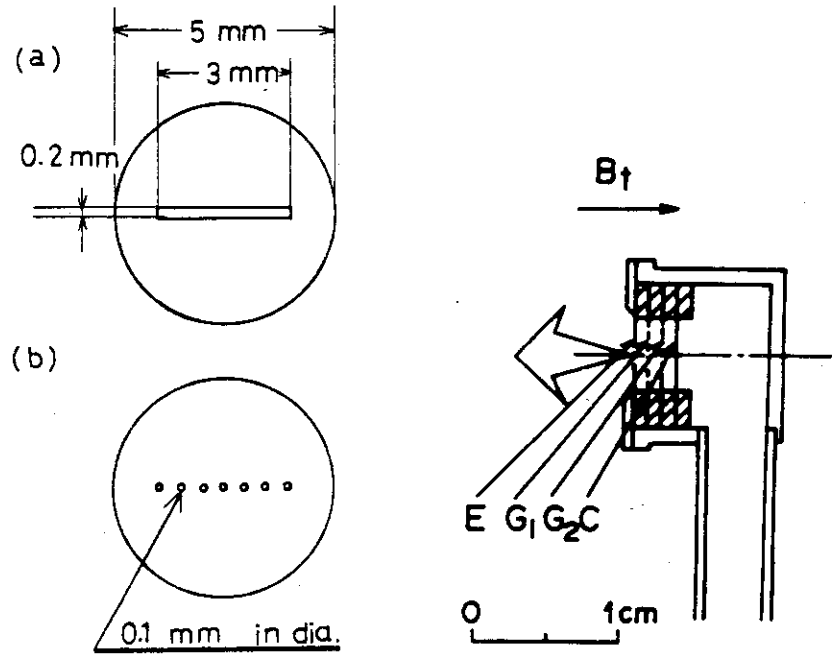

Fig. 3 Schematic drawing of the multigrid energy analyzer. The front views of the entrance apertures are extended. Apertures of types (a) and (b) are used for moderate and full discharges, respectively.

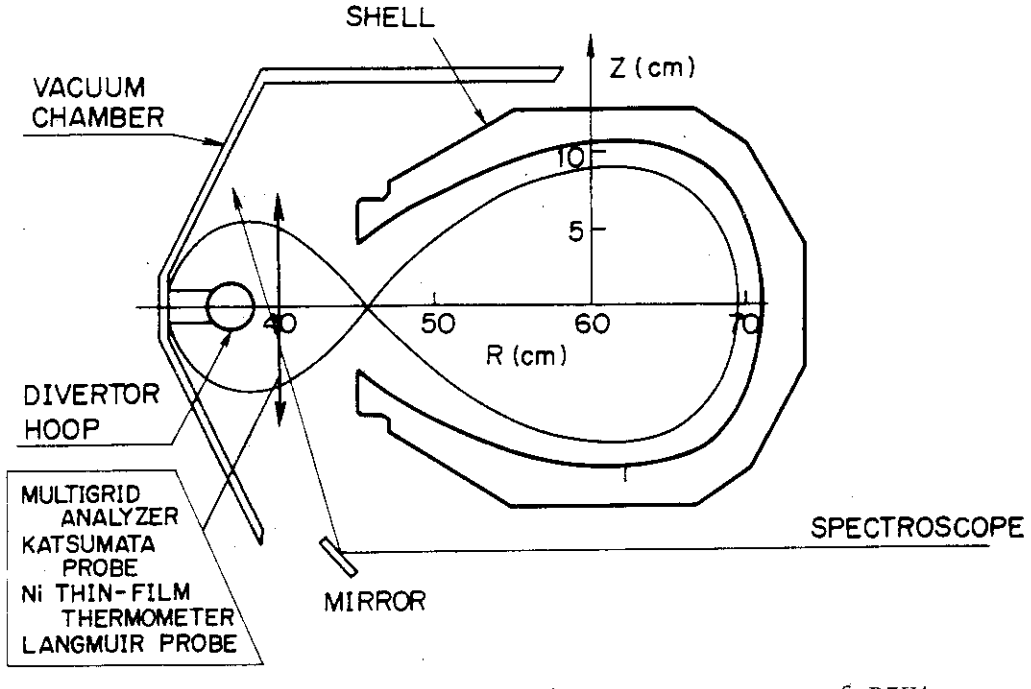

Fig. 4 Schematic drawing of the cross-section of DIVA. The multigrid analyzer, Katsumata probe, Ni thin-film thermometer, and Langmuir probe, are scanned vertically at R = 40 cm. The optical arrangement for the spectroscope is also shown.

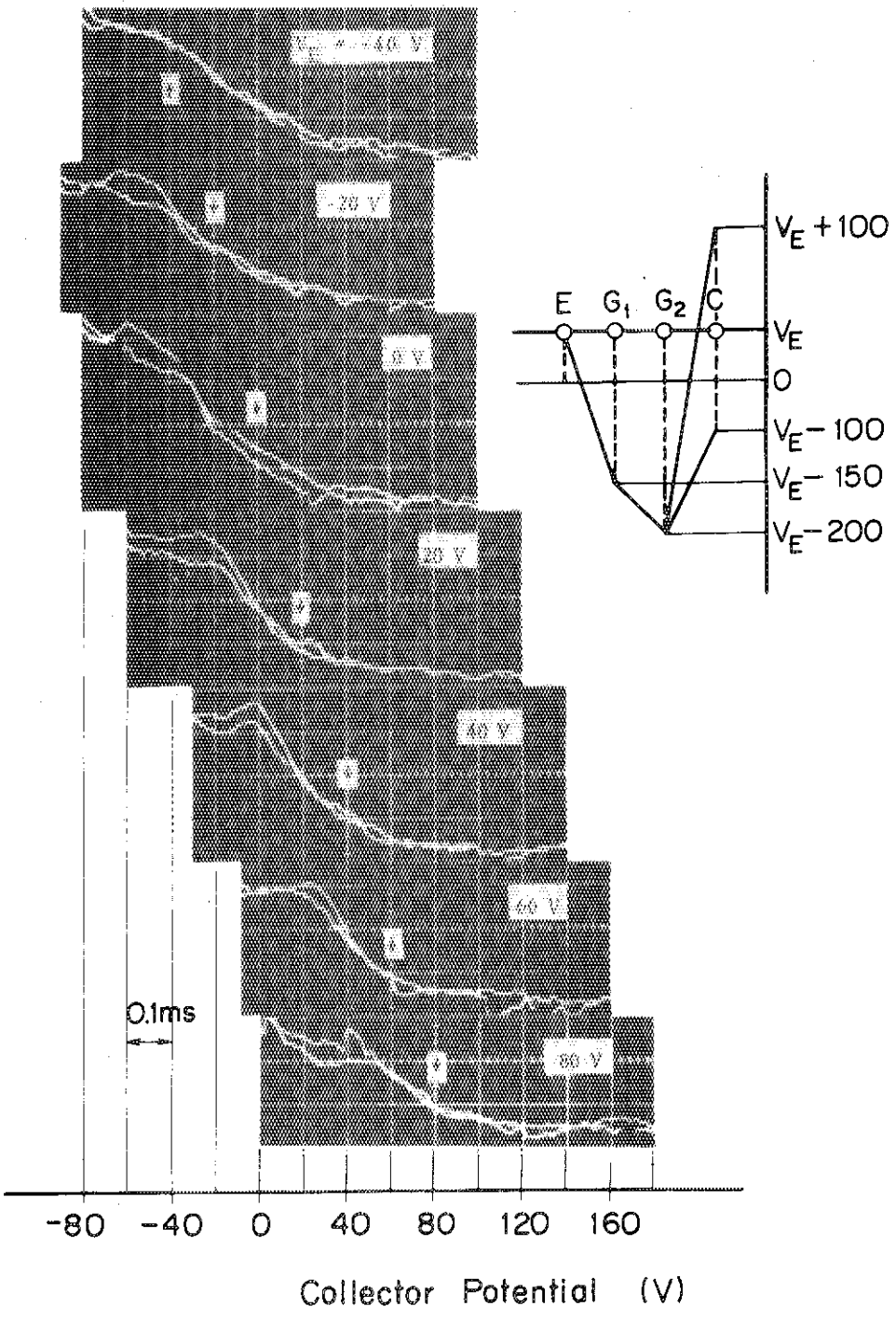

Fig. 5 Oscillograms of ion energy spectra for various bias voltages of the front end E, at R = 40 cm, Z = 4 cm, and t = 15 ms for discharges of B_T = 10 kG and I_p = 14 kA. The arrow shows the position of the front end bias V_E on the abscissa. The potential distribution without plasma between E, G_1, G_2, and C is also shown.

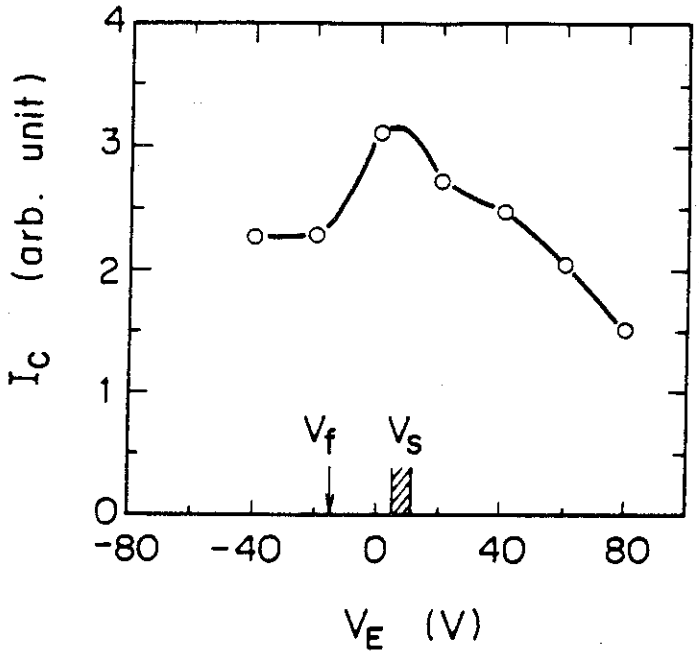

Fig. 6 Saturation current I_C as a function of the front end bias V_E. I_C is determined as the amplitude of the constant part of the energy spectrum in Fig. 5. V_f and V_S are respectively the floating potential and plasma potential before the entrance aperture.

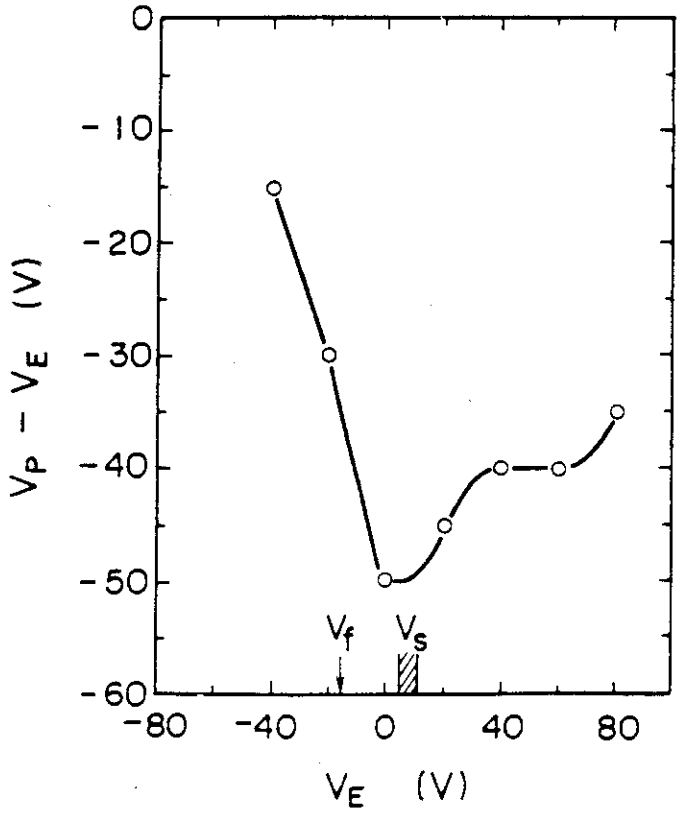

Fig. 7 Potential difference V_P-V_E as a function of the front end bias V_E, where V_P is determined from the ion energy spectrum in Fig. 5 as the potential from which ions are retarded.

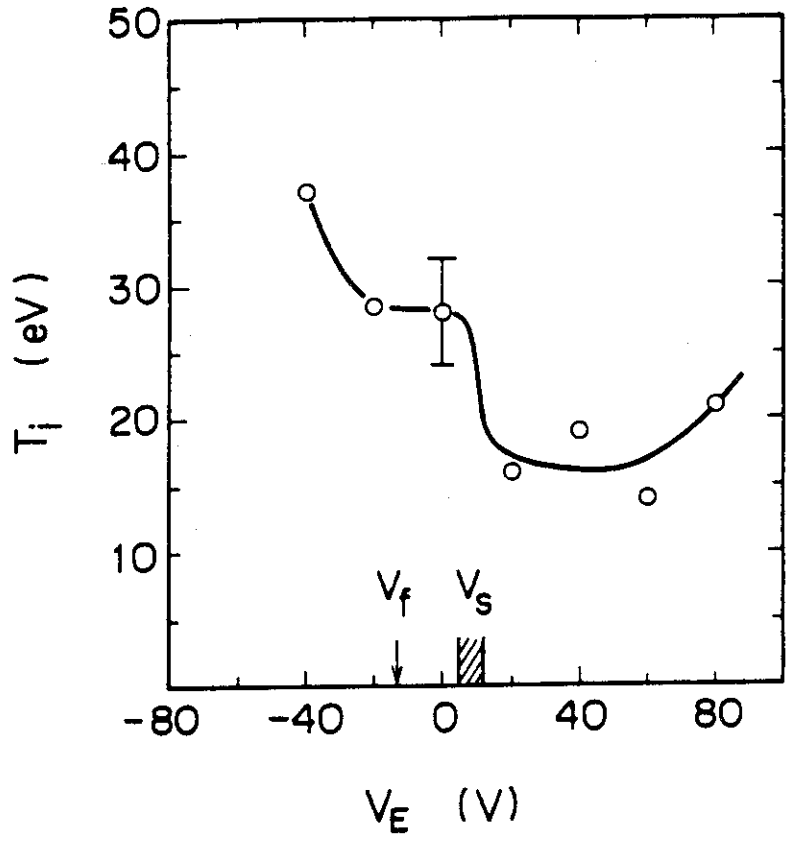

Fig. 8 Ion temperature T_i as a function of the front end bias V_E. T_i is determined from the linear part of the semi-log plots of the energy spectrum in Fig.5.

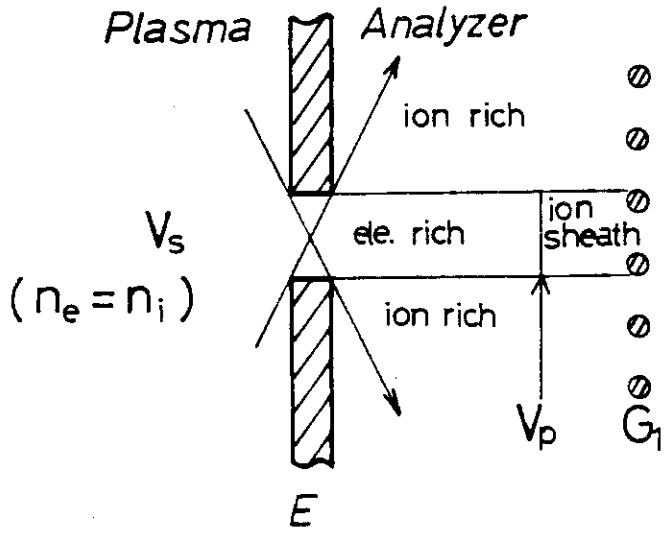

Fig. 9 Schematic drawing of the phenomena near the entrance aperture.

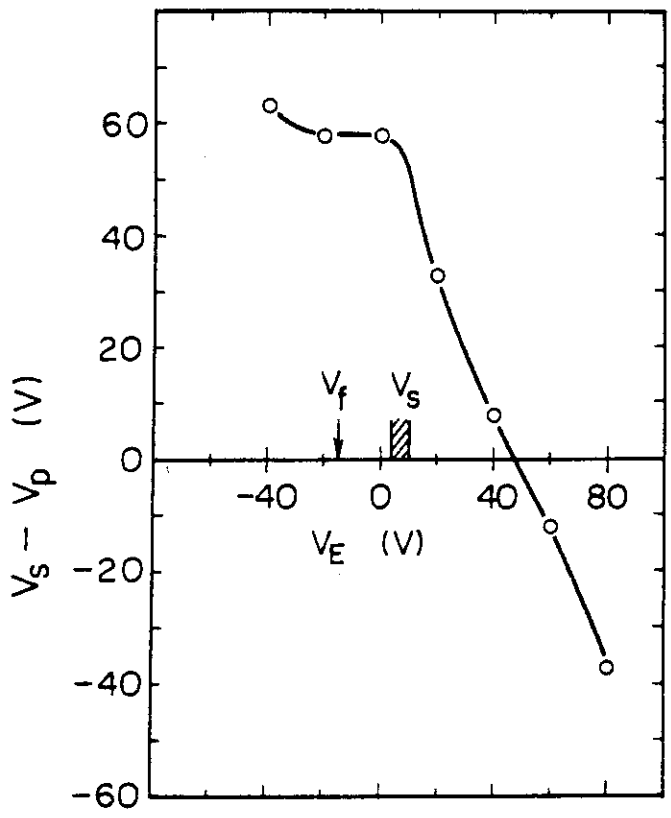

Fig.10 Potential difference V_S-V_P as a function of the front end bias V_E. V_S and V_P are the plasma potentials before and after the entrance aperture, respectively.

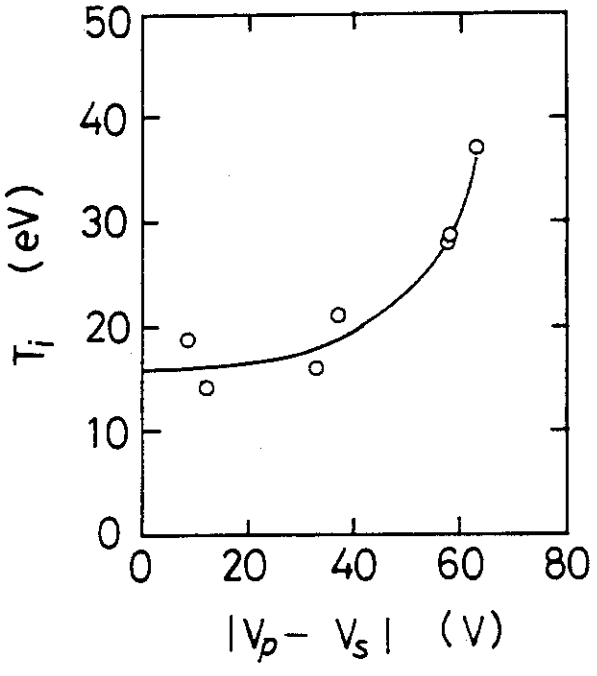

Fig.11 Ion temperature T_i versus $|V_S$-$V_P|$.

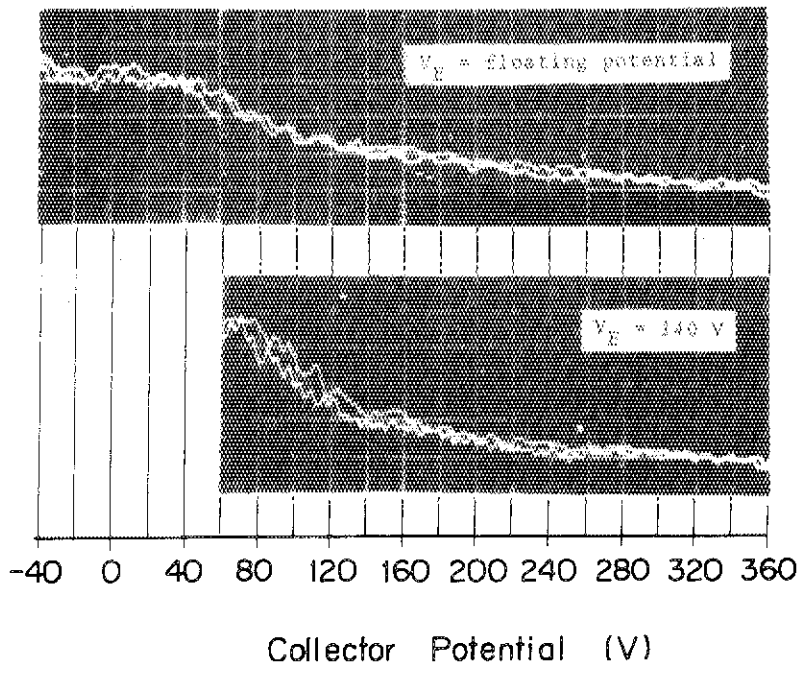

Fig.12 Oscillograms of ion energy spectra at R = 40 cm, Z = -4.25 cm, and t = 9 ms for discharges of B_T = 20 kG and I_P = 40 kA. The upper trace is for V_E as a floating potential, while the lower trace is for V_E = 140 V.

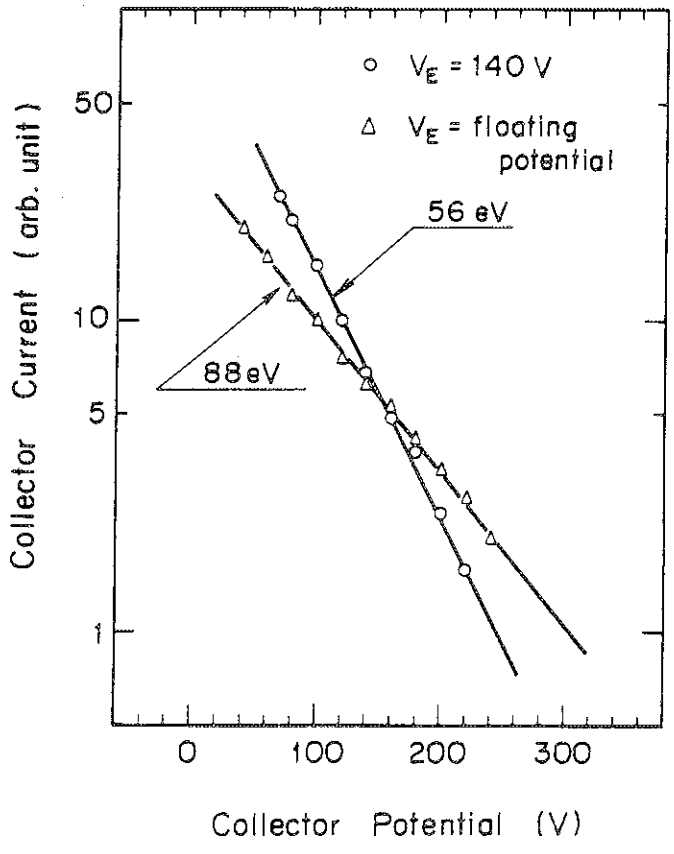

Fig.13 Semi-log plots of Fig.12.

3. SCRAPE-OFF LAYER PLASMA

3.1 Introduction

It is generally believed that plasma-wall interactions become more serious in a future large tokamak because the plasma temperature of the scrape-off layer increases with the increasing temperature of the main plasma. From this point of view, the scrape-off layer plasma has been investigated, employing the various probes listed in the previous chapter. The insertion of probes in tokamak plasmas is very limited. For example, in DIVA, plasma disruptions occur if probes penetrate the main column, whereas they can be used successfully in the divertor region. The divertor region is away from the main plasma and impurity backflow is negligibly small [1]. Therefore, we can obtain detailed information about the scrape-off layer plasma by the probe measurement of the divertor plasma which diffuses out from the main plasma column. The results can be applied to a conventional tokamak, where the plasma-wall interaction takes place at a material limiter.

The boundary condition of the scrape-off layer plasma is ruled by the sheath [2]; the sheath is formed at the wall, the limiter and the neutralizer plate in the divertor chamber. The particle flow velocity (typically 0.3 C_s, C_s is a sound velocity) and the heat transmission rate γ (typically $\sim$7) are determined by the sheath. The flow velocity affects the particle divertor efficiency and the efficiency of shielding impurity influx. The heat transmission rate determines the ratio of the boundary to core plasma temperatures.

Thus, the sheath plays an important role in determining the characteristics of the scrape-off layer plasma. The cross-field diffusion in the scrape-off layer is also of importance since it decides the average particle confinement time and the divertor efficiency. In DIVA, the total particle efflux can be measured and a Bohm-like functional dependence of the diffusion coefficient was ascertained. In the scrape-off layer, a two-dimensional ambipolar diffusion must be taken into account. A decreasing potential along the field line to the divertor plate was observed. Detailed discussions about this effect are beyond the scope of the thesis.

In Section 3.2, the characteristics of the scrape-off layer plasma are surveyed, such as the electron and ion temperatures, the particle

flow velocity, the cross-field diffusion and the particle loss flux to the wall. In Section 3.3, the results are generalized and an empirical scaling for the scrape-off layer plasma is derived. A summary is given in Section 3.4.

3.2 Observation of the Scrape-off Layer Plasma

3.2.1 Electron and Ion Temperatures

The electron temperature was measured by the Langmuir probe and the multigrid analyser. Especially, the latter was used to obtain the electron energy spectrum. The ion temperature was measured by the multigrid analyser (for the parallel temperature) and by the ion-sensitive probe (Katsumata probe [3], for the perpendicular temperature). We also employ the impurity Doppler broadening for the ion temperature (see Section 2.3).

Figure 1 shows an example of Z-profiles of the electron and ion temperatures, which were obtained by scanning the multigrid analyzer. The spatial resolution of the analyser was 1 mm. The abrupt changes of the profile at Z = ±4 cm correspond to the separatrix magnetic surface [4]. The electron and ion temperatures are roughly in agreement; this is one of the features of the scrape-off layer plasma.

The measurement by the Katsumata probe is reported in Ref. [3]. Figure 2 shows Z-profiles of perpendicular and parallel ion temperatures. These two ion temperatures agree well, indicating the isotropic velocity distribution of the ions.

The electron velocity distribution is important for the estimate of the heat flux to the material surfaces, as is shown in Chapter 4. Figures 3(a) and (b) show the energy spectra of electrons on the electron and the ion sides of the divertor (see Section 4.1), respectively. A remarkable high-energy tail appears on the electron side. It also exists on the ion side, but their amount and energy are small. We shall call those electrons epithermal. In Ref. [5], the loss mechanism of the epithermal electrons is discussed in detail. The epithermal electrons must be generated continuously by the acceleration of the toroidal electric field in the vicinity of the main plasma. Once the epithermal electrons flow into the scrape-off layer from the main plasma, they go to the divertor plate through the scrape-off layer without collisions

since the mean free path of the epithermal electrons is several hundred meters and is much greater than the connection length from the main plasma to the divertor, which is about 10 m. The epithermal electrons disappear after colliding with the divertor plate. Therefore, the spectrum is asymmetric with respect to the equatorial plane.

It was confirmed that cooling the edge electron temperature by the impurity gas (e.g. CH_4) injection is useful for the reduction of the metal impurity [1]. Figure 4 shows an example of the change of the electron energy spectrum associated with the CH_4 injection. The epithermal electrons decreased considerably, but the bulk electron temperature was reduced only a little.

3.2.2 Particle Flow

The measurement of the particle flow to the divertor is important from a point of view of impurity backflow. We use a directional probe (Fig. 5) consisting of a pair of parallel plane probes which collect particles from both directions simultaneously. Angular distributions of the electron and ion saturation currents are obtained by rotating the probe. The result is depicted in Fig. 6. The pattern is symmetric around $\theta = 0$, which indicates that the plasma flows to the divertor along the magnetic field lines and that a cross-field flow (e.g. E×B flow) is less than the detectable level. The ratios of the ion and electron Larmor radii to the width of the probe are 0.24 and 0.006, respectively, for $T_e = T_i = 20$ eV and the toroidal magnetic field of 15 kG at the position. Therefore, dips appeared in the electron angular distribution at $\theta = \pm 90°$.

Defining J_u/J_d as the ion current density to/from the divertor, respectively, we can calculate the particle flux to the divertor from

$$F_D = \int ds (J_u - J_d) \frac{B_R}{B_T}$$

where $\int ds$ is the integral over the total area at R = 40 cm and B_R, B_T are the radial component of the magnetic field, the toroidal magnetic field, respectively. B_R/B_T was measured by the Hall element. Typical values of B_R/B_T were $(2 \sim 3) \times 10^{-2}$.

Z-profiles of J_u, J_d and $J_u - J_d$ are shown in Fig. 7. The features of the particle flow are as follows: The forward flow exceeds the backward

one outside the separatrix ($Z \sim \pm 4$ cm). Inside the separatrix, the backward flow exceeds the foreward one on the ion side of the divertor. The resultant reverse flow extends to the equatorial plane, connecting to the net foreward flow on the electron side.

The ion side reverse flow is explained with a trapped particle by the magnetic mirror and/or a reflected particle on the divertor plate. A ratio of the collision frequency to the bounce frequency of the trapped particle is in the range of $0.1 \sim 1$. A typical trapped ion makes an excursion through ACE in Fig. 8. The points B and D lie at R = 40 cm, where the measurements are carried out. The reverse flow results when the particle flux in the direction of CD overcomes the flux ED. This may occur if the toroidal drift of the particle is so large that the flux through ABCD exceeds the flux through ED because of a lower plasma density at E. The reverse flow increases in the course of the discharge, since the separatrix shrinks with decreasing I_D/I_P, i.e. the point E in Fig. 8, approaches to R = 40 cm. The above discussion is also valid for the reflected particle from the divertor plate. Therefore, the observed reverse flow may be explained by the toroidal drift of ions, which are back-scattered due to the mirror reflection and/or the wall reflection.

The particle flow velocity V_f can be written as

$$j_u - j_d = n_i \, e \, V_f \qquad (1)$$

where n_i is the ion density.

Figure 6 indicates that $j_d \cong j_\perp$, where $j_\perp$ is the ion saturation current density to the probe set parallel to the flow. This means that the backward flow has a negligible flow velocity. One can write

$$j_d \cong j_\perp = \frac{1}{2} n_i C_s \qquad (2)$$

where C_s is a sound velocity.

From Eqs. (1), (2) and Fig. 6, we obtain $V_f = (0.3 \sim 0.5) \times C_s$. The result agrees with that in FM-1, where the ion sound wave was excited in the plasma, and the flow velocity was determined from its time of flight [6]. In DIVA, however, excitation of the ion sound wave in the scrape-off layer is difficult because of $T_i \cong T_e$.

3.2.3 Cross-field Diffusion

The cross-field diffusion coefficient in the scrape-off layer is closely related to the divertor efficiency. The diffusion coefficient $D_\perp$ in the divertor region is experimentally estimated as follows: Figure 9 shows a conceptional diagram of the measurement of the diffusion coefficient. The evolution of the density profile from the point source (width h) along the field line was measured. The actual experimental geometry is shown in Fig. 10. The edge of the movable shell was used as a toroidal limiter. Ion saturation current profiles were measured by the electrostatic probes 1, 2 for various locations of the movable shell in the Z-direction (Fig. 11). The difference between each pair (e.g. S4 - S10 and S7 - S10) of the ion saturation current profile by each probe gives the evolution of the density profile from the point source at the edge of the movable shell (Fig. 12).

One can calculate the diffusion coefficient from the obtained profiles as follows. The equation of continuity of the particle flux in the steady-state is

$$\frac{\partial \Gamma_x}{\partial x} + \frac{\partial \Gamma_Z}{\partial Z} = 0 \tag{3}$$

where x is a co-ordinate along the field line. $\vec{\Gamma}$ is written using a flow velocity V_f along the field line.

$$\vec{\Gamma} = nV_f \vec{e}_x - D_\perp \frac{\partial n}{\partial Z} \vec{e}_Z \tag{4}$$

Substituting Eq. (4) into Eq. (3), we obtain

$$V_f \frac{\partial n}{\partial x} = D_\perp \frac{\partial^2 n}{\partial Z^2}$$

The solution is

$$n(x_j, Z) = \frac{n_o}{\sqrt{4\pi D_\perp x_j / V_f}} \exp\left\{- \frac{(Z-Z_{oj})^2}{4D_\perp x_j / V_f}\right\} \tag{5}$$

$$n(0, Z_{oj}) = n_o$$

where the suffix j (j = 1, 2) corresponds to the probe 1, 2.

$4D_\perp x_j/V_f$ and Z_{oj} are determined from Fig. 12 by the least square method. We can calculate $D_\perp$ from

$$D_\perp = (C_2^2 - C_1^2) \cdot \frac{V_f}{\ell} \tag{6}$$

where $C_j^2 = 4D_\perp x_j/V_f$ and $\ell = x_2 - x_1$. The results are tabulated in Table 1. We obtain $D_\perp = (0.8 \sim 1.3) \times 10^3$ cm^2/s, which is 0.1 $\sim$ 0.2 of the Bohm diffusion coefficient defined by $D_B = \frac{T_e}{16eB}$.

Parameter dependence of the diffusion coefficient was investigated by measuring the divertor efficiency for the particle flux. The divertor efficiency η_p is defined as

$$\eta_p = F_D/F_P \tag{7}$$

F_D and F_P are respectively the particle flux to the divertor and the total particle flux to the shell, the limiter and the divertor. The measurement of F_D and F_P is described in the next subsection.

Using Eq. (5), η_p is calculated as

$$\begin{aligned}\eta_p &= 2 \int_0^\Delta \sqrt{\frac{V_f}{4\pi D_\perp L}} \exp(-\frac{V_f\, x^2}{4D_\perp L})dx \\ &= \mathrm{Erf}(\sqrt{\frac{\Delta^2\, V_f}{4D_\perp L}}) \\ &\equiv \mathrm{Erf}(y)\end{aligned} \tag{8}$$

where Δ is a width of the scrape-off layer at the shell edge and L is a half length of the magnetic field line connecting the shell edges on the electron and ion sides.

Assuming $D_\perp \sim \frac{1}{10} D_B$, $V_f \sim 0.3C_s$, $L \sim \pi qR$ and $\Delta \sim 1$ cm, y is reduced to

$$y^2 = I_p(\mathrm{kA}) \times \sqrt{\frac{100}{T_e(\mathrm{eV})}} \tag{9}$$

Figure 13 shows η_p versus y^2. It is shown that the diffusion coefficient has the functional dependence of the Bohm diffusion.

3.2.4 Particle Flux to the Wall

We describe the measurement of the charged particle flux to the wall.

In DIVA, the shell, the limiter and the divertor plate are used as a collecting electrode. It was found that a large d.c. bias voltage on the shell prevents the initiation of the tokamak discharge. Hence, we use a pulsed bias to obtain the saturation characteristics. Figure 14 shows a current versus voltage characteristic curve of one of the shells at a prescribed time in the discharge, where the opposite electrode is the vacuum chamber. Total particle fluxes to the shells were measured as shown in Fig. 15. In this case, each shell was biased negatively with respect to one another.

Figure 16 shows an example of the ion saturation current to the various components in the device. The divertor efficiency amounts to about 10 % in this case.

Knowing the total particle flux F_p from the plasma column and the total number of confined particles N, we can estimate the average particle confinement time τ_p.

$$\tau_p = \frac{N}{F_p} \tag{10}$$

Time variation of τ_p from Eq. (10) is shown in Fig. 17 together with τ_p from the H_α line measurement. In the first half of the discharge, both values of τ_p agree with each other. The discrepancy in the latter half may be due to impurities since τ_p from Eq. (10) includes the effect of impurity ions but another does not, and it was reported that the metal impurities increased in the latter half of the discharge [7].

3.3 Scaling Law

The energy and particle conservation laws give the following simple formula for plasma parameters in the scrape-off layer, i.e. the electron temperature, T_{es}, the width of the scrape-off layer, d, the electron density, n_{es}, the particle flux density, f_p and the heat flux density, q.

$$\bar{T}_{es} = \frac{\tau_p}{\tau_E} \cdot \frac{3}{2\bar{\gamma}} \cdot \frac{P_{in}-(P_R+P_{cx})}{P_{in}} \cdot (\bar{T}_e + \bar{T}_i) \tag{11}$$

$$d = \sqrt{D_\perp L/V_f} \tag{12}$$

$$\bar{n}_{es} = \frac{L\bar{n}_e a}{2V_f \tau_p d} \tag{13}$$

$$f_p = n_{es} V_f \tag{14}$$

$$q = \overline{\gamma}\overline{T}_{es} f_p \tag{15}$$

Symbols used in Eqs (11) - (15) are as follows.

P_{in} : Ohmic input power
P_{cx} : charge-exchange loss power
P_R : radiation loss power
τ_p : particle confinement time
τ_E : energy confinement time
$\overline{T}_e$: average electron temperature of the main plasma
$\overline{T}_i$: average ion temperature of the main plasma
$\overline{n}_e$: average electron density of the main plasma
a : minor radius
$\overline{\gamma}$: average heat transmission rate
$D_\perp$: cross-field diffusion coefficient
V_f : particle flow velocity
L : half length of a magnetic field line between the material surfaces in the scrape-off layer

$\overline{T}_{es}$, d, $\overline{n}_{es}$, f_p and q can be calculated from these equations if we know V_f, $\overline{\gamma}$, $D_\perp$ and the parameters of the main plasma. The measurements of V_f and $D_\perp$ are discussed in the previous section.

The local heat transmission rate γ is discussed in detail in Chapter 4. Here, the average γ is described.

Equation (11) is rewritten as

$$\overline{\gamma}\,\overline{T}_{es} = \frac{P_{in} - P_{cx} - P_R}{F_P} \tag{16}$$

F_P is the total particle loss flux and its measurement is described in the previous section. $(P_{cx}+P_R)$ is measured by the pyroelectric detector. The detail is described in Chapter 5. Figure 18 shows the relation between the measured electron temperature $\overline{T}_{es}$ near the surface which collects the main part of the heat flux and $\overline{\gamma}\,\overline{T}_{es}$ as calculated from Eq. (16). The result gives $\overline{\gamma}$ = 4 - 10 and is consistent with the value estimated from the sheath model described in Chapter 4. It is shown below that the ratio $\overline{T}_{es}/(\overline{T}_e+\overline{T}_i)$ is determined mainly by $\overline{\gamma}$ for $P_{in} \gg P_{cx} + P_R$.

The relation between energy confinement time τ_E and particle confinement time τ_p is also important in understanding the scrape-off plasma and is shown in Fig. 19. In a conventional discharge, $\tau_p/\tau_E \approx 1.5$. By operating the divertor, τ_E increases and $\bar{\tau}_p$ does not change substantially, thereby decreasing the ratio to $\tau_p/\tau_E \approx 0.8$.

The scrape-off layer plasma and the relation between particle confinement time and energy confinement time were investigated; the following results were obtained: $V_f \approx 0.3\ C_s$, $\tau_p/\tau_E \approx 1$, $D_\perp \approx 0.1\ D_B$ and $\bar{\gamma} \approx 7$. Thus, Eq. (11) is simplified as follows:

$$\bar{T}_{es} \approx 0.2 \frac{(P_{in} - P_{cx} - P_R)}{P_{in}} (\bar{T}_e + \bar{T}_i) \qquad (17)$$

This equation shows that temperature at the edge is extremely high in a high-temperature tokamak with $P_{in} >> P_{cx} + P_R$, and it is expected that surface erosion and impurity production become serious. Thus, some method of cooling the plasma edge down to a sufficient low temperature, typically several tens of electron-volts, is required, as discussed in Ref. [8]. The other important parameters, i.e. the line density of the scrape-off layer plasma $\bar{n}_{es}d$, is given by Eq. (13) by specifying device parameters. For example, the following parameters are assumed: $R = 5$ m, $a = 1.5$ m, $\bar{n}_e = 6 \times 10^{13}$ cm^{-3}, $\bar{\tau}_p = 1$ s, an ideal poloidal limiter and $\bar{T}_{es} = 50$ eV with some cooling method. The line density is about 1×10^{13} cm^{-2}. This value is considered to be high enough to shield the impurity influx because a shielding effect due to a plasma with a lower line density, i.e. $\lesssim 5 \times 10^{12}$ cm^{-2}, is observed in the present experiment. However, this value seems too low to shield the hydrogen influx because charge-exchange process and wall reflection give a relatively high energy for the neutral particles [9].

3.4 Summary

The scrape-off layer plasma was investigated experimentally. The following results were obtained.

(1) The electron and ion temperatures roughly agree.
(2) The epithermal electrons appear on the electron side of the divertor in the low density discharge.
(3) Outside the separatrix, particles flow to the divertor along the field line.

(4) Inside the separatrix, the reverse flow is observed on the ion side. It is explained by the toroidal drift of ions, which are back-scattered due to the mirror reflection and/or the wall reflection.

(5) The particle flow velocity $V_f = (0.3 \sim 0.5)C_s$.

(6) The cross-field diffusion coefficient $D_\perp = (0.1 \sim 0.2)D_B$, having the functional dependence of the Bohm diffusion.

(7) The total particle flux F_p to the wall was measured by the pulse bias method. The average particle confinement time is estimated from F_p and the total number of electrons N.

(8) An empirical scaling of the plasma parameters in the scrape-off layer is obtained.

References

[1] Nagami, M., Maeda, H., Kasai, S., Yamauchi, T., Sengoku, S., et al., J. Nucl. Mat. 76 & 77 (1978) 521; Nagami, M., Divertor Experiment for Impurity Control in DIVA, Japan Atomic Energy Research Institute Report JAERI-M 8215 (1979).

[2] Bohm, D., The Characteristics of Electrical Discharge in a Magnetic Field, Chapter 3. McGraw-Hill New York (1949).

[3] Odajima, K., Kimura, H., Maeda, H., Ohasa, K., Jpn. J. Appl. Phys. 17 (1978) 1281.

[4] Shimomura, Y., Maeda, H., Ohtsuka, H., Kitsunezaki, A., Nagashima, T., et al., Phys. Fluids 19 (1976) 1635.

[5] Yamamoto, S., Sengoku, S., Kimura, H., Shimomura, Y., Maeda, H., et al., Nucl. Fusion 18 (1978) 205.

[6] Hsuan, H., Okabayashi, M., Ejima, S., Nucl. Fusion 15 (1975) 2.

[7] Maeda, H., Ohtsuka, H., Shimomura, Y., Yamamoto, S., Nagami, M., et al., in Plasma-Wall Interaction (Proc. Int. Symposium, Jülich, 1976) Pergamon Press, Oxford (1977) 537.

[8] Nagami, M., Shimomura, Y., Maeda, H., Ohtsuka, H., Shiho, M., et al., Nucl. Fusion 18 (1978) 529.

[9] Fielding, S.J., McCracken, G.M., Erents, S.K., Pospieszczyk, A., Stott, P.E., in Controlled Fusion and Plasma Physics (Proc. 8th Europ. Conf. Prague, 1977) Vol.1 (1977) 39; Wagner, F., Mayer, H.M., ibid. 24.

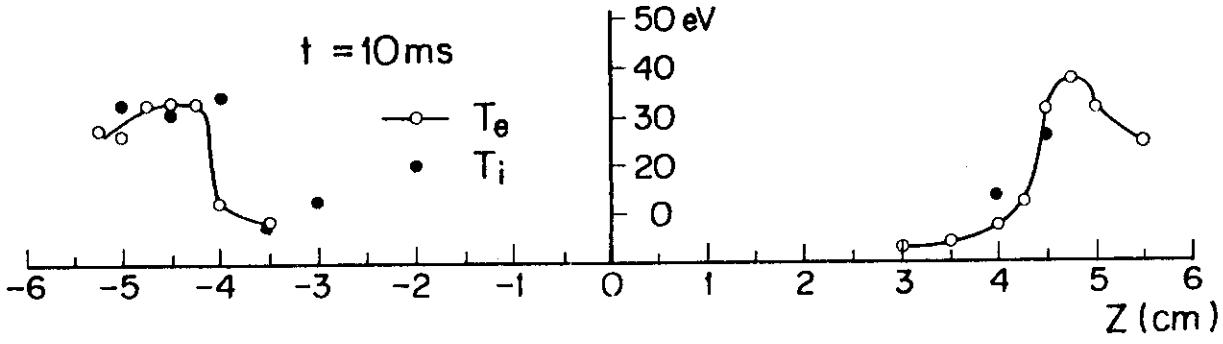

Fig. 1 Z-profiles of the electron and ion temperatures measured by the multigrid energy analyzer at R = 40 cm in the divertor region. B_T = 10 kG, I_P = 15 kA and I_D/I_P = 1.2

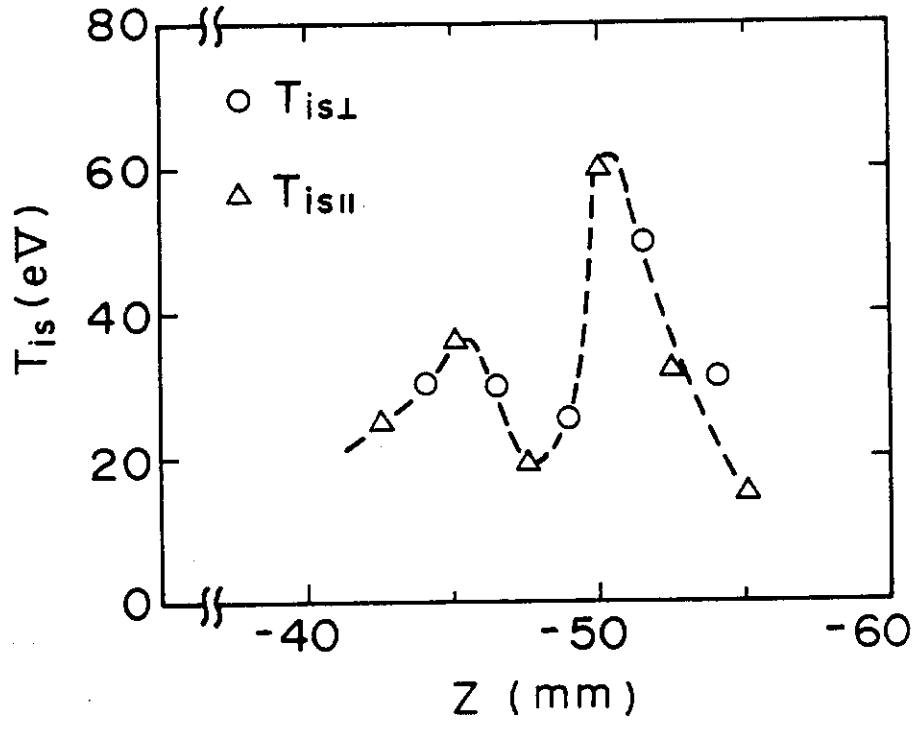

Fig. 2 Z-profiles of the perpendicular and parallel ion temperatures measured by the Katsumata probe and the multigrid energy analyzer, respectively, at R = 40 cm. B_T = 20 kG, I_P = 40 kA and I_D/I_P = 1.2.

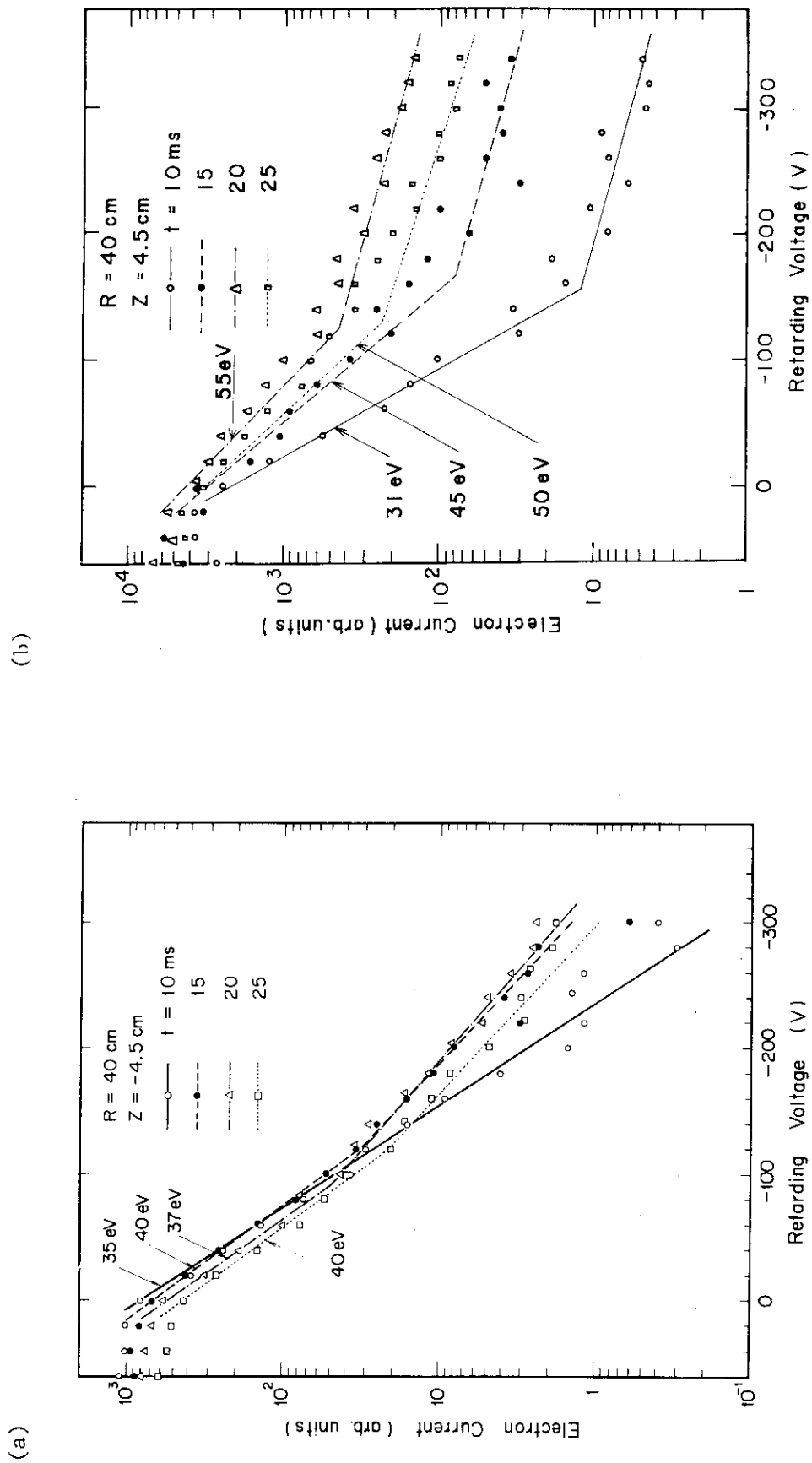

Fig. 3 Energy spectra of electrons near the separatrix magnetic surface in the divertor region;
(a) on the ion side, (b) on the electron side of the divertor.
The discharge condition is same as in Fig. 1.

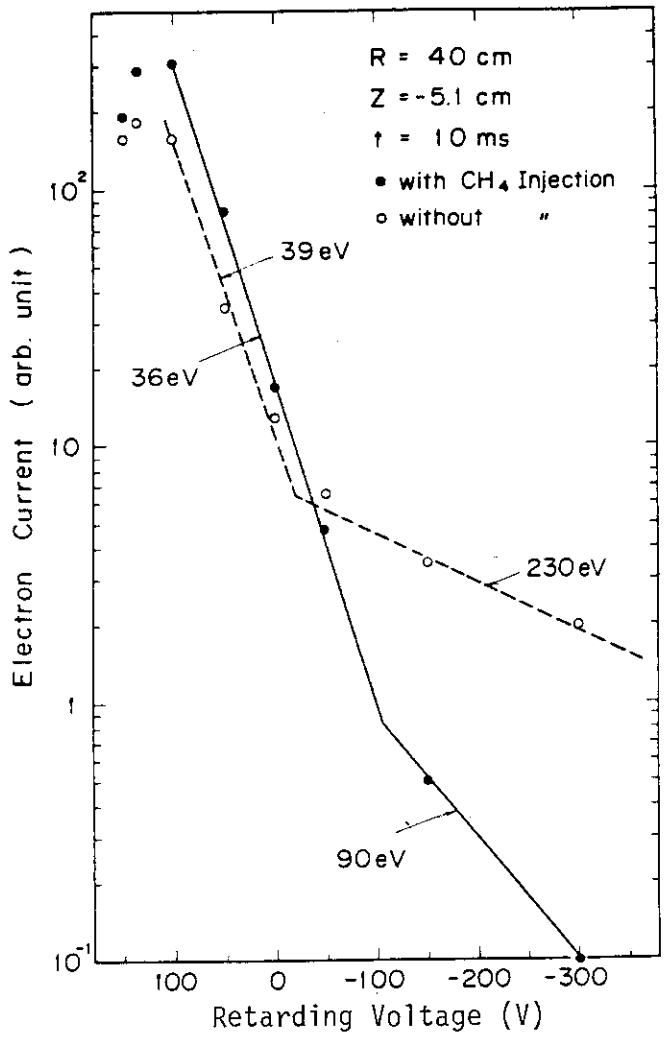

Fig. 4 Change of the electron energy spectrum associated with the CH_4 injection, measured by the multigrid energy analyzer. B_T = 20 kG, I_P = 30 kA and I_D/I_P = 1.56.

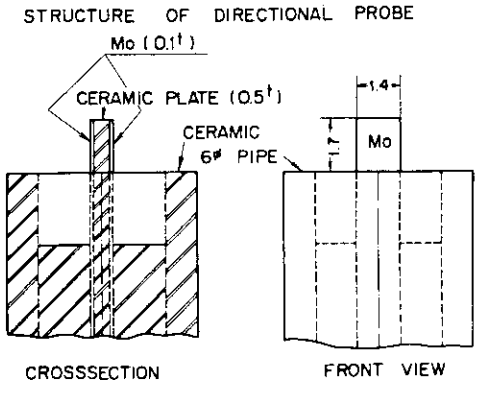

Fig. 5 Directional probe

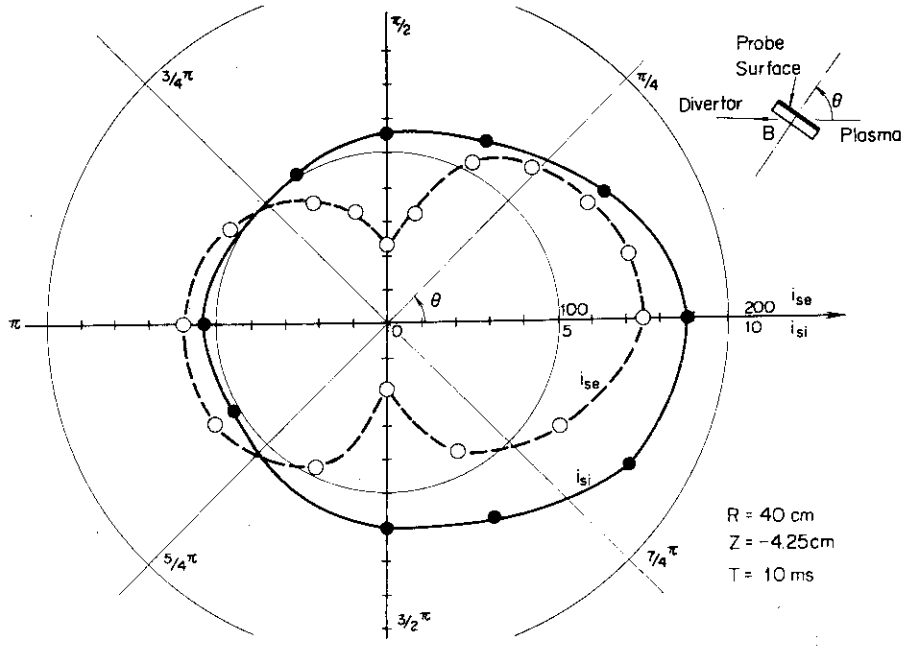

Fig. 6 Ion and electron saturation currents obtained by rotating the directional probe around its axis in the divertor region.

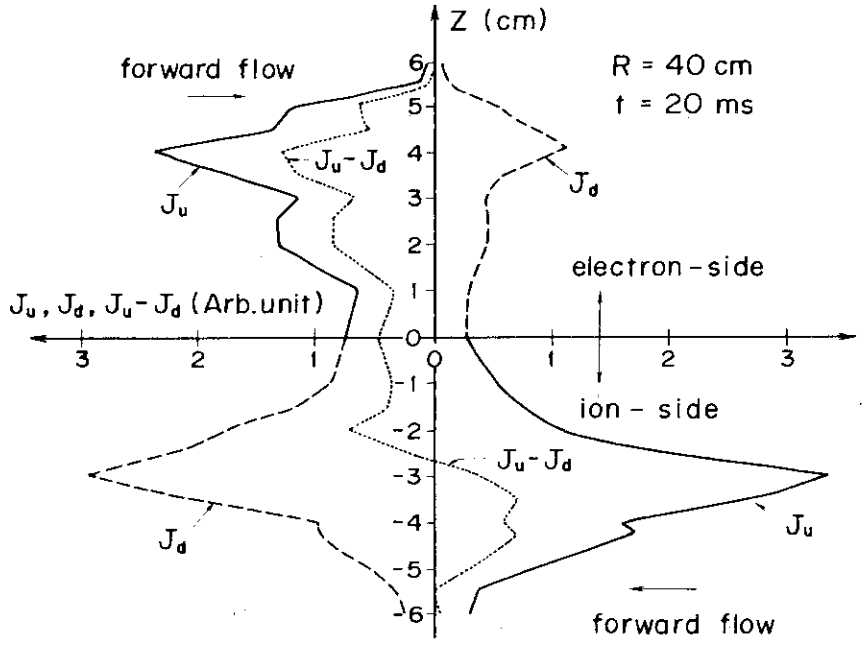

Fig. 7 Z-profiles of the ion saturation current to and from the divertor, J_u and J_d, and their difference J_u-J_d, measured by the directional probe at R = 40 cm and t = 20 ms.

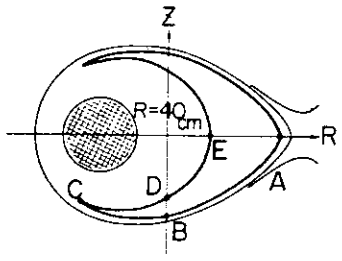

Fig. 8 An example of the orbit of a trapped ion. The calculation was done assuming the drift approximation, no toroidal electric field and $V_{\perp}/V_{\parallel}$ = 2 at A with an energy of 20 eV.

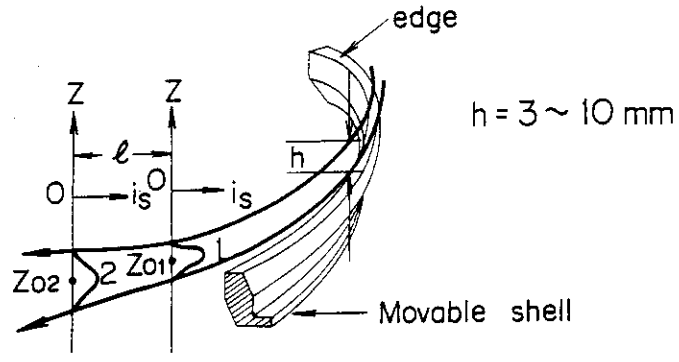

Fig. 9 Conceptional diagram of the measurement of the diffusion coefficient in the divertor region.

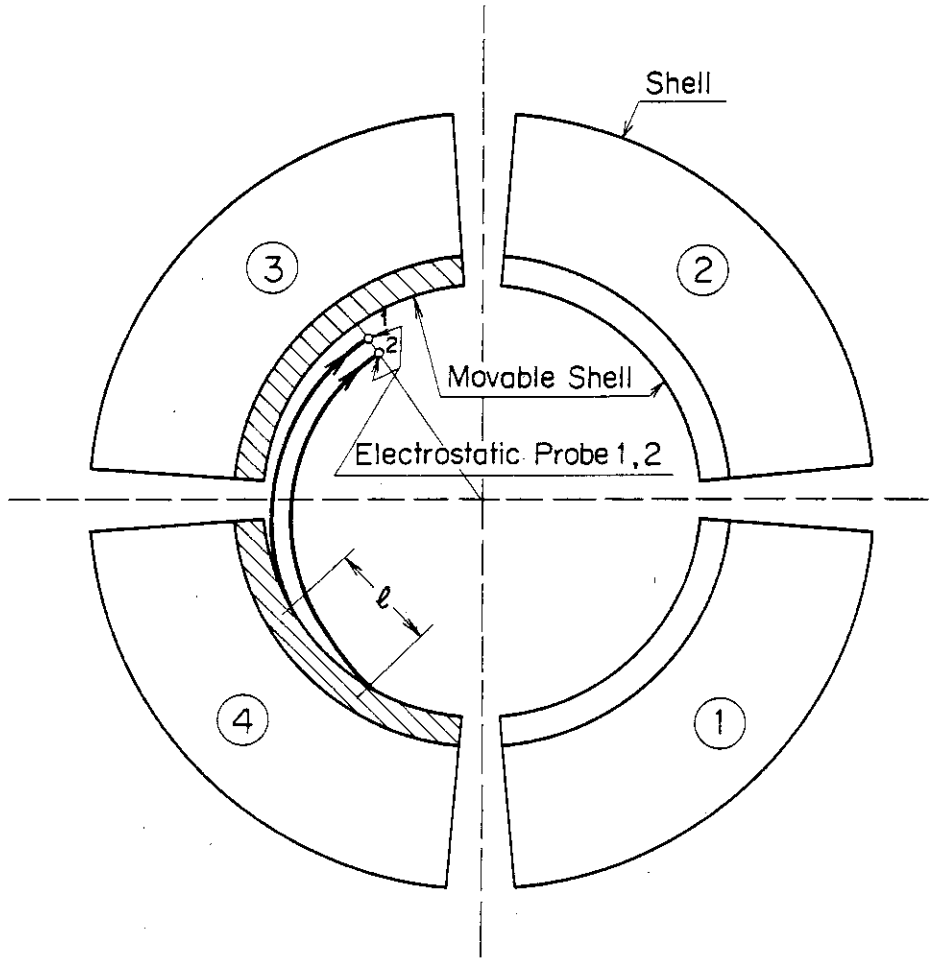

Fig.10 Actual experimental geometry of the measurement of the diffusion coefficient in the divertor region.

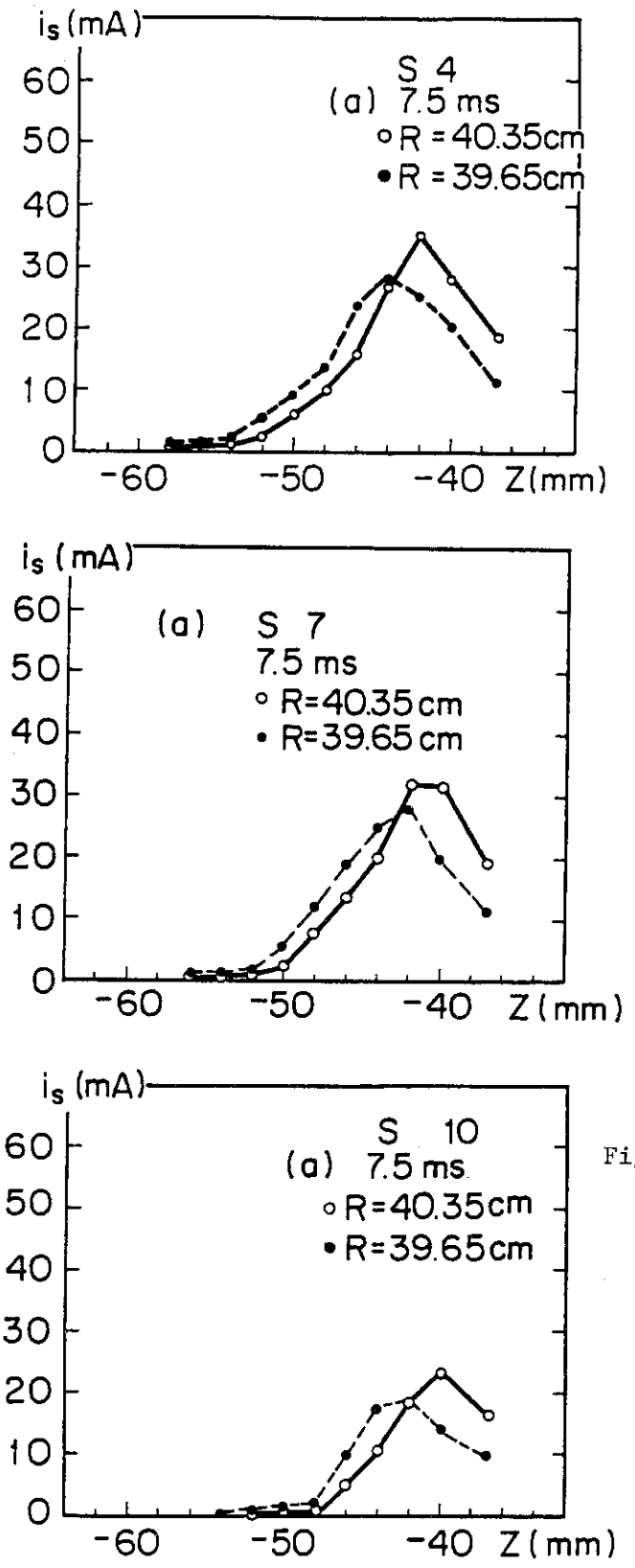

Fig.11 Z-profiles of the ion saturation currents measured by the electrostatic probe 1 and 2, which are scanned vertically along R = 39.65 cm and 40.35 cm, respectively. S4, S7 and S10 indicate the position of the movable shells, e.g. they are shifted 4 mm inwardly from the normal position (Z = -45.5 mm) for S4.

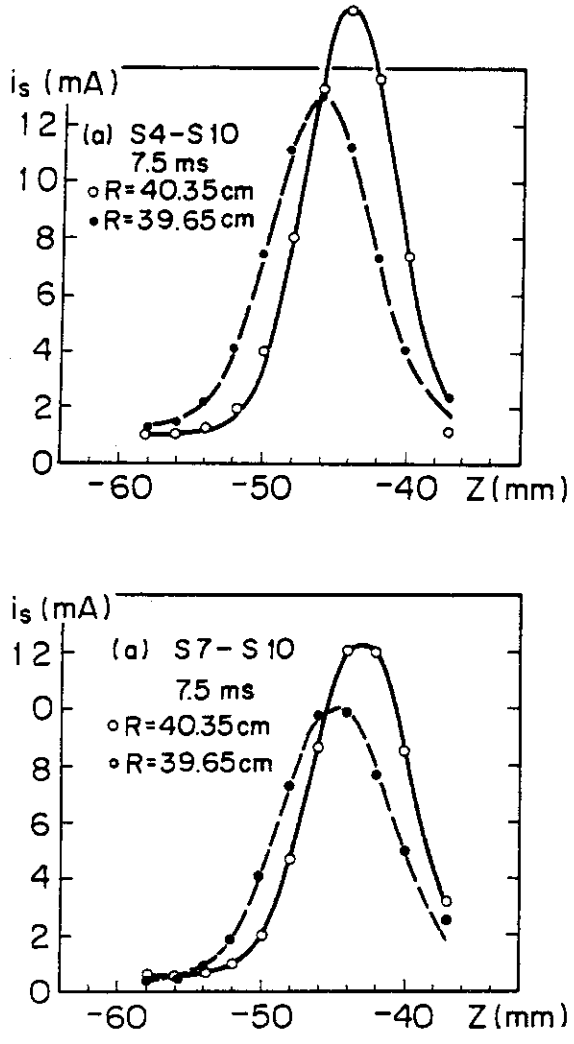

Fig.12

Evolutions of the ion saturation current profile from the point source at the edge of the movable shell. They are obtained as the difference between S4, S10 and S7, S10 in Fig. 11. The solid and broken lines are best fitting curves to Eq. (5) by the method of the least squares.

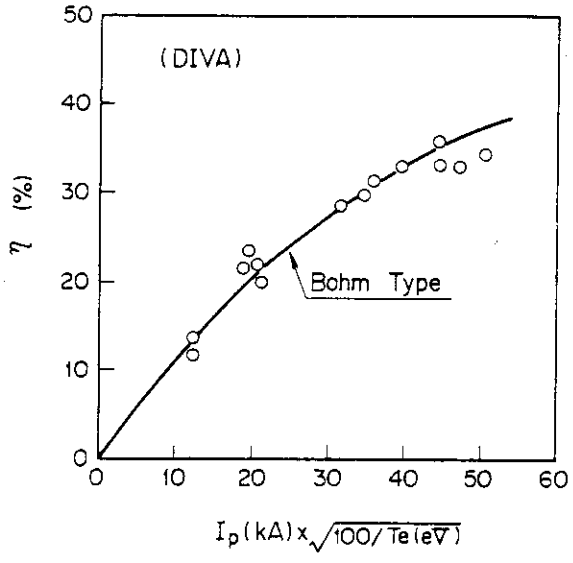

Fig.13

Particle divertor efficiency η. B_T = 0.8T - 2.0T, n_{es} = (1.5-5.0) × 10^{12} cm^{-3} and T_{es} = 20 - 100 eV.

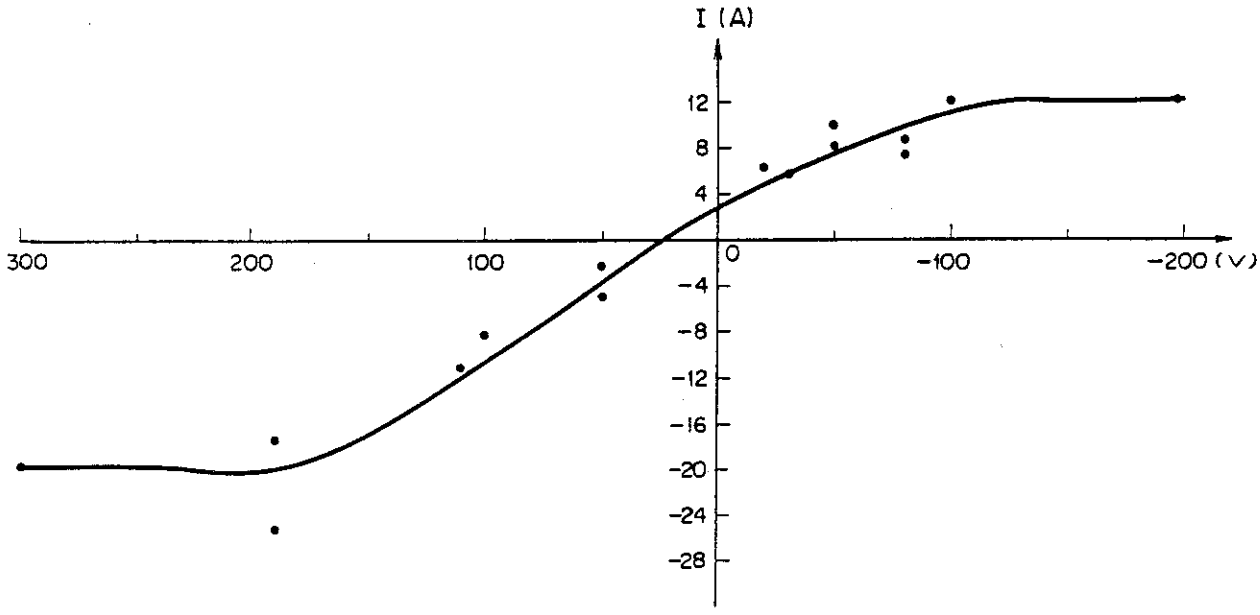

Fig.14 An example of the current characteristic curve of one of the shells. The vacuum chamber is used for the opposite electrode.

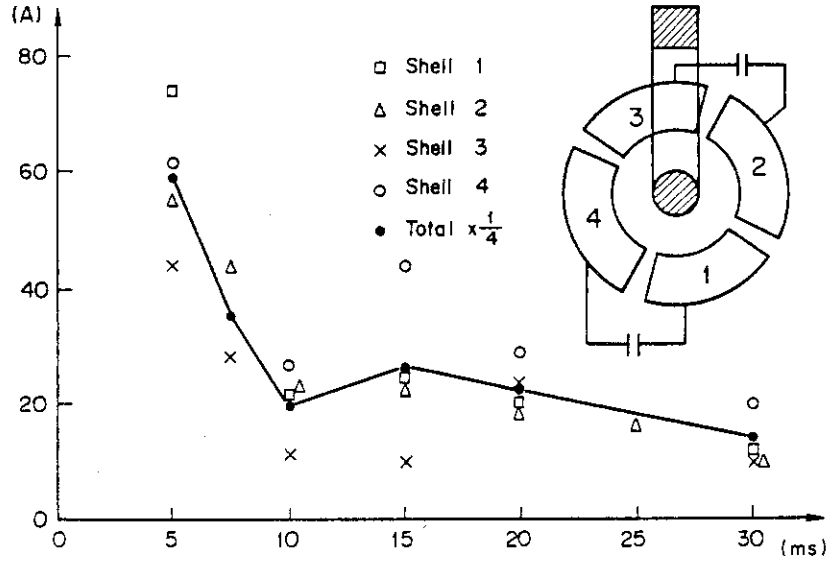

Fig.15 Time evolutions of the ion saturation currents to each sector piece of the shells.

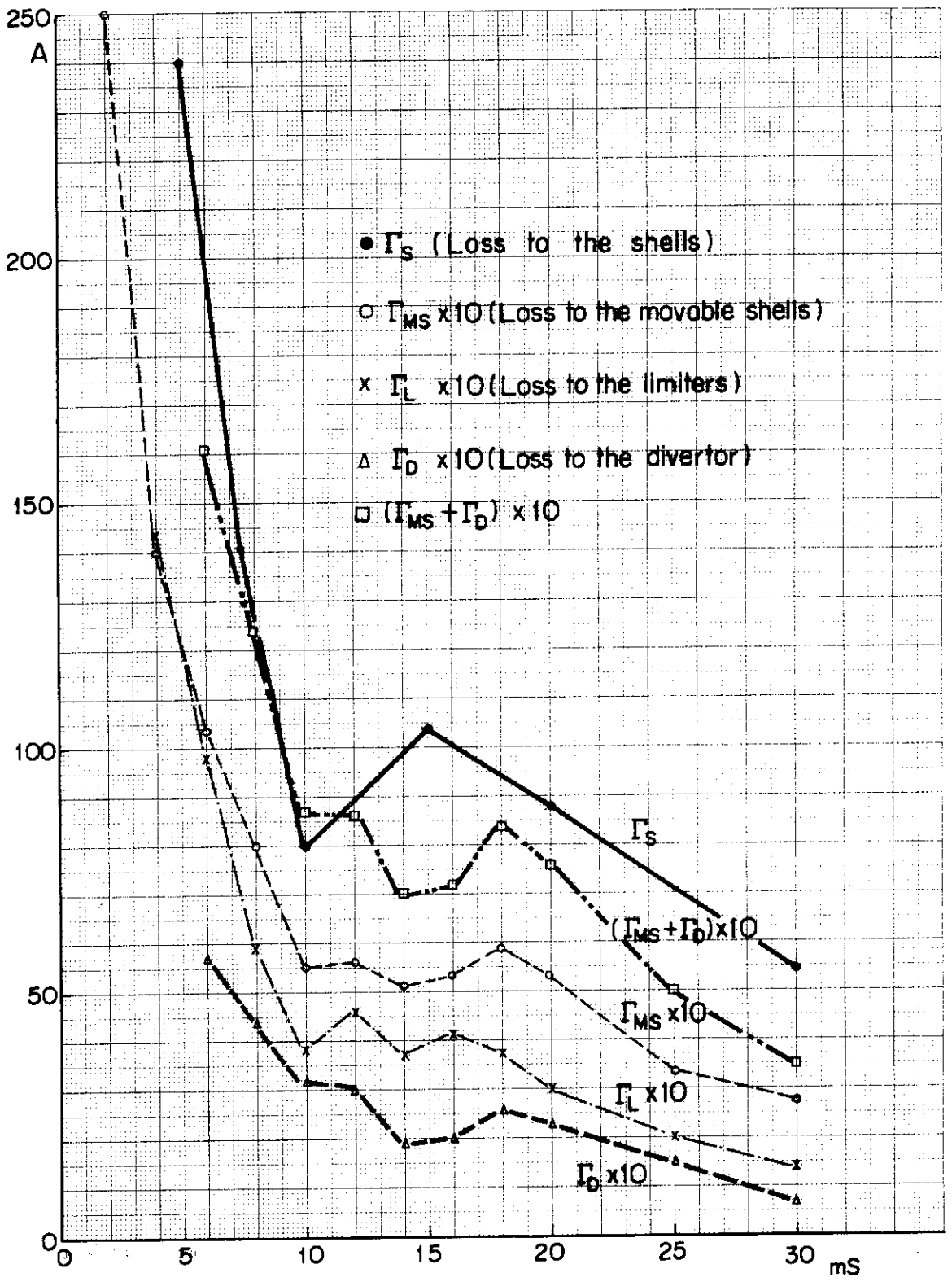

Fig.16 Time evolutions of the ion saturation currents to each component in the device, i.e. the shell, the movable shell, the limiter and the divertor. B_T = 10 kG, I_P = 15 kA and I_D/I_P = 1.1.

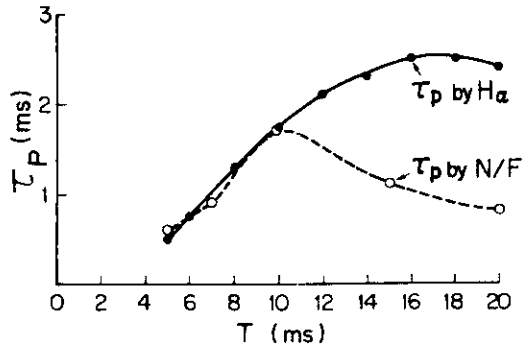

Fig.17 Particle confinement time τ_p obtained by the electrostatic probe method. τ_p by the optical (H_α) method is also shown.

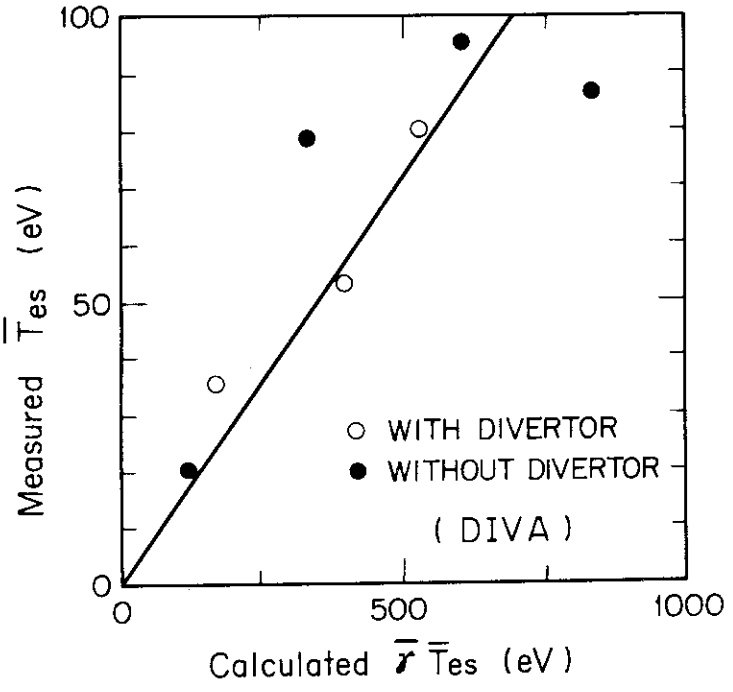

$$\left[\bar{\gamma}\bar{T}_{es} = 1.5 \times \frac{\bar{\tau}_p}{\tau_E}\,\frac{P_{in}-P_{CX}-P_R}{P_{in}}\,(\bar{T}_i+\bar{T}_e) = \frac{P_{in}-P_{CX}-P_R}{F_p}\right]$$

Fig.18 Measured electron temperature $\bar{T}_{es}$ in scrape-off layer plasmas and calculated $\bar{\gamma}\bar{T}_{es}$ from Eq.(16).

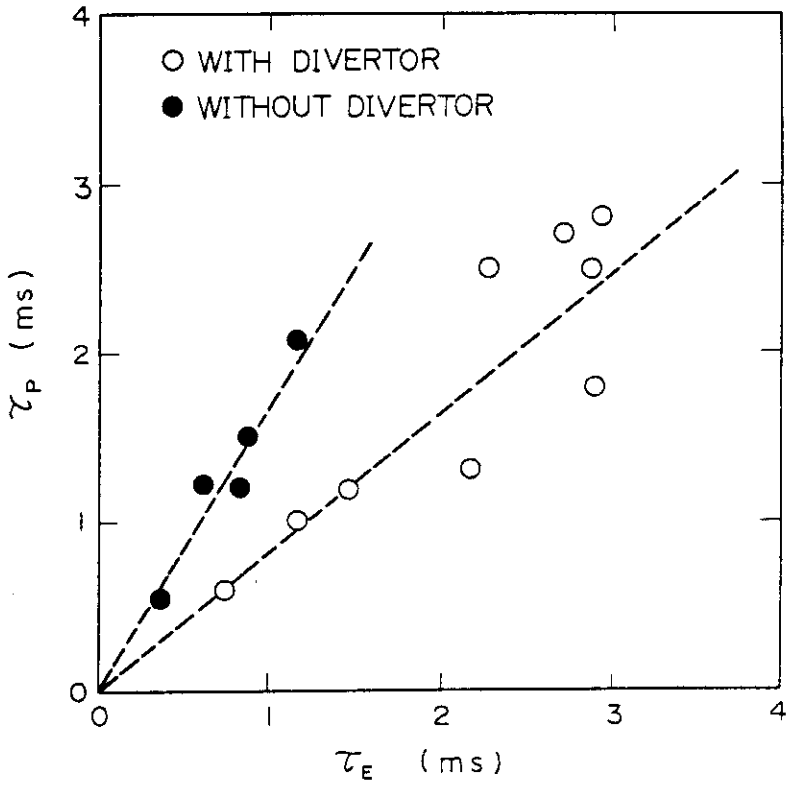

Fig.19 Relation between the particle confinement time τ_p and the energy confinement time τ_E with and without divertor. B_T = 0.8-2.0 T, I_P = 10-53 kA, q_a = 2.6-5.9, $\bar{n}_e$ = (1.5-5.0) × 10^{13} cm^{-3}, T_{io} = 80-300 eV and T_{eo} = 200-700 eV.

Table 1 Results of the measurement of the cross-field diffusion coefficient.
α is a ratio of the flow velocity to the ion sound velocity.

	S4 - S10	S7 - S10
t(ms)	7.5	7.5
C_1^2	4.42	4.75
C_2^2	4.97	5.50
Z_{01} (mm)	44.1	43.0
Z_{02} (mm)	46.0	44.7
Z_0 (mm)	45.1	43.9
B_t/B_p	48.0	37.3
ℓ (mm)	271	266
Te (eV)	20	20
Cs (cm/sec)	4.4×10^6	4.4×10^6
B_Z/B_R	0.28	0.29
$(Z_{01}-Z_{02})/7$	0.28	0.24
$D_\perp(cm^2/sec)$	$2.1\times10^3\alpha$	$3.2\times10^3\alpha$

4. HEAT FLUX TO THE MATERIAL SURFACES IN A TOKAMAK

Heat flux to the material surfaces in the scrape-off layer of a tokamak plasma is investigated experimentally. The time response of heat flux measurement has been improved to 0.2 ms by the recently developed thin-film thermometer. The result shows that the heat flux is calculated from a simple sheath model including secondary electron emission effects even if epithermal electrons are present.

4.1 Introduction

For the design of next-generation large tokamaks, it is important to estimate heat loads to the walls in contact with the plasma, i.e. a limiter and/or a neutralizer plate of a divertor. When the heat fluxes to the walls are so large as to evaporate the structural materials, plasma contamination by metal impurities is significant.

This chapter describes an experimental study on the thermal interaction between plasma and walls in the divertor tokamak, DIVA [1-5]. The other interactions relevant to the release of the metal impurity, such as ion sputtering and arcing, are discussed in Ref. [6].

It is well known that a sheath potential built up in front of an electrically insulated conducting plate plays an important role as a thermal barrier. The heat flux q ($W \cdot cm^{-2}$) towards an electrically insulated conducting plate in a plasma is written as follows [7]:

$$q = \gamma I_s T_e \qquad (1)$$

where I_s ($A \cdot cm^{-2}$) is the ion saturation current density, T_e (eV) is the electron temperature and γ is called a heat transmission rate; and $\gamma = 7.8$ for hydrogen plasma of $T_e = T_i$, where T_i is the proton temperature.

In the scrape-off layer of DIVA, various types of probes have been used successfully [8]. The procedures of the present experiment is to measure the local values of q, I_s and T_e with pertinent probes scanned in the divertor region, and to calculate γ. As noted in previous experiments [3, 5], heat fluxes in the divertor are highly asymmetric about the median plane, and high-energy electrons escaping from the main plasma cause this asymmetry since they can exist on one side of the divertor until they are annihilated at the neutralizer plate. Hereafter, we shall distinguish the two sides of the divertor — with respect to the median plane — as

the electron side and the ion side of the divertor. On the electron side, γ is a few to ten times larger than the value estimated on the basis of Eq. (1). Moreover, even in the case with additional hydrogen gas injection after starting the discharge, γ is a few times larger than expected although the amount of high-energy electrons is considerably reduced. However, the above experiments were somewhat limited in accuracy. The thermo-couple used for heat flux measurements had a response time of 5 ms, which is too long for our experiment since in this time interval the ion saturation current and the electron temperature change considerably. In addition, the use of a Langmuir probe for the measurement of I_s and T_e may be difficult, particularly in the presence of high-energy electrons.

We now report results with our recently developed thin-film thermometer [9-10] with a response time of 0.2 ms, which is short enough for our experiment. As to particle measurement, an electrostatic multigrid energy analyzer is used, which is able to measure I_s and T_e even in the presence of high-energy electrons.

From detailed measurements with these probes, the relationships between heat flux q, heat transmission rate γ and other plasma parameters are obtained. It is found that the thermal interaction between the plasma and the walls in the scrape-off layer can be described by a simple sheath model. These results can be applied to the thermal interaction between the plasma and the limiter in the scrape-off layer of a conventional tokamak [11].

4.2 Thermometer and Multi-Grid Energy Analyzer

The detailed description of the thin-film thermometer is given elsewhere [9-10]. Here it is described only briefly. Figure 1 shows the structure of the thermometer. The backing metal was a thin molybdenum plate of 8 × 12 mm^2 area and 0.1 mm thickness. Silicon monoxide was vacuum-deposited on the molybdenum plate and then nickel was added. The silicon monoxide layer served as an electrical insulator. The molybdenum temperature was measured by the change in resistance of the nickel film. The response time of the thermometer was measured by using a Q-switched pulse laser; it was found to be less than 0.2 ms.

The width of the nickel film is 0.4 mm which is much larger than the thickness of the molybdenum plate. Thus, the spatial resolution of the thermometer is determined by the width of the nickel film.

Figure 2 shows the multigrid energy analyzer schematically. The external jacket of the analyzer is at the same potential as the vacuum vessel. In front of stainless-steel collector plate C, 5 mm in diameter, three stainless-steel grids (E, G_1, G_2) are placed at 1 mm spacings. The grid E with the same potential as the vacuum vessel has seven holes, 100 μm in diameter and 100 μm long, with 1 mm aperture, which determines the spatial resolution of this analyzer. The mesh grids G_1 and G_2 are made of 20- and 50-μm wires and have a transparency of 0.31 and 0.44, respectively.

Figure 2 also shows the potential distributions between the three grids and a collector plate to obtain the ion and electron velocity distributions. The ion saturation currents are obtained by the following procedure, which discriminates against high-energy and secondary electrons: We adopt the potential profile shown in Fig. 2 (a) and subtract the collector signal at +150 V from that at -40 V. The latter consists of the ion saturation current plus the electron leakage current, the former consists of the electron leakage current only, where the term "electron leakage current" applies to electrons which have higher energy than the retarding potential of grid G_2 and succeed in passing grids G_1 and G_2, in addition to those which are emitted at grid G_2 and can reach collector C. It was experimentally confirmed that the electron leakage current is independent of the collector potential unless it is less than the critical potential which is equal to the G_2 potential plus the mean energy of the secondary electrons.

4.3 Experimental Procedure and Results

Figure 3 shows the cross-sectional view of DIVA. The experiment was performed under the following operational conditions: The toroidal magnetic field was fixed at 1 T. The ratio of the divertor hoop current to the plasma current was 1.2, where the latter was 14 kA with a flat-top. The basic pressure was 1×10^{-7} torr, and hydrogen gas of 1.5×10^{18} atoms was admitted by four fast-acting valves, 0.8 ms before starting a discharge. Additional hydrogen gas was injected 2.2 ms after starting the discharge at a rate of 1.7×10^{19} $H_2 \cdot s^{-1}$.

The central electron and ion temperatures were 200 and 80 eV from laser scattering and charge-exchange neutrals, respectively. The average electron density was 1×10^{13} cm^{-3} from a 4 mm μ-wave interferometer.

A thermometer and a multigrid analyzer were scanned vertically at R = 40 cm.

Figure 4 shows typical thermometer data. This figure represents the resistance change of the thin Ni film. The temperature T of the thin film, which is assumed to be equal to that of the molybdenum plate, is obtained from a calibration curve. If the heat flux to the divertor has a very sharp peak in space, we must take the heat conduction in the molybdenum plate into account to calculate the heat flux from the measured temperature [10].

Figure 5 shows the Z-profile of the heat flux calculated by taking the above mentioned effect into account, on the electron side of the divertor. This profile indicates a sharp peak near Z = 45 mm. In this figure, the results from a simple heat balance equation,

$$q(Z,\ t) = \rho c d \frac{dT(Z,t)}{dt} \qquad (2)$$

where ρ, c, and d are density, specific heat and thickness of the molybdenum backing plate, respectively, are also shown.

It is found that the peak value of the heat flux would be underestimated by a factor of 1.5 if Eq. (2) were used. However, only in a narrow region, $\Delta Z \simeq 1$ mm, the effect of transverse heat transfer is dominant. Outside this region, both the results from the simple heat balance equation and the transverse heat conduction equation are in good agreement.

Next, we describe the results of particle measurements. Figure 6 shows the time variation of electron energy spectra at Z = 45 mm. These spectra were obtained by changing the bias voltage of grid G_2 of the multigrid analyzer shot by shot. It was found that relatively high-energy electrons, whose energy range is 100 to 200 eV, exist in a narrow layer on the electron side of the divertor, i.e. Z = 45 $\sim$ 50 mm and that the amount of these electrons varies with time. To examine a much higher range of energy than that of the multigrid analyzer, we scanned an X-ray target [12], whose spatial resolution is 1 mm, on the electron side of the divertor. The X-ray energy observed with 100 % efficiency ranges approximately from 10 to 100 keV, as determined by the thickness of the aluminum window and the NaI scintillator. Figure 7 shows the Z-profile of the X-ray intensity I_X from the target. The profile of the electron flux whose energy is

higher than 150 eV is also depicted in this figure. The peak position of I_x is 42.5 mm, where the heat flux is much smaller than that of Z = 45.0 mm. It is clear that the peak heat flux has no correlation with the runaway electrons and the peak position rather coincides with the path of the electrons in the 100 - 200 eV range of energy.

The measurement of the ion saturation current density was also made by the procedure described in the previous section. The ion saturation current density and the bulk temperature of electrons are shown in Fig. 5. It is noted here that the measured heat flux is by a factor 2 ∿ 3 higher than the values calculated from Eq. (1) by using the measured ion saturation current density and the bulk temperature of electrons.

4.4 Discussion

It is natural that this relatively high heat flux is due to the electrons in the 100 - 200 eV range of energy. Hereafter, we shall call these electrons epithermal. The loss mechanism of the epithermal electrons from the main plasma column is discussed in Ref. [12]. To confirm the relationship between heat flux and epithermal electrons we make some simple analysis following Lovberg [7]. We assume the electron velocity distribution to be a two-component Maxwellian, i.e.

$$n_e = \sum_{k=1}^{2} n_{ek} \left(\frac{m}{2\pi T_{ek}}\right)^{1/2} \exp\left(-\frac{mV_{//}^2}{2T_{ek}}\right) \qquad (3)$$

where n_e and m are the density and the electron mass, and subscripts 1 and 2 refer to the low- and high-energy components, respectively. Furthermore, we make two assumptions: 1) Ion temperature T_i is equal to T_{e1}. This held roughly true in the scrape-off layer due to a multi-grid analyzer. 2) Secondary electrons are emitted from the backing plate of the thermometer. These are induced by electron impact only. The secondary-electron emission coefficient on a molybdenum surface, δ(electrons/electron), is taken from Ref. [13]. The data in Ref. [13] are given for monoenergetic electrons. In the present analysis, however, we adopt the mean energy for the incident energy of the primary electrons. This treatment seems to be correct because δ can be derived from Eq. (4) if the potential difference between the plasma and the electrically insulated plate is known, and it is experimentally confirmed that δ obtained in this way is in good agreement with the data in Ref. [13] for various plasma parameters,

i.e. $T_e = 20 \sim 50$ eV.

Ion-induced secondary electrons are not considered here because the secondary-electron emission coefficient due to ion impact on a molybdenum surface is much smaller than that due to electron impact in the energy range considered.

A floating potential ϕ_o of the backing plate, where the space potential is set zero, can be determined by the condition that the net current to this plate is equal to zero, i.e.

$$\sum_{k=1}^{2} \frac{1-\delta_k}{4} n_{ek} \left(\frac{8T_{ek}}{\pi m}\right)^{1/2} \exp \frac{e\phi_o}{T_{ek}} = \frac{\xi}{4} n_o \left(\frac{8T_i}{\pi M}\right)^{1/2} \quad (4)$$

where n_o is the ion density, M is the ion mass and ξ a correction factor of the electron-to-ion saturation current ratio in a strong magnetic field. ξ was measured by a plane probe for the scrape-off layer plasma in DIVA and has a value of $2 \sim 4$. Typical data for T_{e1}, T_{e2}, corresponding secondary emission coefficients δ_1, δ_2 and n_{e1}/n_o at Z = 45 mm, t = 20 ms are 55 eV, 198 eV, 0.59, 0.98 and 0.083, respectively. The calculated ϕ_o using $\xi = 3$ at 20 ms is shown in Fig. 7. The heat flux to the thermometer can be written as

$$q = I_s T_{e1} \left[\frac{2}{\xi}\sqrt{\frac{M}{m}} \left\{(1-\varepsilon)\exp \frac{e\phi_o}{T_{e1}} + \varepsilon h^{3/2} \exp \frac{e\phi_o}{T_{e2}}\right\} + 2 - \frac{e\phi_o}{T_{e1}}\right] \quad (5)$$

where $h = T_{e2}/T_{e1}$, $\varepsilon = n_{e2}/n_o$ and $I_s = \frac{1}{4} n_o \left(\frac{8T_i}{\pi M}\right)^{1/2}$.

This may be compared with the heat flux in the absence of a high-energy tail, by rewriting it in the from

$$q = F\gamma I_s T_{e1} \quad (6)$$

$$\gamma = 2\left(\frac{1}{1-\delta_1} + 1\right) - \ln \frac{\xi\sqrt{\frac{m}{M}}}{1-\delta_1} \quad (7)$$

where γ is the heat transmission rate in the absence of a high-energy tail, equal to $6.7 \sim 8.6$ for hydrogen plasma with $T_{e1} = 7 - 55$ eV and $\xi = 3$, and F is the correction factor for the two-component model.

For the parameter range of the present experiment, i.e. $h \lesssim 4.0$ and $\varepsilon \lesssim 0.1$, the low-energy term in the left-hand side of Eq. (4) is dominant. In this case, $e\phi_o$ and F are approximately written as follows:

$$e\phi_o \simeq T_{el} \ln \frac{\xi\sqrt{\frac{m}{M}}}{(1-\delta_1)(1-\varepsilon)} \tag{8}$$

$$F \simeq \frac{1}{\gamma}\left[2\left(\frac{1}{1-\delta_1}+1\right) + \frac{2}{\xi}\sqrt{\frac{M}{m}}\,\varepsilon\, h^{3/2}\left\{\frac{\xi\sqrt{\frac{m}{M}}}{(1-\delta_1)(1-\varepsilon)}\right\}^{1/h} - \frac{e\phi_o}{T_{el}}\right] \tag{9}$$

These approximate forms of $e\phi_o$ and F are in agreement with the exact value from Eqs. (4, 5) within 10 %, using the measured values of h and ε. Before we compare theory and experiment, we shall estimate the accuracy of the experimental data of the heat flux.

The transverse heat transfer in the backing plate of the thermometer was already discussed in Section 4.3. Another probable error in the measurements is due to the fact that the floating potential of the backing plate of the thermometer is shallower than expected from Eq. (4) since the dimension of the backing plate, 8 mm, is larger than the characteristic length of spatial variation of the floating potential.

If the bias voltage of the thermometer is shallower than the local floating potential, the heat flux is higher than that of a plate at local floating potential. To confirm this statement, the dependence of the heat flux on the bias voltage of the thermocouple sheath (diameter 0.25 mm) was examined. Figure 8 shows the time-integrated heat flux to a thermocouple as a function of the bias voltage with respect to the vacuum chamber.

In this figure, probe characteristics are also depicted. These were obtained by employing a stainless-steel sheath of the thermocouple as an electrode.

The transient heat flux as a function of the bias voltage ϕ is given by substituting ϕ instead of ϕ_o in Eq. (5). It is with this equation that the time-integrated heat flux shown in Fig. 8 is compared although a rigorous comparison would be rather inadequate since both electron temperature and ion saturation current change in time during the discharge.

The minimum heat flux is obtained from the condition $\left.\frac{dq}{d\phi}\right|_{\phi=\phi_m} = 0$, i.e.

$$e\phi_m = T_{el} \ln \frac{\xi}{2}\sqrt{\frac{m}{M}} \tag{10}$$

assuming $\varepsilon = 0$ for simplicity.

The floating potential, by setting the secondary-electron emission coefficient zero, is given as

$$e\phi_o = T_{el} \ln \xi\sqrt{\frac{m}{M}} \tag{11}$$

The difference between the two potentials $\phi_o - \phi_m$ is about 0.7 T_{el}/e, by using $\xi = 6.4$ from the probe characteristics shown in Fig. 8. This is consistent with the experiment, where the minimum heat flux is realized in the vicinity of $e\phi = e\phi_o - T_e$.

Let us estimate how much the heat flux measurement was affected by the above-mentioned effect. For example, we consider the peak heat flux at t = 20 ms (Fig. 5). The calculated local floating potential is -94 V. In this case, $q = 18.5\ I_s T_{el}$, where $\xi = 3$ is assumed. The floating potential of the backing plate of the thermometer placed at Z = 45 mm can be calculated from the equation, integrating Eq. (4) from Z = 41 mm to Z = 49 mm, and is about -85 V. From Eq. (5), q becomes $19.8\ I_s T_{el}$. From this result, it can be said that the heat flux measurement was affected within 10 % because the thermometer was not at local floating potential, and that the influence of this effect is relatively small. We are now in a position to compare theory and experiment.

Figure 9 shows the relationship between heat flux q measured on the electron side of the divertor and the correction factor F calculated exactly from Eqs. (4, 5) by using experimental data for h and ε, and $\xi = 3$.

Heat fluxes are averaged in space over the aperture of the multigrid analyzer. The error bars for q are determined so as to include the widest range between the shot-to-shot deviations and the temporal changes for the neighbouring time steps, $\Delta t = \pm 1$ ms. The error bars for F are due to the ambiguity of ξ. The upper values correspond to $\xi = 2$, the lower ones to $\xi = 4$. The values of q corresponding to F = 1 are those in the absence of epithermal electrons. It is seen that there is a strong correlation between the relatively large heat flux and the presence of epithermal electrons.

The relationship between the measured heat flux q and $F\gamma I_s T_{el}$ is shown in Fig. 10. As a whole, they are in good agreement.

The present experiment was performed under discharge conditions with additional gas injection. The relatively large heat flux on the electron side of the divertor has a strong correlation with the epithermal electrons whose energy range is 100 to 200 eV, and has no correlation with the runaway electrons. If the amount of additional gas was increased, the number and the kinetic energy of the epithermal electrons became small. Hence, the heat flux was also relatively small.

On the other hand, in the case of no additional gas injection, the heat flux becomes very large.

The peak values of the heat flux at 15 ms for three additional gas injection rates are tabulated in Table 1.

4.5 Summary

The thermal interaction between the plasma and an electrically insulated plate in the divertor region of DIVA, where $T_e \lesssim 50$ eV and $n_e \lesssim 1 \times 10^{12}$ cm^{-3}, was investigated experimentally.

The results show that the heat flux to the divertor can be calculated from a simple sheath model including secondary-electron emission effects even if epithermal electrons are present.

This result can be applied to the thermal interaction between the plasma and the limiter in a conventional tokamak.

References

[1] MAEDA, H., OHTSUKA, H., SHIMOMURA, Y., YAMAMOTO, S., NAGAMI, M., et al., in Plasma-Wall Interaction (Proc. Int. Symposium, Jülich, 1976) Pergamon Press, Oxford (1977) 537.

[2] MAEDA, H., FUJISAWA, N., SHIMOMURA, Y., FUNAHASHI, A., OHTSUKA, H., et al., in Plasma Physics and Controlled Nuclear Fusion Research (Proc. 6th Int. Conf., Berchtesgaden, 1976) Vol.2, IAEA, Vienna (1977) 289.

[3] SHIMOMURA, Y., in Controlled Fusion and Plasma Physics, (Proc. 7th Europ. Conf., Lausanne, 1975) 2 (1975) 81.

[4] SHIMOMURA, Y., MAEDA, H., OHTSUKA, H., KITSUNEZAKI, A., NAGASHIMA, T., et al., Phys. Fluids 19 (1976) 1635.

[5] MAEDA, H., SHIMUMORA, Y., KITSUNEZAKI, A., OHTSUKA, H., NAGAMI, M., et al., Nucl. Fusion 16 (1976) 148.

[6] OHASA, K., MAEDA, H., YAMAMOTO, S., NAGAMI, M., OHTSUKA, H., et al., Nucl. Fusion 18 (1978) 872.

[7] LOVBERG, R.H., Plasma Diagnostic Techniques (Huddlestone, R.H. and Leonard, S.L. eds.) Ch. 3, Academic Press New York (1965).

[8] KIMURA, H., NAGAMI, M., YAMAMOTO, S., UEDA, N., OHTSUKA, H., MAEDA, H., SHIMOMURA, Y., Diagnostics of a Scrape-off Layer Plasma, Japan Atomic Energy Research Institute Report JAERI-M 6971 (1977).

[9] UEDA, N., SEKI, M., ANNO, K., KAWAMURA, H., MAEDA, H., Development of a Heat Flux Meter and Measurement of the Heat Flux to the Divertor in DIVA, Japan Atomic Energy Research Institute Report JAERI-M 6723 (1976).

[10] SEKI, M., KAWAMURA, H., UEDA, N., MAEDA, H., J. Nucl. Sci. Technol. 14 (1977) 68.

[11] GOMAY, Y., FUJISAWA, N., MAENO, M., SUZUKI, N., UEHARA, K., et al., Nucl. Fusion 18 (1978) 849.

Table 1 Comparison of heat flux peak values for different additional gas injection rates.

Rate of an additional gas injection	Peak values of heat flux
0 H_2/s	2200 Watts/cm^2
1.7×10^{19}	330
4.5×10^{19}	180

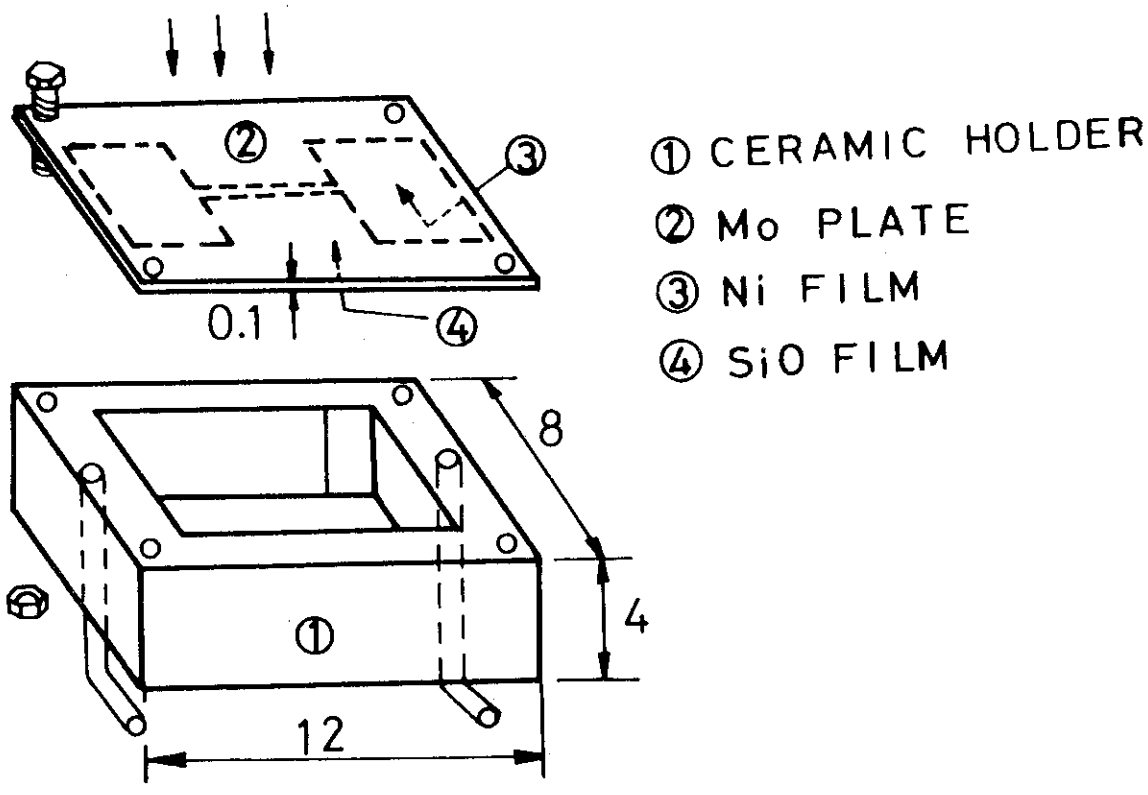

Fig. 1 Schematic drawing of thermometer.

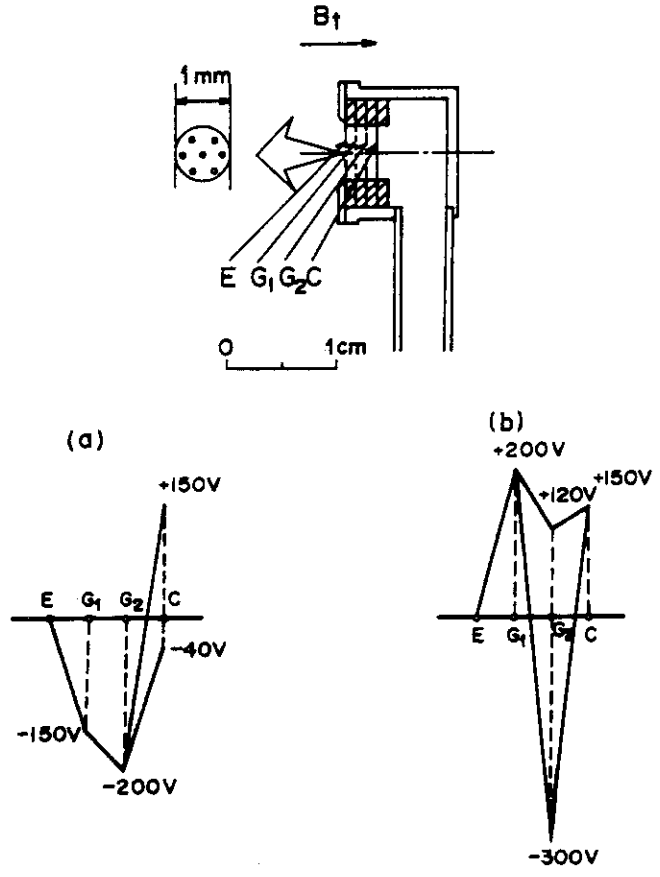

Fig. 2 Schematic drawing of electrostatic multigrid energy analyzer and potential distribution between grids E, G_1, G_2 and collector C for (a) ion and (b) electron energy analysis.

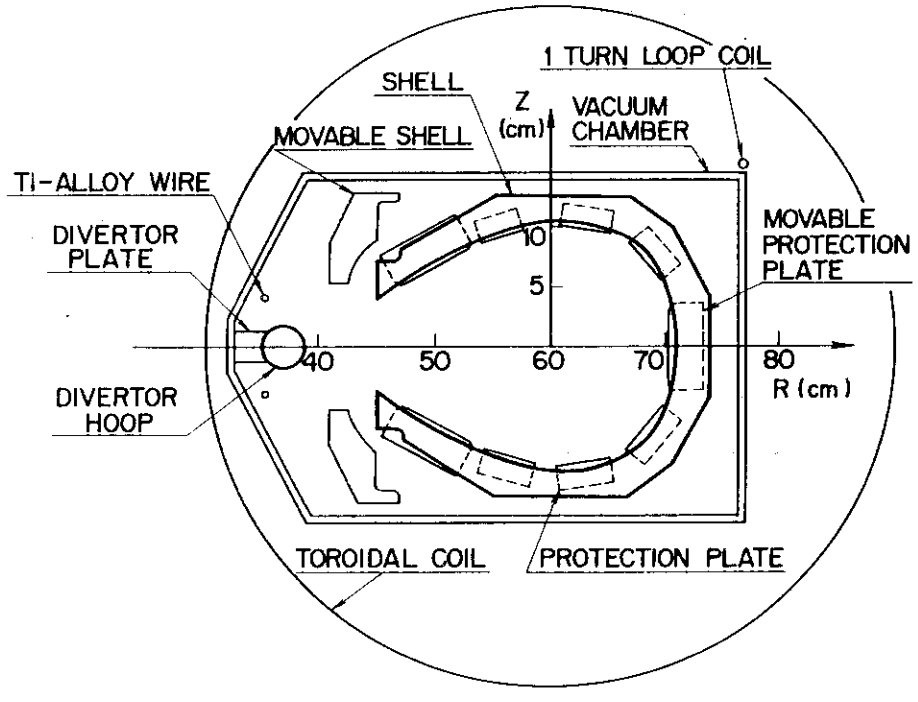

Fig. 3 Cross-sectional view of DIVA.

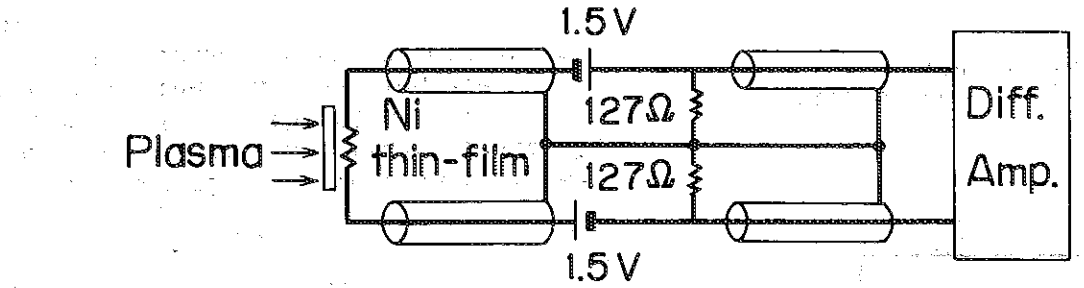

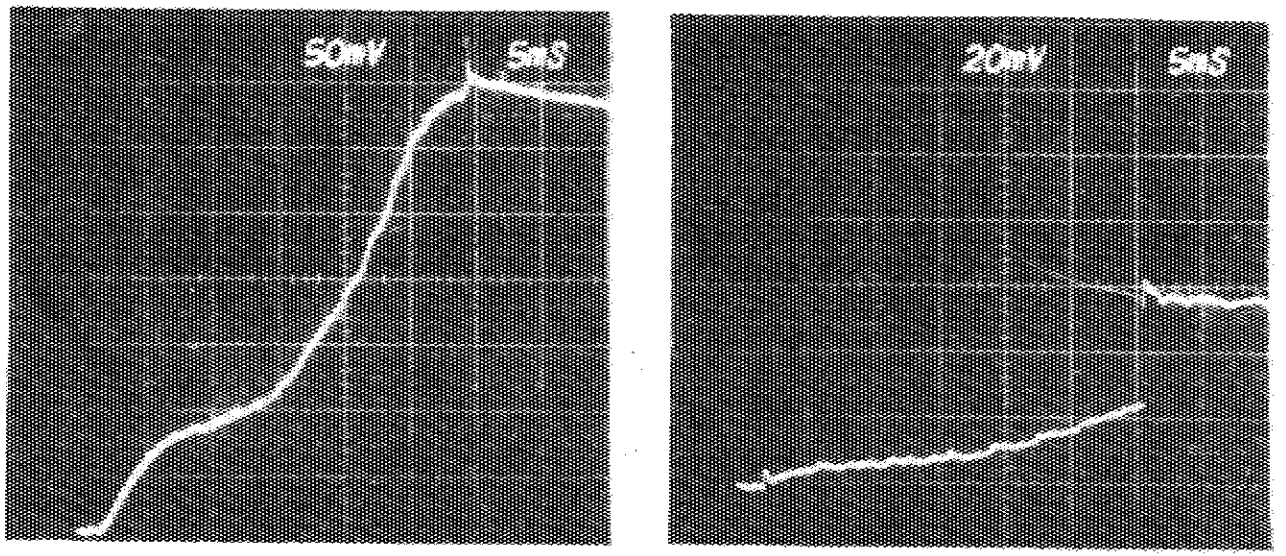

(a) R = 40 cm
Z = 4.5 cm

(b) R = 40 cm
Z = 3.0 cm

Fig. 4 Outputs of thermometer located at different positions.

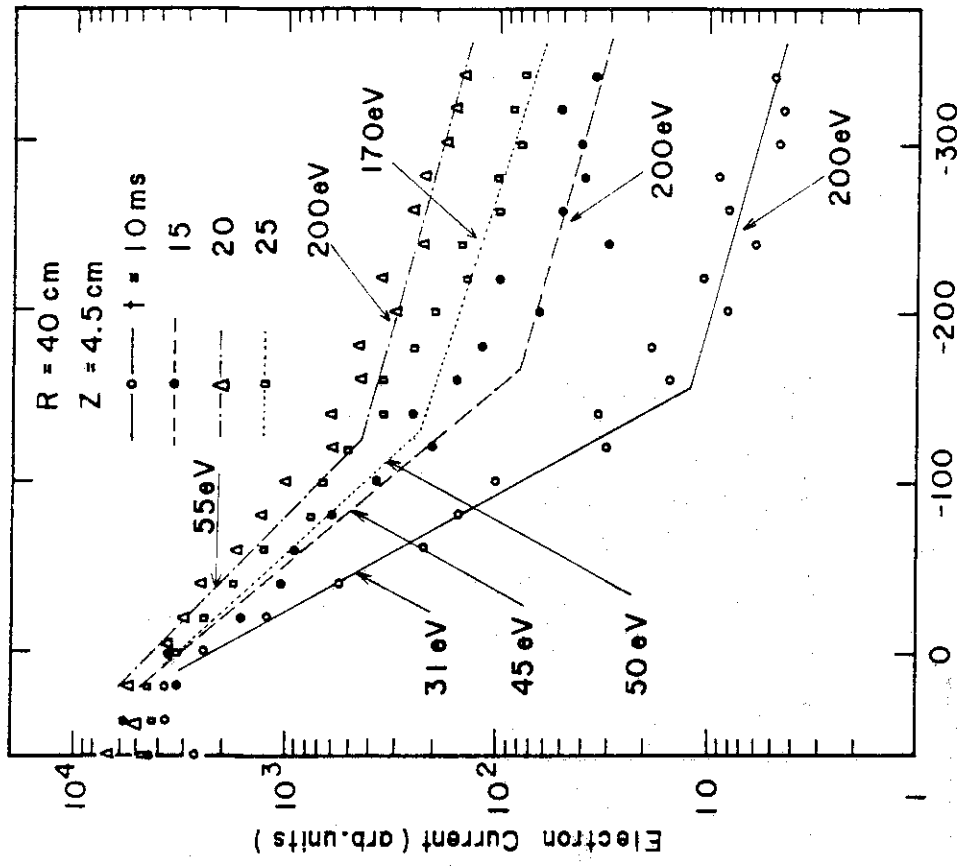

Fig. 6 Energy spectra of electrons on the electron side of the divertor.

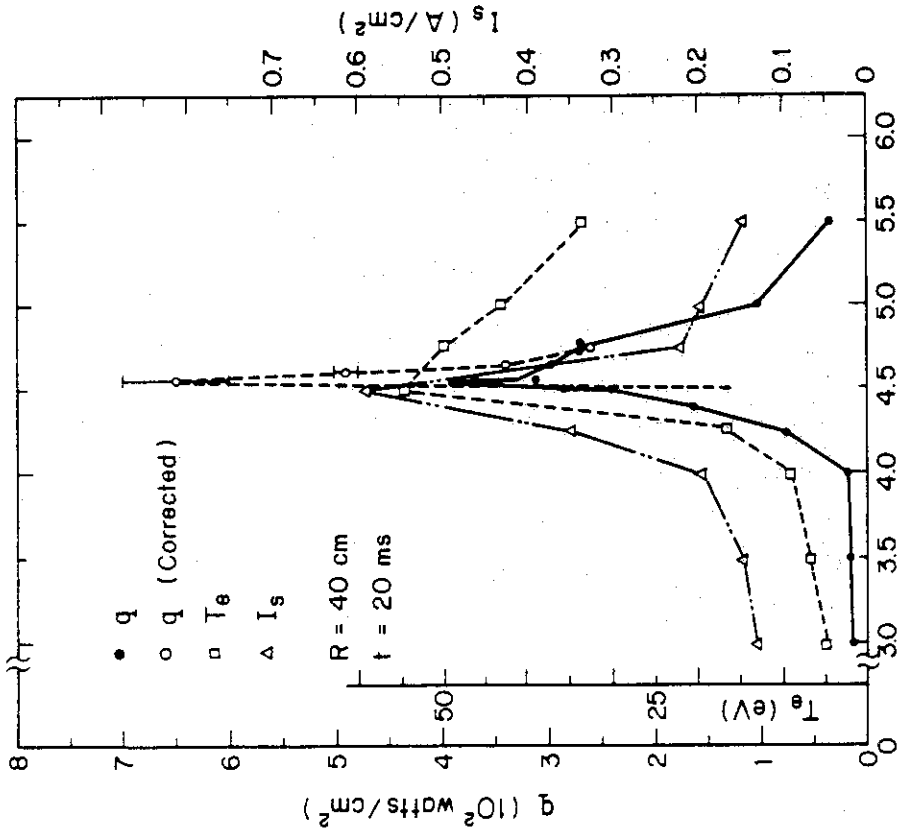

Fig. 5 Z-profiles of heat flux q, electron temperature T_e and ion saturation current density I_s on the electron side of the divertor. Heat fluxes near the peak position are corrected by the transverse-heat-cunduction equation.

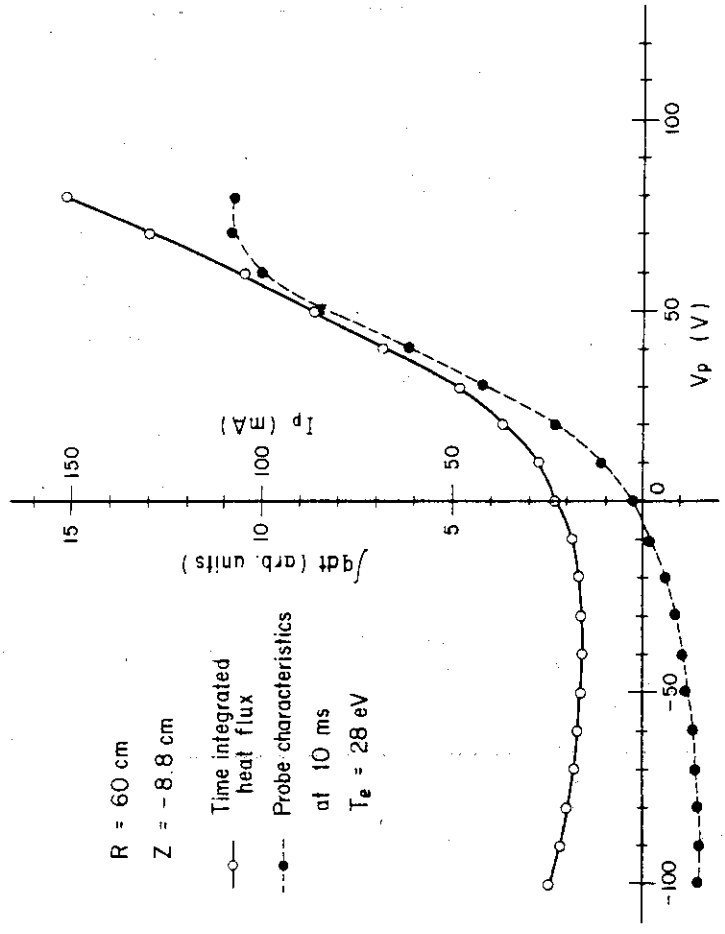

Fig. 8 Time-integrated heat flux during the whole discharge duration to a thermocouple as a function of bias voltage V_p of a thermocouple sheath, together with the probe characteristic at 10 ms, employing the sheath as an electrode.

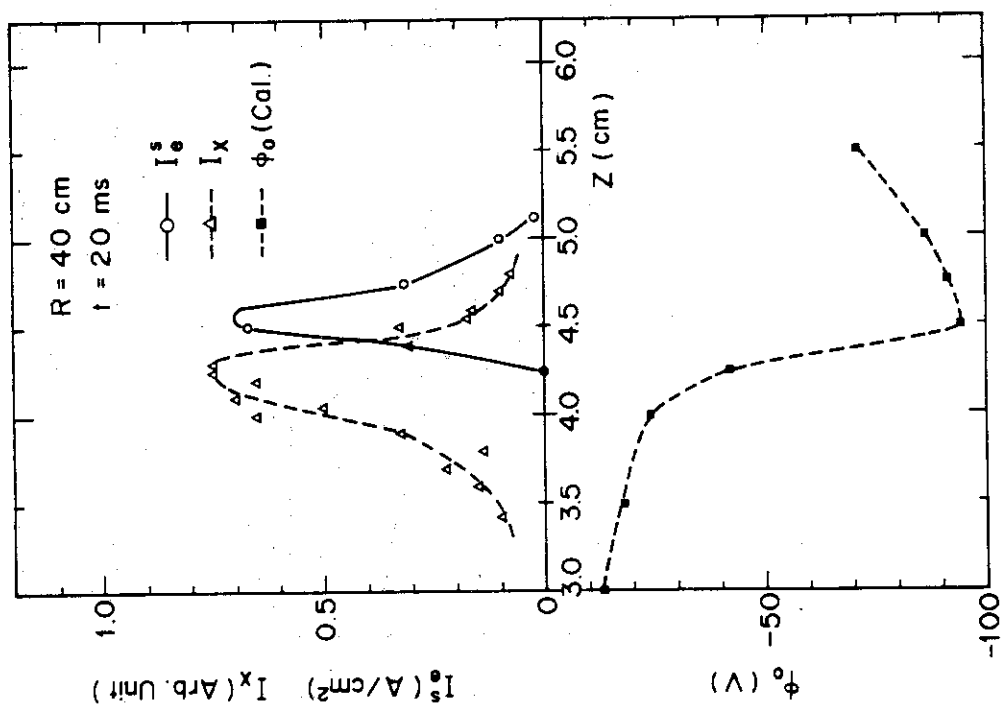

Fig. 7 Z-profiles of epithermal electron flux I_e^s, X-ray intensity I_x and calculated folating potential ϕ_o on the electron side of the divertor.

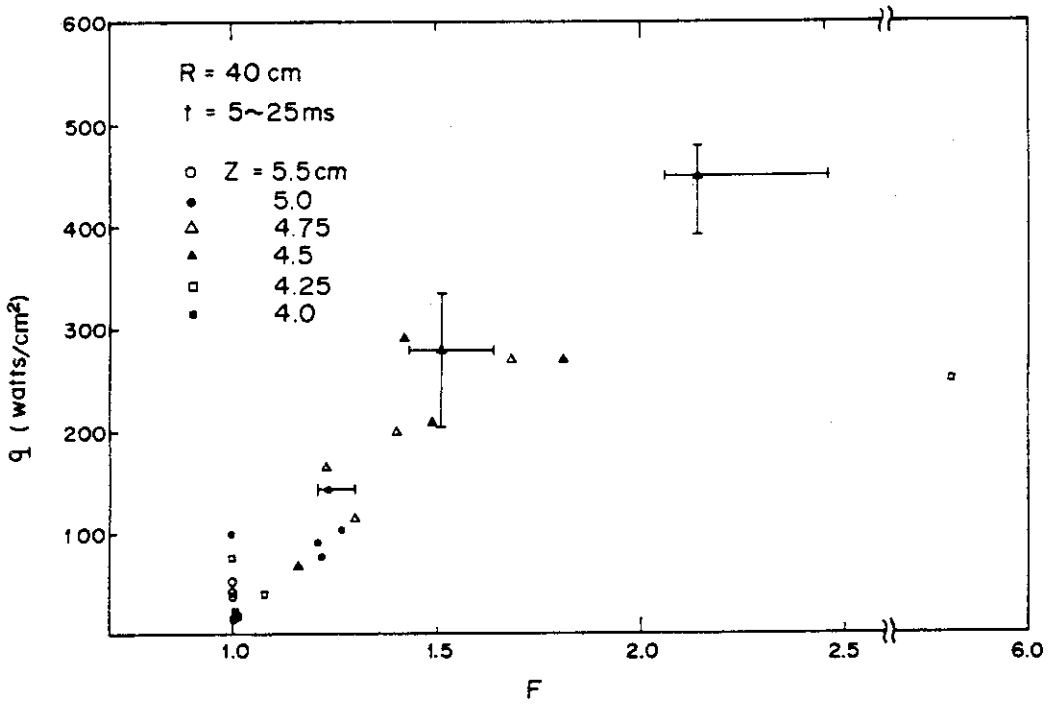

Fig. 9 Relationship between heat flux q and correction factor F for the two-component model.

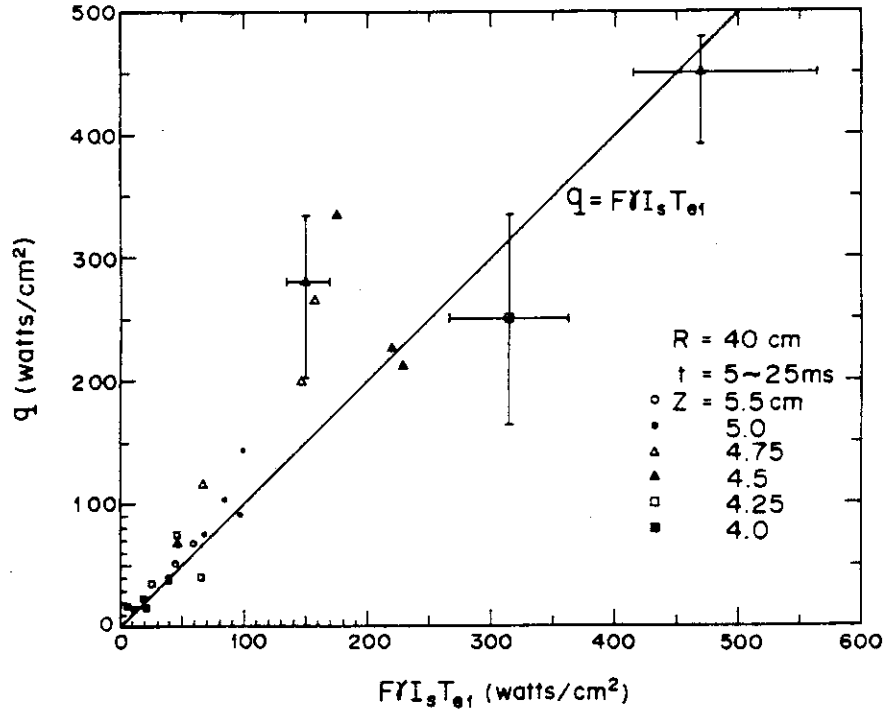

Fig.10 Relationship between heat flux q and $F\gamma I_s T_{e1}$ for the two-component model.

5. RADIATION LOSS AND POWER BALANCE IN AN OHMICALLY-HEATED TOKAMAK PLASMA

The radiation loss is measured quantitatively by a pyroelectric detector calibrated by heavily contaminated resistive discharges. The results are: (1) radiation loss power due to low-Z impurities does not play an important role; (2) radiation loss power due to the pseudo-continuum from high-Z impurities affects the power balance of the confined plasma; (3) the time dependence of energy loss channels is clarified in the gross power balance, a fact of which attests to the reliability of the radiation measurements carried out by the pyroelectric detector.

5.1 Introduction

Radiation losses significantly affect temperature, power balance and stability of tokamaks. In particular, high-Z-impurity effects (such as Mo, W, and Au, etc.) will become much more serious in future tokamaks because the plasma will easily be contaminated by high-Z-impurities [1] radiating a large amount of power [2].

In the TFR, radiation is measured spectroscopically and bolometrically, the former method showing radiation due to oxygen to be dominant and the latter one demonstrating correlation with the molybdenum signals; no agreement of these two methods has, however, been obtained [3]. The complexity of the spectrum due to heavy impurities seems to make it difficult to estimate the radiation loss. A Veco "Thinistor" and a pyroelectric detector are used to measure the radiative power in ATC [4] and ORMAK [5], respectively. However, radial profile or comparison with spectroscopy have not been obtained.

DIVA is a tokamak with an axisymmetric divertor, and spectroscopic and various probe measurements carried out at several places around the torus have shown that the detected flux (photons and ions) and the temperature do not depend on the detector position along the toroidal direction [6]. Divertor and toroidal symmetries facilitate attacking the problem of impurities and radiation losses.

In this chapter, we attempt: (1) to calibrate a pyroelectric detector and to evaluate the radiative power and its radial profile quantitatively, (2) to obtain a quantitative correlation between bolometric and spectroscopic measurements, and (3) to clarify the time dependence of

various loss channels in the DIVA energy balance.

The pyroelectric detector is calibrated by using resistive discharges (i.e. discharges with cleaning processes setting in early), and this calibrated value represents an uppermost value for the detector sensitivity. The total value and the radial profile of the radiation loss are obtained over a wide range in Ohmic-heating power.

Radiation loss due to low-Z impurities does not play an important role, and the pseudo-continuum in the range of 120-240 Å has a good correlation with the signal observed by the pyroelectric detector and dominates the radiation loss. In a discharge without divertor, the radiative power due to the pseudo-continuum increases by a factor of five.

The power balance study shows that radiative power, charge-exchange, and conduction and convection losses are 30 %, 10 % and 60 %, respectively, for 10 kG, and 23 %, 7 % and 70 % of Ohmic input power, respectively, for 20 kG with divertor operations.

Section 5.2 shows the experimental set-up, and Section 5.3 the calibration of the pyroelectric detector. The experimental results and the correlation between the results of measurements carried out with the pyroelectric detector and the spectroscopic measurement in the vacuum-ultraviolet region are shown in Section 5.4. Section 5.5 discusses the gross power balance, and conclusions are drawn in Section 5.6.

5.2 Experimental Set-up and Method

DIVA is a tokamak with an axisymmetric divertor, and the cross-sectional view of the device is shown in Fig. 1. The main plasma is surrounded by a copper shell which is divided into four sector pieces in the toroidal direction and is ion-plated with gold to reduce gas absorption. The shell has an opening towards the burial chamber which is made of stainless-steel. There are a divertor hoop and titanium evaporation sources in the burial chamber. A part of the shell, i.e. the movable shell, can be moved vertically to vary the width of the opening connecting the plasma with the divertor. The movable shell, titanium-alloy wires and copper rods supporting these wires are removed in the 20 kG experiment. The protection plates of gold act as a limiter for the discharge without divertor. A more detailed description of this device is found in Ref. [7].

In addition to conventional measurements, the diagnostics used are: a) the pyroelectric detector, which will be described in the next section; b) a grazing-incidence vacuum monochromator calibrated by a branching-ratio method (20-1300 Å) [8]; c) Langmuir probes, and an electrostatic multi-grid energy analyzer, which are used to measure scrape-off-plasma parameters such as plasma density, electron and ion temperatures, and particle flux to the divertor [9]; d) thermo-meter and/or thermo-couple probes which measure the heat flux to the divertor with a resolving time of 0.2 ms and 5 ms, respectively [10].

The total outflux to the shell from the main plasma is measured by biasing each four sector pieces negatively with respect to one another to collect the ion saturation current impinging on each surface [9].

5.3 Calibration of the Pyroelectric Detector

Time-resolved measurements of radiation including charge-exchange neutral loss flux have been carried out by a vertically scanning colimated pyroelectric detector. The detected flux (neutrals and photons) does not depend on the detector position in the toroidal direction. It is not clear how much the absorption coefficient of the pyroelectric detector refers to the vacuum ultraviolet region and how much to the charge-exchange fast neutrals. Thus, the surface of the pyroelectric element is covered with the same material as the first wall, i.e. gold, and the energy deposition by fast neutrals and photons on the element surface is expected to be the same as the flux impinging on the first wall.

One convenient methods is to use a tokamak plasma as a light source to calibrate the pyroelectric detector, but usually the radiative power is not clear. The radiative power can be estimated to be almost equal to the Ohmic input in heavily contaminated discharges.

A calibration of the pyroelectric detector has been performed in the course of discharge cleanings, in which the plasma is heavily contaminated, and it is expected that almost all of the Ohmic input energy is translated by radiation to the shell surface. Thus, we can estimate an upper limit of the radiative power, including neutral loss flux.

Figure 2 shows the relative radiation loss per unit length of the plasma column measured by a vertical scan of the collimated pyroelectric detector and the input power in the cource of the discharge cleanings. The open circles are obtained in the early phases of the discharge

cleanings. In these cases, toroidal symmetry is also established.

An example of plasma current, loop voltage and a signal from the pyroelectric detector at the center of the column is also shown in Fig. 2. The loop voltage V_L is 20-30 V and is well correlated with the radiative power. These open circles give the maximum of the radiative- to-input-power ratio. The black circles are obtained in the middle stage of the discharge cleaning, and I_P, V_L and the radiative power are also shown in Fig. 2. Many voltage disruptions have been observed and, in this case, the radiative- to-input-power ratio is smaller than in the case of resistive discharges.

The calibration of the pyroelectric detector was done with discharge cleaning pulses, which usually have low temperature and density and which may have spectral compositions from those of regular pulses. Thus, we have assumed the spectral response of the pyroelectric detector to be flat and the gold plating not to act as a filter. The calibration of the pyroelectric detector by the afore-mentioned method only is not always accurate. The consistency of these assumptions will be demonstrated in the course of a power balance study in Section 5.5.

5.4 Experimental Results

5.4.1 Characteristics of Discharges

There can be two types of discharge operations in DIVA: with and without divertor. The discharge with divertor is characterized by I_D/I_P = 1.2, where I_D and I_P are the divertor and the plasma current, respectively, and there is a separatrix in the shell. Therefore, a fraction of particles and heat flows to the burial chamber. For the operation without divertor, we have I_D/I_P = 0.46; in this case, the separatrix is outside the shell and there is no particle and heat flow to the burial chamber.

The electron temperature T_e as measured by laser scattering is about 180-250 eV at r = 3 cm, and the ion temperature T_i as measured by a charge-exchange spectrometer is 80-100 eV, in both cases at the center of the column.

The plasma radius is limited by the gold protection plates (i.e. a limiter) in the operation without divertor; and the radius of the current channel is 10 cm and is larger than that in the operation with divertor (8.5∿9 cm), in which the current channel is limited by a magnetic limiter. In both cases, the plasma currents are determined so as to have the same

safety factor at the limiter q_a.

Figure 3 shows a signal of the pyroelectric detector along different chords (dotted line) and the caculated radial profile of the power density (solid line), in discharges with and without divertor.

Both cases have almost the same T_e and T_i at the center of the column, and a total electron number of N_e. The loop voltage is, however, by factor of 2.5 smaller for discharges with a divertor than for those without one, and the radiation loss including neutral flux is also smaller by a factor of three. It should be noted that, for similar plasma parameters, the power throughput is by a factor of three smaller for discharges with divertor than for those without one.

This indicates that the energy confinement time, τ_E, is increased by a factor 2 or 3 for a discharge with divertor, which seems to be a result of the decrease in radiation loss. The radiation loss is not the dominant factor in the power balance, even for the case without divertor. The electron temperature profiles are, however, strongly affected by the radiation loss. The divertor increases the radius of the hot column by reducing the radiation loss and increases the energy confinement time because the internal energy of the plasma is concentrated in the hot column [13]. The energy confinement time is discussed in detail in Ref. [14].

5.4.2 Pseudo-continuum

Impurities observed with vacuum-ultraviolet spectroscopy are grouped into light elements (C, N, O) and heavy elements (Au, etc.). The spectroscopic intensity of the light elements can be reduced to half of its value by flushing titanium on the divertor chamber surface. On the other hand, the resistivity is not remarkably changed, when the amount of light element is reduced to one half. The density of light impurities is less than 1 % of the density of the electrons before titanium flushing, and the radiation loss due to light impurities is spectroscopically estimated to be 6 kW [11]. The reduction of radiation loss due to the reduction of light impurities by a factor of two is bolometrically estimated to amount to 2-3 kW. Thus, the radiation loss due to light impurities can be estimated to be 4-6 kW (20∿30 % of the radiative power measured by the pyroelectric detector) at 10-15 ms in the operation with divertor and no titanium flushing. Therefore, heavy elements dominate the radiation losses in DIVA experiments.

Figure 4 shows the power spectrum versus the wavelength in the range 120 Å - 240 Å, i.e. the pseudo-continuum, in the cases with and without divertor. The spectrograph at wavelength between 20 and 2000 Å shows that the radiative power from the plasma is concentrated in this range [12].

The signal from the pyroelectric detector is sensitive to this pseudo-continuum. Unfortunately, it is quite difficult to identify the origin of this pseudo-continuum. When the particle and heat fluxes to the burial chamber are intercepted by the gold-plated movable shell, the line radiation of AuII (1800.85, 1973.31 and 1783.22 Å) measured by a normal-incidence vacuum monochromator has increased, and, simultaneously, the intensity of the pseudo-continuum has also increased. This fact suggests that the pseudo-continuum is due to gold.

Figure 5 shows the correlation between the line-integrated radiative power measured by the pyroelectric detector (P_{py}) and that of the pseudo-continuum at the column center.

Open circles represent the case without divertor and black circles that with divertor; ⊖, ⊕ and ⊙ indicate the various conditions of the burial chamber, e.g. the case in which particles and heat flux to the burial chamber are intercepted by the movable shell. The details of these cases are described in Ref. [12]. The triangle designates the optimum condition, i.e. the case where the whole particle and heat flux to the burial chamber is intercepted by a molybdenum target [13], whose heat and sputtering characteristics are better than those of the materials used in DIVA.

There is a good correlation between the radiative power measured by the pyroelectric detector and the radiance due to the pseudo-continuum. The radiation loss due to heavy impurities in the optimum condition becomes comparable to the power loss due to charge-exchange fast neutrals.

The radiative power due to the pseudo-continuum is reduced by introducing the molybdenum target in the divertor, and, in this case, the other plasma parameters are not remarkably changed. Figure 6 shows a correlation between the decrease of P_{py} and that of the radiative power due to the pseudo-continuum. There is a linear correlation, and, from the slope, we can evaluate the radiative power due to the pseudo-continuum. The value calibrated by this method is by a factor of three smaller than that calibrated by a branching-ratio method [8] and is within the accuracy of the calibration.

Figure 7 shows the radiation loss due to the pseudo-continuum

calibrated by this method, in the cases with an without divertor operation. The radiation loss due to the pseudo-continuum is 8.5 kW for the discharge with divertor and 39 kW for that without one at 15 ms. We can estimate the gold-ion density and an effective ionic charge Z_{eff} by using the results of Ref. [15], under the following assumptions: (i) most of the energy radiated by gold is in the detected pseudo-continuum; (ii) corona equilibrium is attained in the central plasma; (iii) the profile of the pseudo-continuum is the same as that measured with the pyroelectric detector shown in Fig. 3; (iv) the contribution from the light impurity to Z_{eff} is neglected because the density of the light impurity is about 1 % of the electron density. The estimated gold-ion density at the center of the column is 0.3 % of the electron density for the discharge with divertor and 1.5 % for that without one, at 15 ms. Then, the resulting Z_{eff} is about 2 and 6 for the discharges with and without divertor, respectively. On the otherhand, the resistivity anomaly calculated on the assumption $q(0) = 1$ is 2-2.5 and 6-8 for discharges with and without divertor, respectively, and is consistent with Z_{eff} determined by the pseudo-continuum.

In conclusion, we can state that the divertor reduces the plasma-wall interaction and, consequently, reduces the radiation loss due to heavy impurities.

5.5 Power Balance with Divertor on

In this section, gross properties of the energy balance will be investigated. The determination of the gross energy loss channels gives comfirms the calibration of the pyroelectric detector and the results described in the previous section.

5.5.1 Power Balance in the 10-kG Experiment

The discharge parameters are shown in Fig. 8; the toroidal magnetic field is 10 kG and $I_D/I_P = 1.2$. The electron temperature at $r = 3$ cm and the ion temperature at the centre of the column at 10 ms are 180 ± 50 eV and 100 ± 20 eV, respectively.

(1) Conduction and convection

An outflux from the plasma can be obtained by ion saturation current falling on each of the shell (or vacuum chamber) surfaces which are

biased negatively with respect to one another.

Figure 9 shows the particle flux to the shell, protection plates, movable shell, and burial chamber.

Heat flows to the shell and the protection plates are calculated by $Q_s = \gamma I_s T_e$ [10], where I_s is the ion saturation current to the shell (or protection plates) and γ is termed a heat transmission rate; experimentally, $\gamma = 5$ is obtained near the shell surface. From this equation, and using the ion saturation current impinging on the shell, we can estimate the heat flow to the shell and the protection plates. In a present experiment, the electron temperature on the surface of the shell measured by Langmuir probes is 15 - 20 eV.

The heat flow to the divertor is measured directly by a thermo-meter (and/or a thermo-couple probe). In the divertor region, the heat transmission rate is higher than the value predicted by a simple sheath model (i.e. $\gamma = 7.8$) for hydrogen plasma of $T_e = T_i$, because of the existence of epithermal electrons and $\gamma = 8$-20 [10]. The heat flows due to conduction and convection are 25 kW, 6 kW and 3 kW to the shell and and protection plates, the burial chamber, and the movable shell, respectively.

(2) Radiation loss and charge-exchange fast neutrals

The energy loss from the main plasma through the radiation and fast neutrals measured by the pyroelectric detector is about 40 % of the Ohmic input, and 22-23 kW at 10 ms. The radiation loss due to the pseudo-continuum measured by the vacuum-ultraviolet spectroscope calibrated in the previous section amounts to about half of the loss measured by the pyroelectric detector.

The energy loss due to charge-exchange fast neutrals is measured by a charge-exchange spectrometer; this value is checked by a two-dimensional Monte-Carlo code. The experimental and calculated values are consistent, 6-8 kW at 10 ms.

The composition of the loss measured by the pyroelectric detector is shown in Fig. 10. The remaining part of the loss may be due to light impurities. The value is 4-6 kW at 10 ms and 2-4 kW at 15 ms, and these values are consistent with the value estimated by spectroscopic and bolometric measurements as described in Section 5.4, paragraph 2.

The time variations of the energy losses in each channel are shown in Fig. 11. The sum of these energy losses coincides well with the Ohmic input power.

The energy balance study at 10 kG shows that the radiative power, the charge-exchange loss, and the conduction and convection losses are about 30 %, 10 %, and 60 % of Ohmic input power, respectively. This imparts consistency to the independent measurements of the energy loss channels, and makes a measurement of the radiation loss by the pyroelectric detector reliable.

However, the result of the energy balance study for 10-kG experiment has still an uncertainty insofar as the conduction and convection losses to the shell have been obtained by a calculation using the experimental values of I_s, T_e, and the heat transmission rate γ, and is the largest energy loss channel which occupies 40 % of the Ohmic input power. The heat transmission rate γ includes an error of a factor of 1.5 and T_e amounts to ±20 %, and the resulting energy loss to the shell may include an error of a factor of 1.5-2.0. In the next sub-section, we shall check the relative accuracy of the measurements in experimental conditions in which conduction and convection losses to the shell consistitute a smaller part of the Ohmic input.

5.5.2 Power Balance in the 20-kG Experiment

In this section, we describe preliminary results of an energy balance study in a 20-kG DIVA discharge. Here, movable shell, titanium wires and their supports shown by dotted curves in Fig. 1 have been removed; the rest of the configuration is the same as in the 10-kG experiment.

The plasma parameters are I_p = 40 kA, T_{eo} = 0.7 keV, $n_{eo} = 0.8 \times 10^{14}$ cm^{-3} and the Ohmic input power P_{in} = 140 kW. The ion temperature T_i agrees with the Artsimovich scaling law and is 270 eV. The pseudo-continuum is observed in the range of 45-250 Å in the present experiment, and low-Z-impurities are more influential than in the 10-kG experiment [13].

The radiative power including charge-exchange losses measured by the pyroelectric detector is 41 kW. The charge-exchange loss calculated by the two-dimensional Monte-Calro code amounts to 10 kW. The heat flux to the divertor measured with the thermo-couple probe is 80 kW and occupies about 55 % of the Ohmic input power.

The heat flux to the shell and the protection plates is calcualted from I_s, T_e and γ. The particle flux to the shell and the protection plates is 180 A, and the electron temperature near the shell is 20-25 eV.

Assuming γ = 5, the calculated heat flux to the shell is 18-23 kW and occupies only 15 % of the Ohmic input power. The sum of these losses is 140-145 kW, and is in good agreement with the Ohmic input power. The results are summarized in Table I.

This result also imparts consistency to the independent measurements of the energy loss channels. The uncertainty described in the 20-kG experiments becomes small because the calculated heat flux to the shell represents only 15 % of the Ohmic input power. The Ohmic input, conduction and convection losses to the shell and the burial chamber are 140, 18-23 and 80 kW, respectively, and the remaining part is considered to be lost by radiation and charge-exchange neutrals and is 37-42 kW. This value agrees well with the value (41 kW) measured by the pyroelectric detector. Thus, the calibration of the pyroelectric detector described in Section 5.3 gives good accuracy.

5.6 Summary

The radiation loss is quantitatively measured in discharges with and without divertor, and the experimental results can be summarized as follows:

(1) The pyroelectric detector, which is sensitive to radiation and neutral loss flux, is calibrated by heavily contaminated resistive discharges.

(2) Radiation loss due to low-Z-impurities does not play an important role, and that due to high-Z-impurities has a great effect and is responsible for the radiation loss from the main plasma.

(3) A pseudo-continuum observed in the range of 120-240 Å is well correlated with the radiative power measured by the pyroelectric detector. In optimum operation with divertor, the radiation loss due to heavy impurities becomes comparable with the power loss due to charge-exchange hot neutrals; on the other hand, in the operation without divertor, the radiative power due to the pseudo-continuum increases by a factor of five.

(4) The time dependences of the energy loss channels were clarified in the gross power balance. The radiative power, charge-exchange loss, and conduction and convection losses are 30 %, 10 %, and 60 % of the Ohmic input power, respectively, in the 10 kG operation, and 23 %, 7 %, and 70 % of the Ohmic input power, respectively, in the 20-kG operation with divertor.

(5) The assumption of flat spectral response of the pyroelectric detector is justified by the consistency prevailing in the power balance study, and the measurement of radiation loss by the pyroelectric detector and of other loss channels is reliable.

References

[1] SHIMOMURA, Y., Nucl. Fusion 17 (1977) 626.

[2] JENSEN, R.V., POST, D.E., GRASBERGER, W.H., TARTER, C.B., LOKKE, W.A., Nucl. Fusion 17 (1977) 1187.

[3] EQUIPE TFR, in Plasma Physics and Controlled Nuclear Fusion Research (Proc. 6th Int. Conf., Berchtesgaden, 1976) Vol.1, IAEA, Vienna (1977) 35.

[4] HSUAN, H., BOL, K., ELLIS, R.A., Nucl. Fusion 15 (1975) 657.

[5] BUSH, C.E., EDMONDS, P.H., ENGLAND, A.C., LYON, J.F., Bull. Am. Phys. Soc. 20 (1975) 1299.

[6] SHIMOMURA, Y., NAGASHIMA, T., KITSUNEZAKI, A., MAEDA, H., OHTSUKA, H., et al., The First Results on JFT-2a, Japan Atomic Energy Research Institute Report JAERI-M 6102 (1975).

[7] SHIMOMURA, Y., MAEDA, H., OHTSUKA, H., KITSUNEZAKI, A., NAGASHIMA, T., et al., Phys. Fluids 19 (1976) 1635.

[8] SHIHO, M., ODAJIMA, K., SUGIE, H., MAEDA, H., KASAI, S., et al., Spectroscopic and Bolometric Measurement of Radiation Loss in DIVA, Japan Atomic Energy Research Institute Report JAERI-M 7397 (1977).

[9] KIMURA, H., NAGAMI, M., YAMAMOTO, S., UEDA, N., OHTSUKA, H., MAEDA, H., SHIMOMURA, Y., Diagnostics of a Scrape-off Layer Plasma, Japan Atomic Energy Research Institute Report JAERI-M 6971 (1977).

[10] KIMURA, H., MAEDA, H., UEDA, N., SEKI, M., KAWAMURA, H., YAMAMOTO, S., Nucl. Fusion 18 (1978) 1195 [Chapter 4 in this thesis].

[11] NAGAMI, M., SHIMOMURA, Y., MAEDA. H., OHTSUKA, H., SHIHO, M., et al., Nucl. Fusion 18 (1978) 529.

[12] MAEDA, H., OHTSUKA, H., SHIMOMURA, Y., YAMAMOTO, S., NAGAMI, M., et al., in Plasma-Wall Interaction (Proc. 6th Int. Symp. Jülich, 1976), Pergamon Press, Oxford (1977) 537.

[13] YAMAMOTO, S., MAEDA, H., SHIMOMURA, Y., ODAJIMA, K., NAGAMI, M., et al., in Controlled Fusion and Plasma Physics (Proc. 8th Europ. Conf. Prague, 1977) Vol.1 (1977) 33.

[14] DIVA GROUP, Nucl. Fusion 18 (1978) 1619.

[15] POST, D.E., JENSEN, R.V., TARTER, C.B., GRASBERGER, W.H., LOKKE, W.A., Steady-State Radiative Cooling Rates for Low-Density, High-Temperature Plasmas, Princeton Plasma Physics Laboratory Report PPPL-1352 (1977).

Table 1 Particle and heat flow in 20-kG experiment with divertor operation

Particle flux (A)		Heat flux (kW)			
Divertor	Shell and limiter	Divertor	Shell and limiter	Radiation	Charge-exchange
80 (31 %)	180 (69 %)	80 (57 %)	18-23 (13 %)	31 (22 %)	10 (8 %)

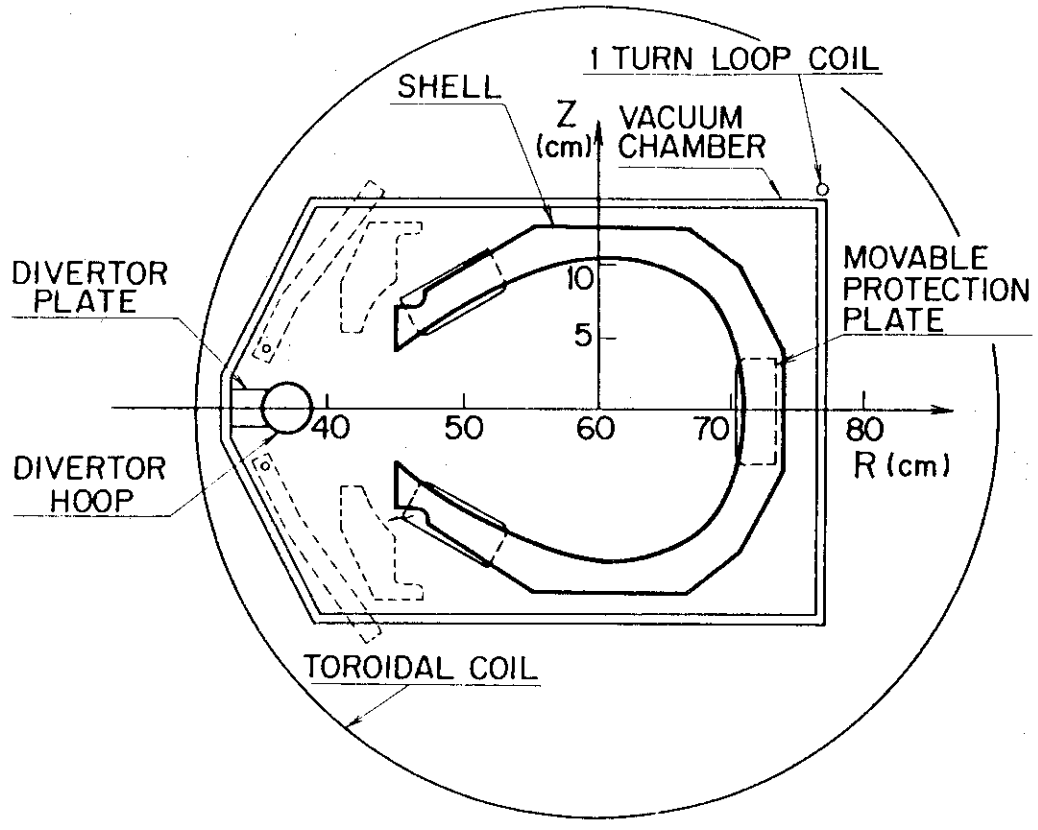

Fig. 1 Cross-sectional view of DIVA. The movable shell, the titanium-alloy wires and the copper rods supporting the titanium-alloy wires which are indicated by the dotted lines are removed in the 20-kG experiment.

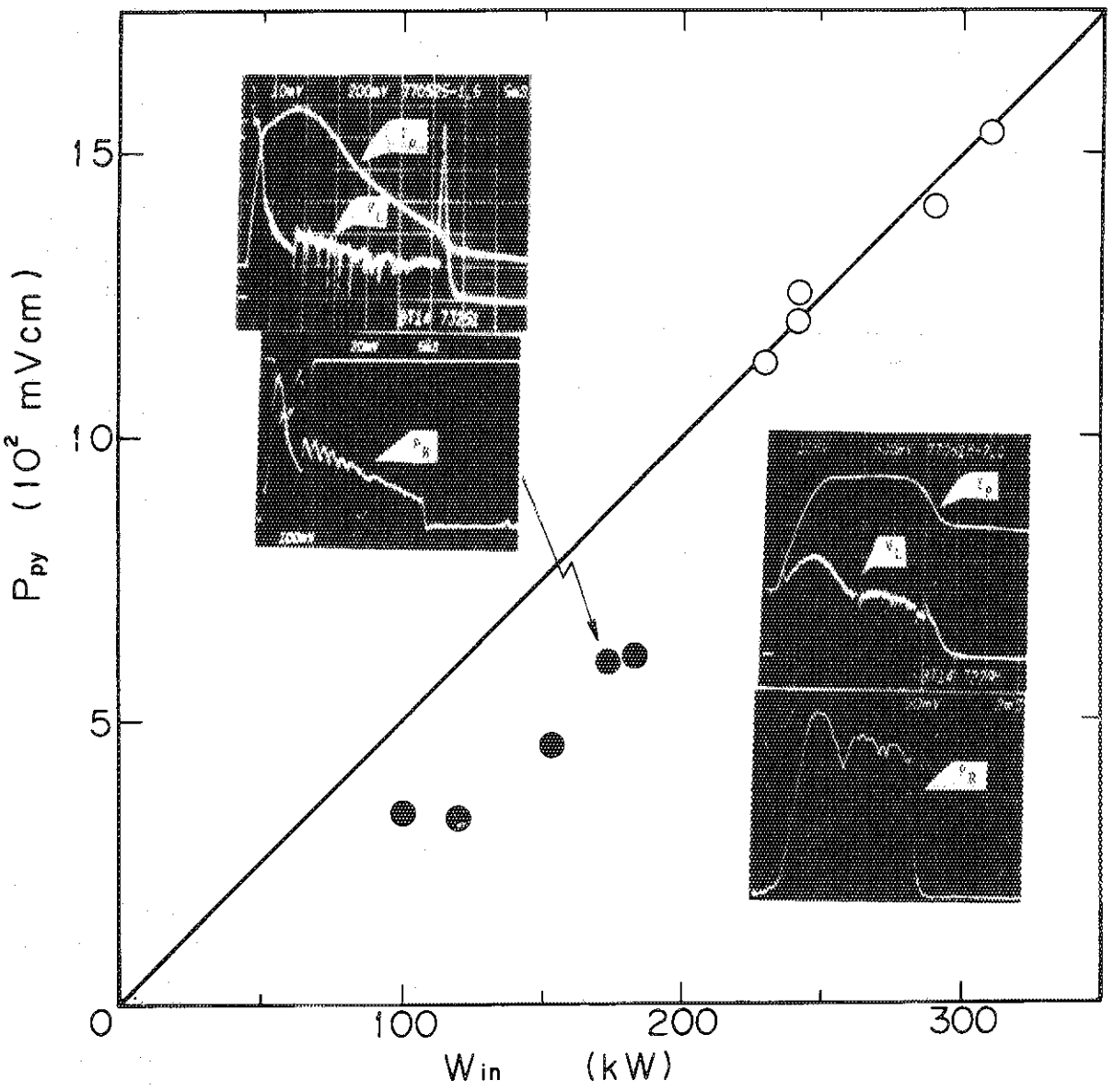

Fig. 2 P_{py}: Relative radiation loss per unit length of plasma column measured by a vertical scan of the collimated pyroelectric detector; W_{in}: Ohmic input power in the course of discharge cleanings. Plasma current, loop voltage and signals from pyroelectric detectors are also shown in this figure. The solid line indicates the calibrated value which is obtained by assuming that the entire Ohmic input energy is transported to the shell surface by radiation.

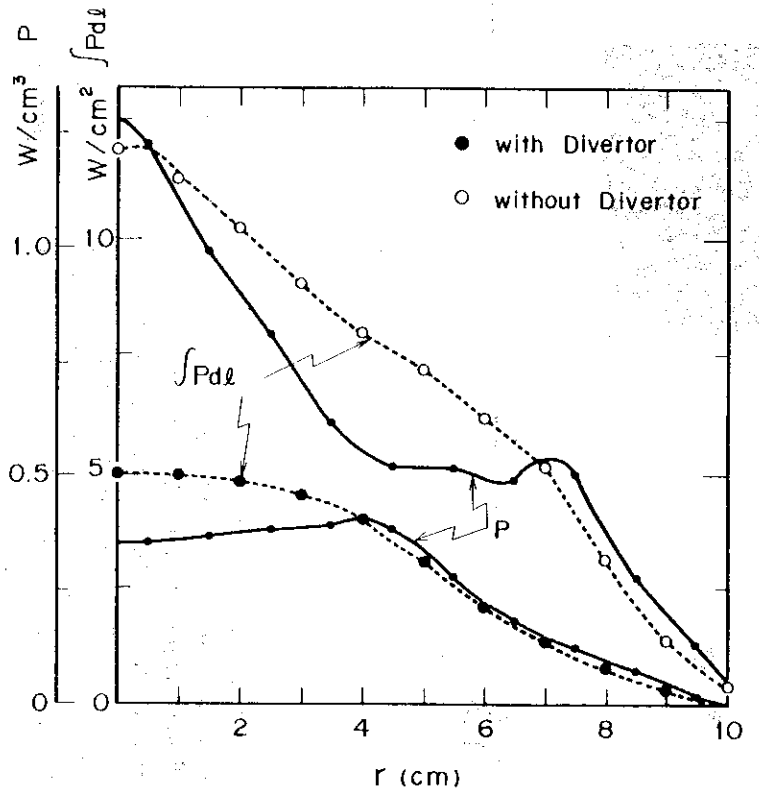

Fig. 3 Radial profiles of the power lost by radiation and charge-exchange neutral particles with and without divertor. Broken lines: integrated along the line of sight, solid lines: power lost per unit volume.

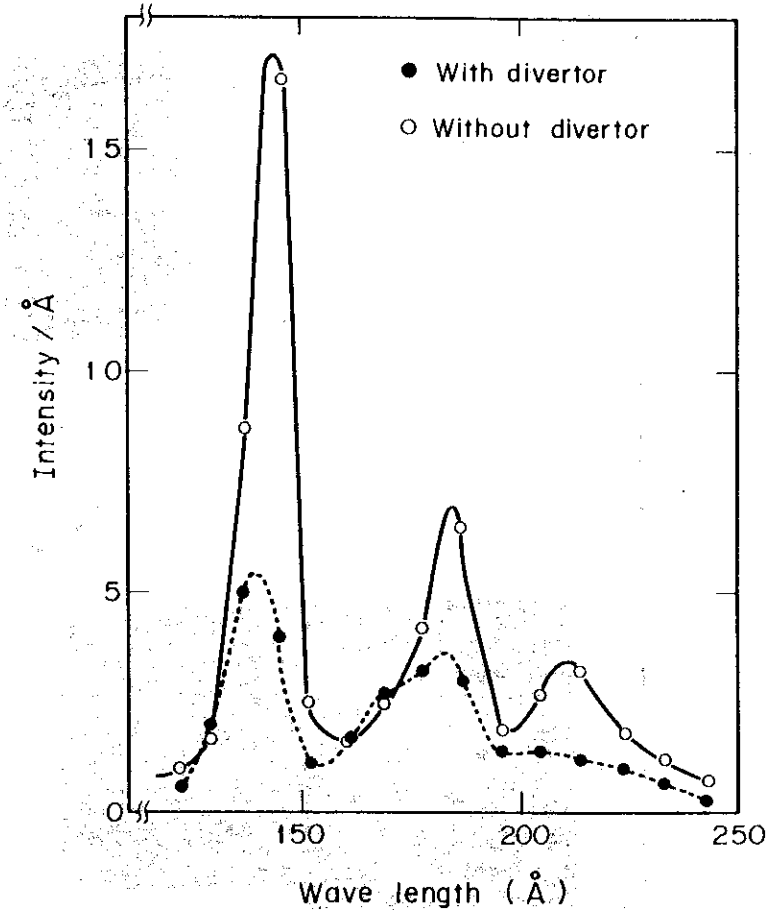

Fig. 4 Power sepctrum versus wavelength in the range 120-240 Å at 10 ms, i.e. pseudo-continuum, with (broken line) and without (solid line) divertor.

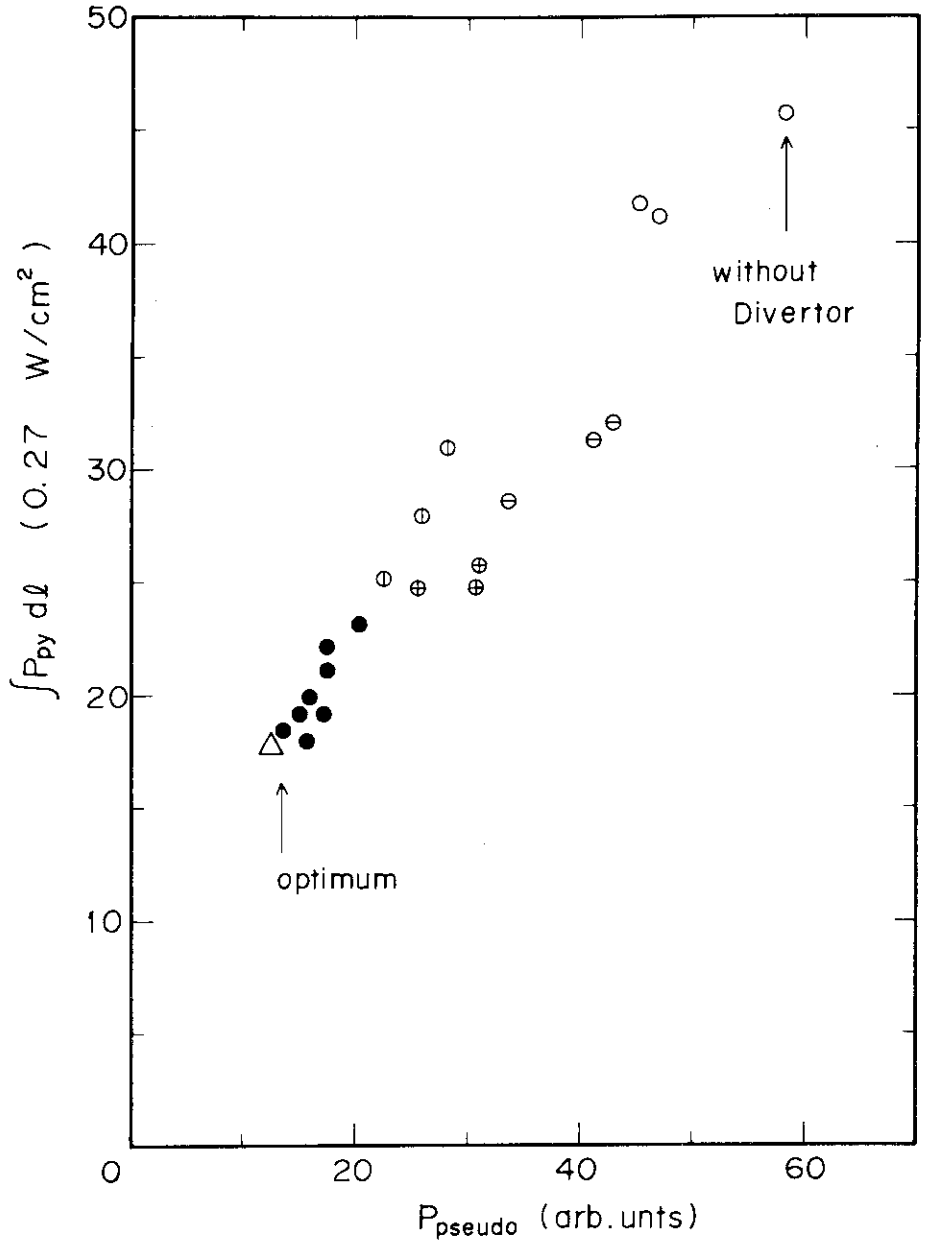

Fig. 5 Correlation between radiative power measured by the pyroelectric detector and that of the pseudo-continuum. Closed and open circles represent cases with and without divertor; the triangle refers to the optimum condition. Various conditions of the burial chamber (cases B, C, D in Ref. [12]) are shown by ⊕ , ⊕ and ⊖ , respectively.

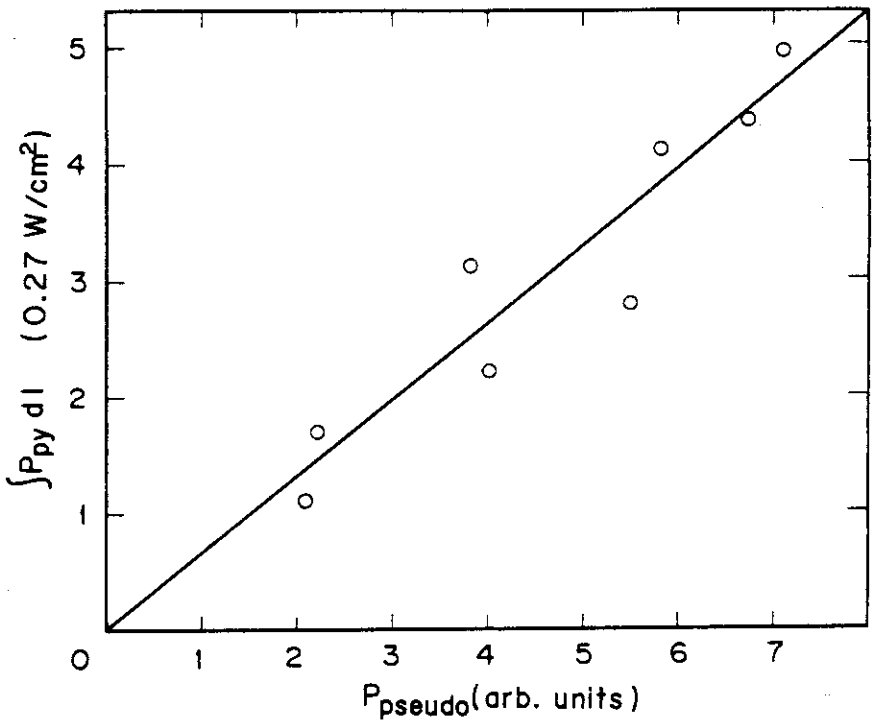

Fig. 6 Correlation between decrement of P_{py} and that of radiative power due to the pseudo-continuum, by introducing the molybdenum target into the burial chamber.

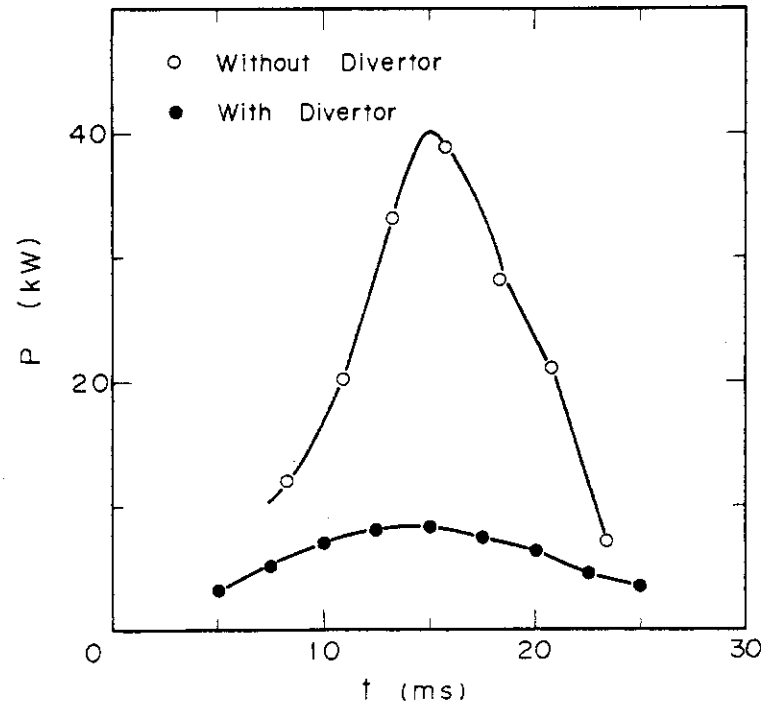

Fig. 7 Radiative loss due to the psudo-continuum calibrated by Fig. 6, in cases of optimized and divertorless operations.

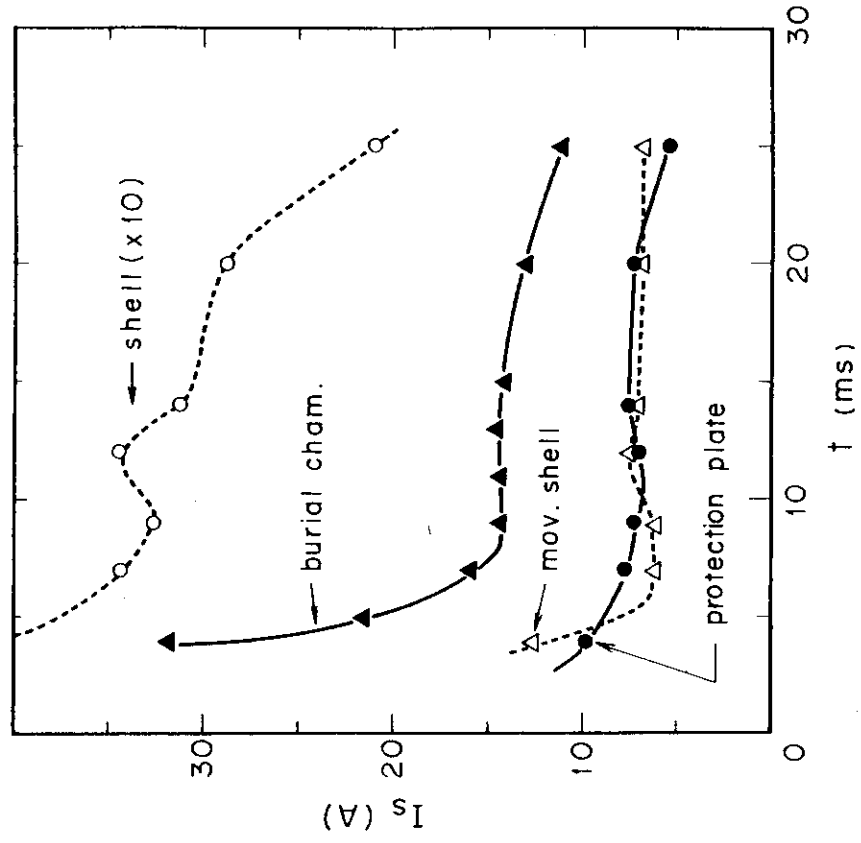

Fig. 9 Particle fluxes to shell, protection plates, movable shell and burial chamber.

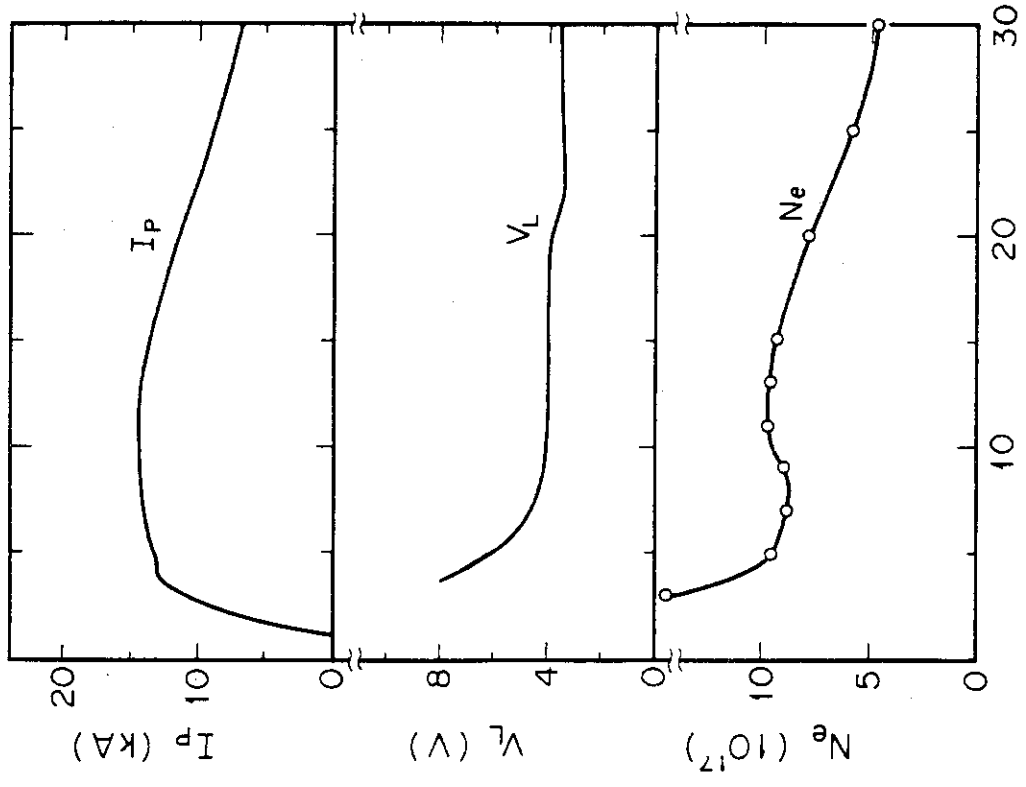

Fig. 8 Discharge with divertor in 10-kG experiment studied in this section; N_e is the total electron number.

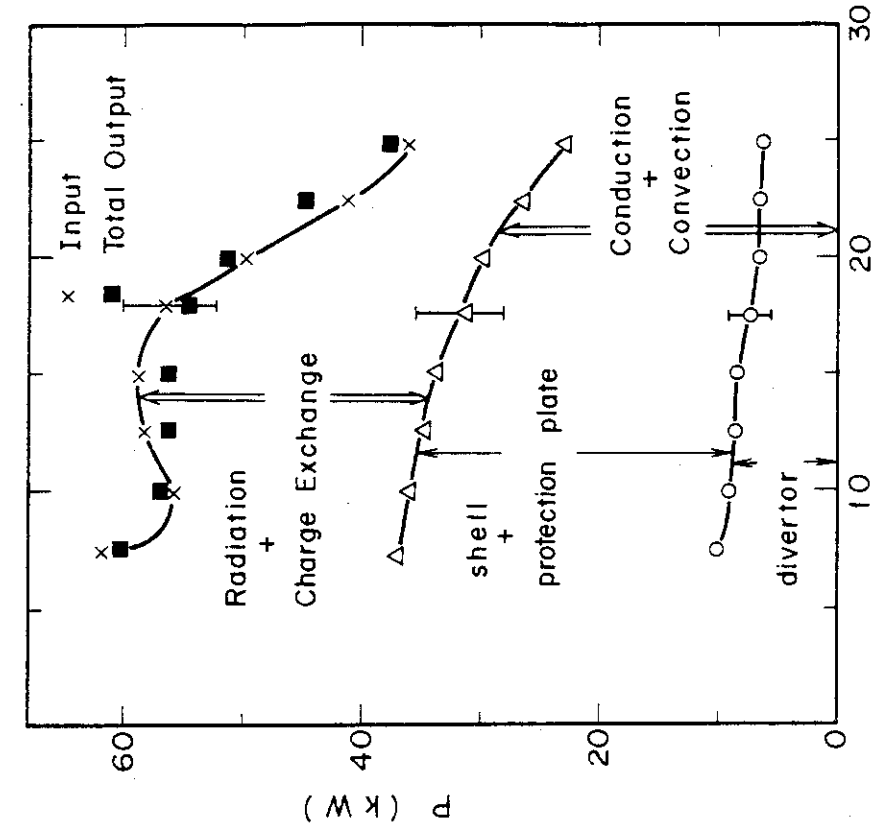

Fig. 11 Time variations of energy losses in each channel. The sum of all energy losses agrees well with the Ohmic input power.

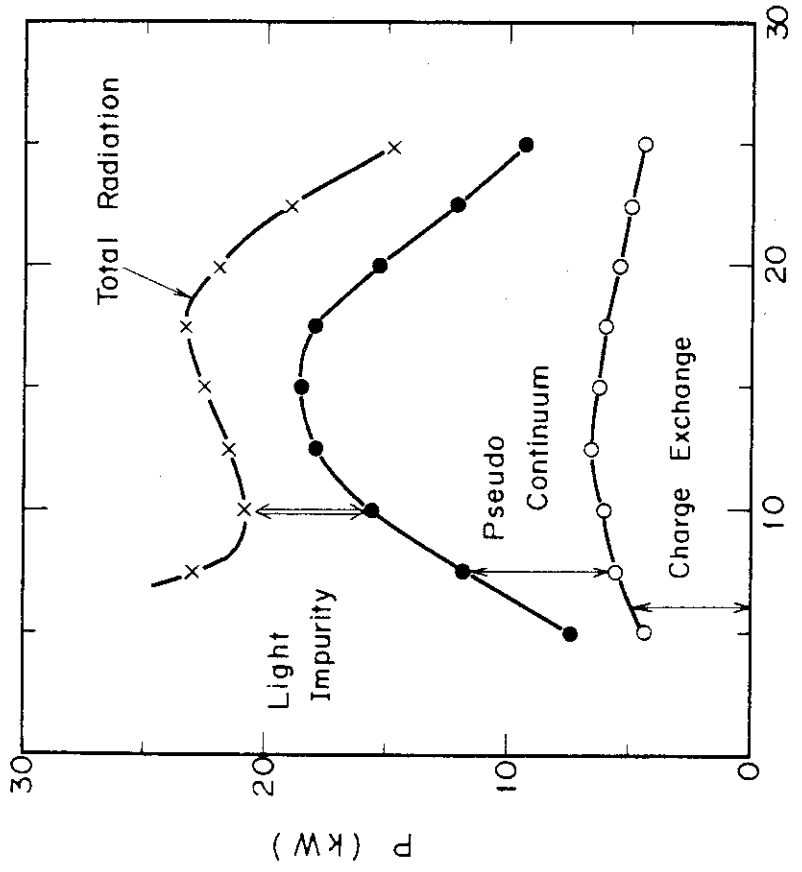

Fig.10 Composition of radiation loss measured by pyroelectric detector. The radiation loss due to the pseudo-continuum and the charge-exchange loss are determined; the remaining part of the loss might be due to light impurities.

6. POWER BALANCE IN AN ICRF-HEATED TOKAMAK PLASMA

6.1 Parameter Survey for the Optimum Ion Heating

ICRF heating of impurity-free tokamak plasmas is studied in DIVA. The frequency is fixed at 25 MHz, which is a second-harmonic cyclotron frequency of deuteron with a toroidal magnetic field of 16.4 kG. The toroidal field B_T and the ratio of proton-to-deuteron density ε_p are varied over ranges of $12 \leq B_T \leq 19$ kG and $2 \leq \varepsilon_p \leq 40$ %, respectively. The most favourable ion heating is obtained at $B_T = 18$ kG and $\varepsilon_p = 5 \sim 10$ %. Ion temperature increases from 200 to 300 eV were measured by charge-exchange neutral analysis and also by spectroscopy, where 100 kW RF net power were applied. The results are consistent with mode-conversion theory.

6.1.1 Introduction

This chapter describes high-frequency wave heating in the ion cyclotron range of frequency (ICRF) in the DIVA tokamak [1], using a second-harmonic cyclotron frequency of deuterium for a $D^+ + H^+$ discharge, where the latter is a minority component. ICRF heating has been intensively investigated in several tokamaks, i.e. early experiments in TO-1[2], TM-1-Vch[3], ST[4], and recent experiments in TFR[5], TM-1-VCh[6], T-4[7], ATC[8], etc. Those experiments were mainly performed for a deuterium plasma with a minority proton component, using a second-harmonic cyclotron frequency of deuterium. Wave-damping mechanisms have been also investigated in theory [9-11]. In TFR, it was shown that the variation of the wave amplitude versus major radius location of a harmonic cyclotron resonance layer of deuteron in a plasma cross-section was asymmetric with respect to the plasma center [5]. This asymmetry was well explained by the theory of mode conversion of the magnetosonic wave in the two-ion hybrid resonance layer [9, 11]. In addition, it was reported, though preliminarily, that the heating efficiency depended on the amount of the proton component, i.e. the ion temperature increase ΔT_i associated with the RF pulse was reduced to 50 % when the amount of H^+ was increased from 8 to 20 %, which again agreed with mode-conversion theory [12].

Thus, it is generally recognized that the heating mechanism of ICRF heating using a second-harmonic cyclotron frequency of deuterium for a $D^+ + H^+$ discharge is due to the mode conversion of the magnetosonic wave

in the two-ion hybrid resonance layer. However, details of the heating mechanism are not yet known because of a lack of reliable information on the ratio of proton to deuteron density during the RF pulse as well as on impurity effects. In the RF heating experiment, it is indispensable to keep impurity influxes as small as possible when the RF pulse is applied, in order to exclude the possibility of plasma heating due to impurities. Assuming $Z_{eff} = 4$ and oxygen impurities, more than 10 % of oxygen are present in a $D^+ + H^+$ plasma. In this situation, the effects of O^{8+} and O^{7+} must be taken into account. In addition, if the first wall is not well conditioned, the electron density and the amount of impurity influxes increase on applying the RF pulse. Then, ΔT_i associated with the RF pulse is partly due to the increase of Joule input with the increase of impurity influxes. The first wall of DIVA was thoroughly flushed by titanium. Extremely pure plasma was obtained, i.e. $Z_{eff} \approx 1$. The radiation loss was less than 10 kW for the Joule input of 85 kW. The one turn loop voltage V_L and the electron density were not affected in the experiment supplying an RF net energy of 1 kJ. No limit has been found for the RF net energy, as yet.

We have examined the dependence of the charge-exchange neutral energy spectrum on the toroidal field B_T and the ratio of proton to deuteron density ε_p over the ranges of $12 \leq B_T \leq 19$ kG and $2 \leq \varepsilon_p \leq 40$ %, respectively. ε_p was measured spectroscopically during the RF pulse. The most appropriate conditions of B_T and ε_p were found in which the maximum bulk ion heating occurred, no high-energy tail was present, and no adverse effect on the plasma confinement was observed.

6.1.2 Experimental Set-up

The generator was operated at 25 MHz which is a cyclotron frequency for hydrogen, ω_{CH}, or the second-harmonic cyclotron frequency for deuterium $2\omega_{CD}$ at 16.4 kG. The RF power can be up to 200 kW. Figure 1 shows a cross-sectional view of DIVA, together with a launching structure (antenna), a matching network and a transmission line. The launching structure was made of a half-turn copper strip, 2×0.3 cm^2 in cross-section, 10.4 cm in radius, and of a ceramic cover, 3.5×1.5 cm^2 in cross-section, 10 cm in inner radius. The launching structure was placed in the shell gap and protected by a pair of molybdenum guard limiters (not shown in Fig. 1), which prevent the ceramic cover from direct contact with the plasma. No Faraday shield was used for the present experiment.

The RF power was transmitted through a co-axial cable (RG-19U) from the generator to a two-stub matching network. The RF power was monitored by a directional coupler in front of the matching network. The coil current was measured by a current probe placed near the midpoint of the antenna. The end of the antenna was terminated to the vacuum vessel as is shown by the dotted line in Fig. 1. As the antenna length is much shorter than a wavelength corresponding to 25 MHz in free space, the coil current measured at the mid-point of the antenna is almost a peak value.

The antenna loading impedance R_s can be calculated from $R_s = \frac{P_f - P_b}{I_c^2}$ (Ω), where P_f, P_b and I_c are incident and reflected powers and the coil current, respectively.

The perpendicular ion temperatures were measured with a 10-ch charge-exchange neutral-particle energy analyser and a Czerny-Terner mounting vacuum monochromator. Both were placed at almost diametrically opposite ports of the antanna. The charge-exchange analyser is not capable of discriminating mass differences, and its signal contains contributions both from deuterium and hydrogen. Ion temperature profiles can be obtained from the Doppler broadening of impurity lines by scanning the monochromator [13]. Parallel ion temperatures were not measured for the present experiment.

The electron temperature and density were measured by laser scattering and by a 2-mm microwave interferometer, respectively. In the scrape-off layer, an electrostatic multigrid energy analyzer [14] and a Katsumata (ion-sensitive) probe [15] were used to measure the parallel and perpendicular ion temperatures, respectively.

6.1.3 Discharge Conditions

The experiment was performed under the following discharge conditions: The toroidal magnetic field B_T was varied from 12 to 19 kG. The ratio of the divertor hoop current to the plasma current was 1.2, where the latter was 32.5 kA with a flat-top in the case of B_T = 18 kG. Deuterium gas was admitted by two fast-acting valves and a programmable d.c. gas feeder.

The ratio of proton to deuteron density ε_p was measured during the discharge by the monochromator, which was varied over a range of 2 $\sim$ 40 % by adjusting the amount of additional hydrogen gas.

The basic plasma parameters in the case of B_T = 18 kG:

Central electron temperature	$T_{eo} \sim 330$ eV
Central ion temperature	$T_{io} \sim 200$ eV
Averaged electron density	$\bar{n}_e \sim 4 \times 10^{13}$ cm^{-3}
One-turn loop voltage	$V_L = 2.5$ V
Plasma current	$I_p = 32.5$ kA
Effective charge number	$Z_{eff} \simeq 1$
Major radius	$R = 60$ cm
Antenna (limiter) radius	$a_A = 10$ cm

6.1.4 Experimental Results

The RF power was applied for 3-8 ms. The maximum RF net power was 140 kW, limited by breakdown at the antenna. Although breakdown took place, the RF power could be raised gradually from a low level to the maximum power as before. The one-turn loop voltage did not change even with the application of maximum RF power. The change in the electron density was also within the shot-to-shot reproducibility of the base plasma, i.e. less than 10 %. Typical time evolutions of the perpendicular ion temperature $T_{i\perp}$, the electron line density $\overline{n_e \ell}$, the plasma current I_p, the one-turn loop voltage V_L, and the spectral line intensity OVII (1623 Å) are shown in Fig. 2. Although the OVII radiation increased by 30-40 %, the impurity level was very low in itself ($Z_{eff} \approx 1$). The electron line density changed only to a negligible extent when RF power was applied.

6.1.4.1 RF measurement

Measurement with the directional coupler and the current probe showed that the plasma loading impedance R_s was 6-7 Ω. This value changed only little over the ranges of B_T and ε_p in the present experiment. The same measurement, in the absence of plasma, gives a circuit loss R_c of 1 Ω. Then, a coupling efficiency was about 0.85. The RF net power, P_{Net}, is defined as

$$P_{Net} = \frac{R_s - R_c}{R_s} (P_f - P_b)$$

Figure 3 shows typical signals from the directional coupler indicating square roots of incident and reflected RF powers, the current probe and a magnetic probe located diametrically opposite to the position of the antenna, in the case of $B_T = 18$ kG and $\varepsilon_p = 5 \sim 10$ %. The signal of the

magnetic probe shows that there is no resonant peak since the two-ion hybrid resonance layer exists in the torus. Figure 4 shows $\tilde{B}_\theta$ as a function of the major-radius location of the fundamental cyclotron resonance layer for hydrogen, where the frequency was fixed at 25 MHz and ε_p = 5-10 %. As was reported from TFR [5] and ATC [11], wave damping is asymmetric with respect to the plasma center.

6.1.4.2 Heating experiments

We first examined the response of charge-exchange neutral spectra, varying the toroidal field, i.e. the position of the fundamental cyclotron resonance layer for hydrogen. Figure 5 shows some examples of charge-exchange neutral spectra and corresponding cyclotron resonance layers. In these examples, ε_p was kept to be 5∿10 %. The features of these spectra are as follows: (A) The cyclotron resonance layer was located on the inner side of the plasma cross-section: ΔT_i was medium and no high-energy tail was present; (B) the cyclotron resonance layer was located on the outer side of the plasma cross-section: ΔT_i was large and also no high-energy tail was present; (C) the cyclotron resonance layer was located on the outer edge of the plasma cross-section: ΔT_i was medium and a remarkable high-energy tail was built up. Figure 6 compares the time evolutions of the count numbers of charge-exchange neutrals at 1.5 keV, in these cases. The e-folding decay times of the count numbers after the end of the RF pulse were (A) 0.7 ms, (B) 1.5 ms and (C) <0.3 ms, respectively. This indicates that the heating took place in the most central region in case B. It is consistent with the fact that the two-ion hybrid resonance layer was located most closely to the plasma center in case B since the two-ion hybrid resonance layer lies on the high-field side of the cyclotron resonance layer, and strong wave damping occures near the two-ion hybrid resonance layer, in accordance with mode-conversion theory [10]. Figure 7 shows the ion temperature increase ΔT_i divided by the RF net power as a function of the toroidal field — the position of the cyclotron resonance layer for hydrogen. The variation of $\Delta T_i/P_{Net}$ is asymmetric with respect to the plasma centre. The maximum $\Delta T_i/P_{Net}$ was obtained at $B_T \sim 18$ kG, which is consistent with the fact that the wave damping variation displays deep valley at $B_T \sim 18$ kG as shown in Fig. 4. Next, we examined the response of the charge-exchange neutral spectra to the ratio of proton to deuteron density, ε_p, keeping

the toroidal field at 18 kG and 16.4 kG. Figure 8 shows some examples of charge-exchange neutral spectra for different values of ε_p. Here, the toroidal field was fixed at 18 kG. Profiles of the L_α lines of deuterium and hydrogen were measured by the monochromator for each case. They are also shown in Fig. 8, where the curves are normalized at the peak corresponding to deuterium. Hydrogen and deuterium atoms have almost the same excitation rate coefficients and transition probabilities. ε_p was determined to be

$$\varepsilon_p = \frac{\sqrt{2}\, P_H}{\alpha P_D}$$

where P_D and P_H are the peak values of the L_α lines of deuterium and hydrogen, respectively, assuming identical temperatures, and α is a correction factor for the absorption effect of the deuterium L_α line by the ground levels of deuterium. A rough calculation shows that α is almost unity for the present experiment [16].

Other measurements like mass analysis of the gas in the device after discharges yielded values considerably different from those obtained by spectroscopy. The ratios of amounts of hydrogen to deuterium gases after discharges were 1.6 and 1.9 %, while the ε_p values measured by spectroscopy during the discharges were 9 and 17 %, respective/y. We adopted data from spectroscopy since a mass-analyser measuring point located within the vacuum pump is away from the first wall in the torus.

The features of spectra as shown in Fig. 8 are as follows: (D) For ε_p < 5 %, a remarkable high energy tail was built up and ΔT_i was medium; (B) For ε_p = 5∿10 %, the high-energy tail disappeared, and ΔT_i was large; (E) For ε_p > 10 %, there was no high-energy tail either, but ΔT_i was small. The decay time of the high-energy tail in case D was 1.2 ms, which was comparable with that of the bulk ion temperature 1.5 ms. In addition, the former is much longer than that of the high energy tail in case C, 0.3 ms. Figure 9 shows $\Delta T_i/P_{Net}$ as a function of ε_p. It can be concluded that the most favourable heating is realized at ε_p = 5∿10 % for B_T = 18 kG.

The radial profile of the ion temperature in the case of ε_p = 5-10 % and B_T = 18 kG was determined from the Doppler broadening of OVII (1623 Å), CV (2271 Å) and CIV (1548 Å) lines and from the localization of line intensities (Fig. 10). The localization of the impurity emissions was

experimentally confirmed by measuring the spatial distributions of their total line intensities. The spatial distributions of the total line emission coefficients were o-tained by applying the Abel inversion method to the radiances observed along different horizontal chords. For the central ion temperature, data from the charge-exchange were adopted. The ion temperatures in the scrape-off layer were measured by the multigrid analyzer and the Katsumata probe. The ion heating in the overall plasma cross-section is shown in Fig. 10; the radial profiles of electron temperature and density are depicted in Fig. 11. The latter was obtained from an Abel inversion of the line densities measured by the microwave interferometer, and data from laser scattering were also plotted (only in the central core). The change in the electron density profile was small, if any at all. For the electron temperature profile, peripheral electron heating was observed. When ε_p was smaller than 5 %, no electron heating occurred in the whole plasma cross-section.

6.1.5 Discussion

The results can be compared with the mode-conversion theory by Jacquinot [17]. According to Jacquinot, a threshold of ε_p exists for the mode conversion. Below the threshold, a main part of the RF power goes to the protons, resulting in the formation of a high-energy tail. Near the threshold, the second-harmonic cyclotron damping of deuteron is enhanced by the proximity of the two-ion hybrid resonance [11]. In the experimental results, a remarkably high-energy tail was built up, and ΔT_i was medium for $\varepsilon_p < 5$ %; the high-energy tail disappeared, and ΔT_i was large for $\varepsilon_p = 5 \sim 10$ %. For a threshold of ~ 5 %, they are consistent, although no quantitative comparison has been made, as yet. Above the threshold, the theory expects significant coupling of the RF power to the electrons. No electron heating was, however, observed in the present experiment. This is probably due to the use of the half-turn antenna placed on the low-field side since the wave is reflected on the cut-off surface till it reaches the mode-conversion layer [18].

Next we consider power balances by using the radial profiles shown in Fig. 10 and 11.

The steady-state power balances for ions with and without RF power are given by

$$P'_{ei} + P^i_{RF} - \frac{W'_i}{\tau'_{Ei}} = 0 \qquad \text{with RF power} \qquad (1)$$

$$P_{ei} - \frac{W_i}{\tau_{Ei}} = 0 \qquad \text{without RF power} \qquad (2)$$

where P_{ei}, P^i_{RF}, W_i and τ_{Ei} are power transferred from electrons to ions, the RF power to ions, energy of the ions and the ion energy confinement time, respectively; the prime denotes quantities with RF power. W_i, W'_i, P_{ei} and P'_{ei} are calculated from the radial profiles of $T_i(r)$, $T_e(r)$ and $n_e(r)$ shown in Figs. 10, 11, on the assumption of equal perpendicular and parallel temperatures. These are tabulated in Table 1.

The power balance after the end of the RF pulse is described by

$$\frac{dW'_i(t)}{dt} = P'_{ei}(t) - \frac{W'_i(t)}{\tau'_{Ei}(t)} \qquad (3)$$

From Eq. (1) and (3), P^i_{RF} is expressed as $P^i_{RF} = -\left.\frac{dW'_i(t)}{dt}\right|_{t=t_2}$, where t_2 is the time where the RF pulse ends.

Writing the time evolution of $W'_i(t)$ after the termination of the RF pulse as

$$W'_i(t) = (W'_i - W_i)\exp(-\frac{t}{\tau_s}) + W_i$$

we can write P^i_{RF} as

$$P^i_{RF} = \frac{W'_i - W_i}{\tau_s} \qquad (4)$$

Here τ_s is the e-folding decay time of the bulk ion temperature after the end of the RF pulse; it is related to τ'_{Ei} as follows:

$$\tau_s = \frac{(W'_i - W_i)\tau'_{Ei}}{W'_i - P'_{ei}\,\tau'_{Ei}} \qquad (5)$$

Experimentally, τ_s was determined from the time evolution of the ion tempetature shown in Fig. 2 and was 1.5 ms. Then, P^i_{RF} = 38 kW. The ion heating efficiency is defined as the ratio of P^i_{RF} to the RF net power P_{Net}. The efficiency is about 40 %. From Eqs. (1) and (2), τ_{Ei} and τ'_{Ei} are calculated to be 4.8 ms and 3.7 ms, respectively. These results contain substantial experimental errors ($\sim$30 %). Nevertheless, the reduction in

ion energy confinement time when RF power is applied can be explained by neoclassical scaling (plateau regime) of the ion energy confinement [19].

The steady-state power balances for electrons with and without RF power are given as

$$P_{OH} - P'_{ei} + P^{e}_{RF} - \frac{W'_e}{\tau'_{Ee}} = 0 \qquad \text{with RF power} \qquad (6)$$

$$P_{OH} - P_{ei} - \frac{W_e}{\tau_{Ee}} = 0 \qquad \text{without RF power} \qquad (7)$$

where P_{OH}, P^{e}_{RF}, W_e and τ_{Ee} are the Ohmic input power, the RF power to the electrons, the energy of electrons and the electron energy confinement time, respectively. The values of P_{OH}, W_e and W'_e are shown in Table 1. P^{e}_{RF} is unknown since the time evolution of the electron temperature after the end of RF pulse has not been measured. τ_{Ee} and τ'_{Ee} are calculated to be 2.2 ms and 1.9 ms, respectively, assuming $P^{e}_{RF} = 0$. Thus, RF heating causes no change in ion and electron energy confinement. The rest of the RF power went presumably to the edge plasma although the details are not yet clear.

Conclusions

The ICRF heating expeiment using the 2 ω_{CD} frequency for a deuteron plasma with a minority proton component was performed under extremely pure-wall condition ($Z_{eff} \simeq 1$).

(1) The RF net power was up to 140 kW; an RF net energy of 1 kJ was applied.

(2) No change in the one-turn loop voltage and the electron density was observed.

(3) The maximum of $\Delta T_i/P_{Net}$ was observed at B_T = 18 kG and ε_p = 5∿10 %;
  (i) the ions were heated in the overall plasma cross-section;
  (ii) no high-energy tail was built up;
  (iii) no adverse effects on plasma confinement were observed;
  (iv) the ion heating efficiency was about 40 %.

(4) The results were consistent with mode-conversion theory.

References

[1] DIVA GROUP, Nucl. Fusion 18 (1978) 1619.

[2] IVANOV, N.V., KOVAN, I.A., LOS', E.V., JETP Lett. 14 (1971) 138.

[3] VDOVIN, V.L., ZINOV'EV, O.A., IVANOV., A.A., KOZOROVITSKII, L.L., PARAIL, V.V., et al., JETP Lett. 14 (1971) 149.

[4] HOOKE, W.M., HOSEA, J.C., in Controlled Fusion and Plasma Physics (Proc. 5th Europ. Conf., Grenoble, 1972) Vol.1, (1972) 107; HOSEA, J.C., HOOKE, W.M., Phys. Rev. Lett., 31 (1973) 150; ADAM, J., CHANCE, M., EUBANK, H., GETTY, W., HINNOV, E., et al., in Plasma Physics and Controlled Nuclear Fusion Research (Proc. 5th Int. Conf., Tokyo, 1974) Vol. 2, IAEA, Vienna (1975) 65.

[5] TFR GROUP, in Theoretical and Experimental Aspects of Heating Toroidal Plasmas (Proc. 3rd Int. Meeting Grenoble, 1976) Vol. 1 (1976) 87; TFR GROUP, in Plasma Physics and Controlled Nuclear Fusion Research (Proc. 6th Int. Conf., Berchtesgaden, 1976) Vol. 3 (1977) 39.

[6] VDOVIN, V.L., SHAPOTKOVSKII, N.V., RUSANOV, V.D., in Theoretical and Experimental Aspects of Heating Toroidal Plasmas (Proc. 3rd Int. Meeting Grenoble, 1976) Vol.2 (1976) 349.

[7] BUZANKIN, V.V., VERSHKOV, V.A., IVANOV, N.V., KOVAN, I.A., KRUPIN, V.A., et al., in Plasma Physics and Controlled Nuclear Fusion Research (Proc. 6th Int. Conf., Berchtesgaden, 1976) Vol.3 (1977) 61.

[8] TAKAHASHI, H., DAUGHNEY, C.C., ELLIS, Jr., R.A., GOLDSTON, R.M., HSUAN, H., et al., Phys. Rev. Lett. 39 (1977) 31.

[9] JACQUINOT, J. MCVEY, B.D., SCHARER, J.E., Phys. Rev. Lett. 39 (1977) 88.

[10] PERKINS, F.W., Nucl. Fusion 17 (1977) 1197.

[11] TAKAHASHI, H., ICRF Heating in Tokamaks, Princeton Plasma Physics Lab. Report, PPPL-1374 (1978).

[12] TFR GROUP, in Heating in Toroidal Plasmas (Proc. Joint Varenna-Grenoble Int. Symp. Grenoble, 1978).

[13] SUGIE, T., TAKEUCHI, H., KASAI, S., FUNAHASHI, A., TAKAHASHI, K., KIMURA, H., J. Phys. Soc. Japan, 44 (1978) 1960.

[14] KIMURA, H., ODAJIMA, K., SUGIE, T., MAEDA, H., Jpn. J. Appl. Phys. 18 (1979) 2275 [Section 2.3 in this thesis].

[15] ODAJIMA, K., KIMURA, H., MAEDA, H., OHASA, K., Jpn. J. Appl. Phys. 17 (1978) 1281.

[16] MITCHELL, ALLAN C.G., ZEMANSKY, MARK W., Resonance Radiation and Excited Atoms, Chapter 3, Cambridge University Press (1961).

[17] JACQUINOT, J., in Heating in Toroidal Plasmas (Proc. Joint Varenna-Grenoble Int. Symp. Grenoble, 1978).

[18] JACQUINOT, J., MESSIAEN, A., EC INTOR REPORT, Heating, Appendix 5 (June, 1979).

[19] KIMURA, H., ODAJIMA, K., SENGOKU, S., IIZUKA, S., SUGIE, T., et al., ICRF Heating in DIVA: Parameter Survey and Very High Efficiency Ion Heating Experiment, Japan Atomic Energy Research Institute Report, JAERI-M 8429 (1979).

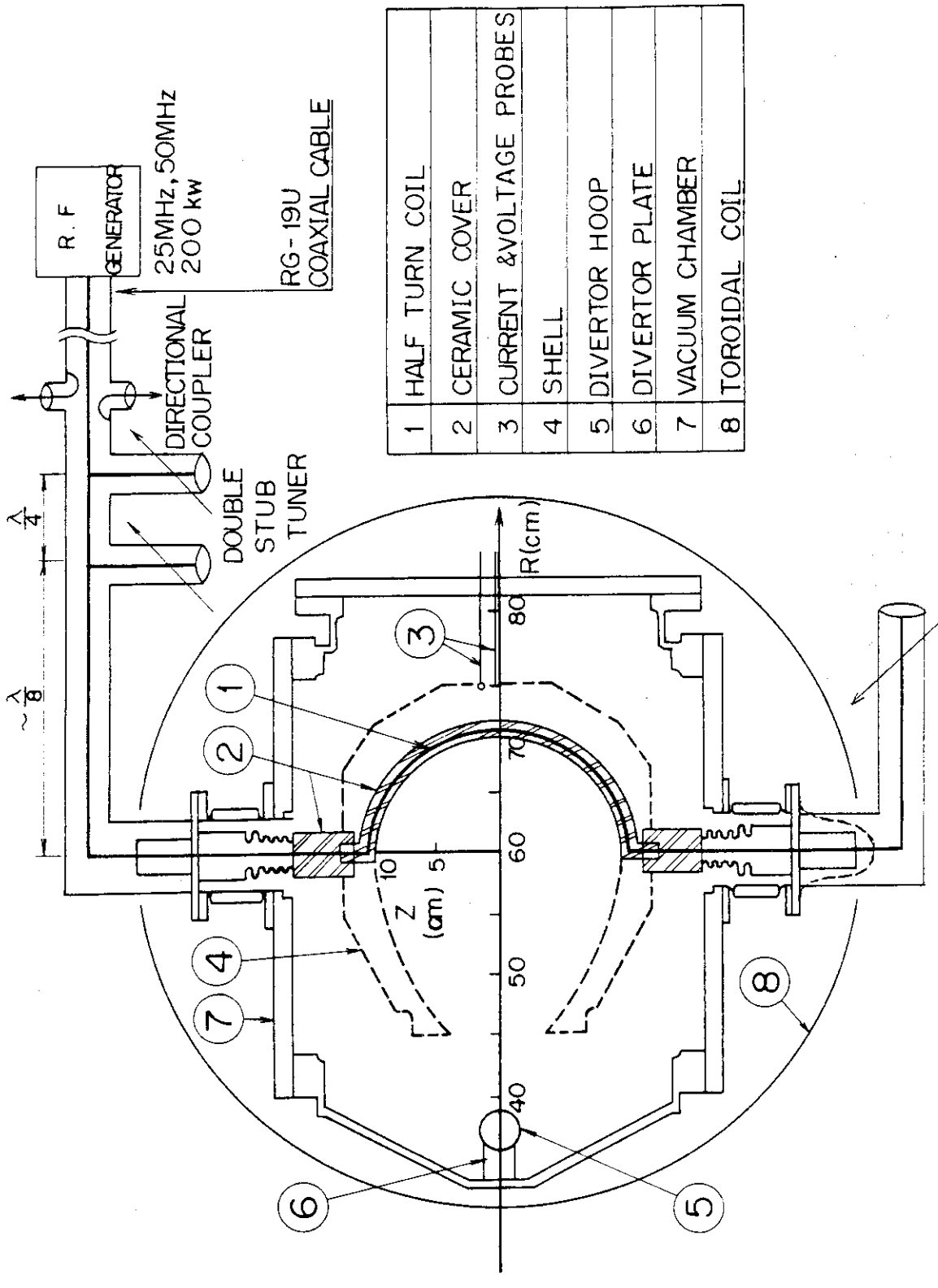

Fig. 1 Cross-sectional view of DIVA together with launching structure (antenna), matching network and transmission line.

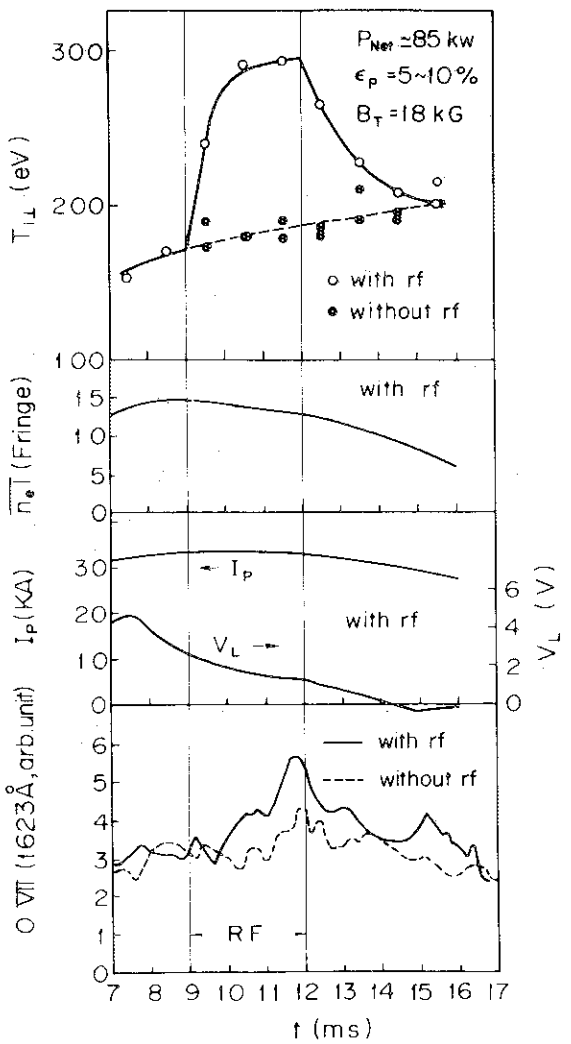

Fig. 2 Time evolution of perpendicular ion temperature $T_{i\perp}$(CX), electron line density $\overline{n_e \ell}$, plasma current I_p, one-turn loop voltage V_L and spectral line intensity OVII (1623 Å)

$B_T = 18$ kG, $\epsilon_p = 5\sim10\%$

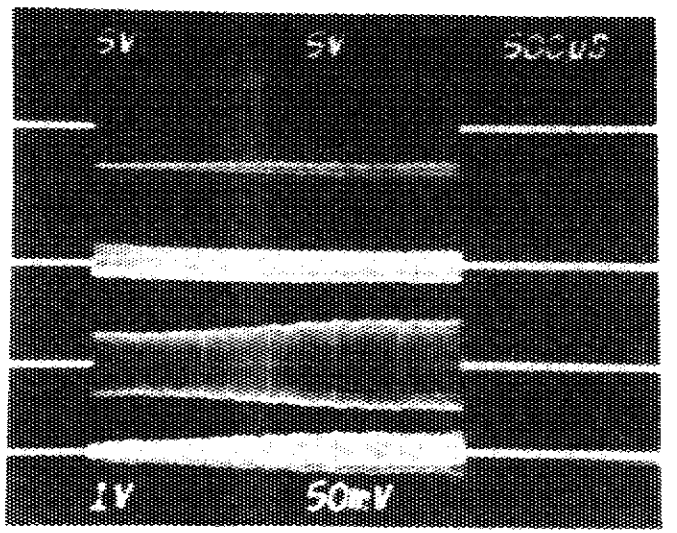

OUTPUT OF DIRECTIONAL COUPLER, CURRENT PROBE AND MAGNETIC PROBE.

Fig. 3 Typical signals of square roots of incident and reflected RF powers $\sqrt{P_f}$, $\sqrt{P_b}$, coil current, I_C and magnetic fluctuation B_θ.

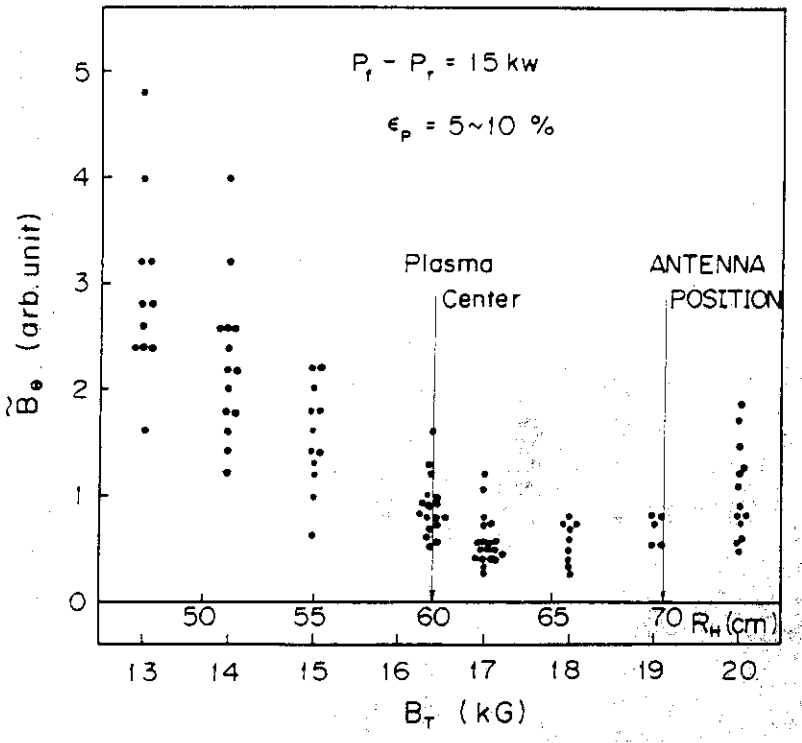

Fig. 4 Magnetic fluctuation $\tilde{B}_\theta$ as a function of toroidal field B_T or major radius location of fundamental cyclotron resonance layer for hydrogen R_H. The frequency is fixed at 25 MHz and ε_p = 5 ~ 10 %.

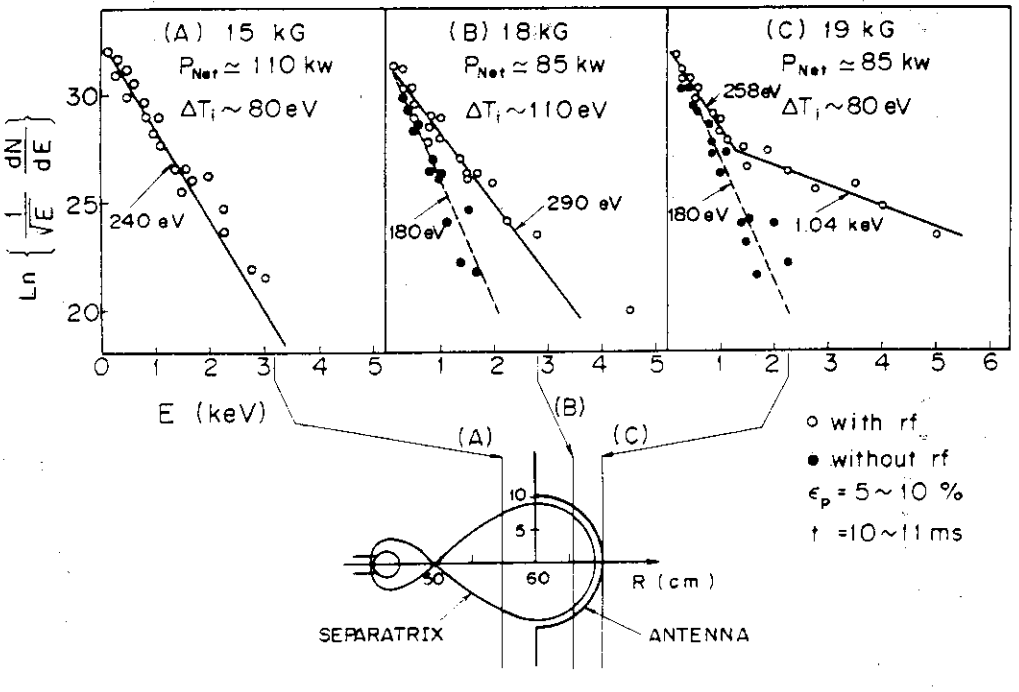

Fig. 5 Charge-exchange neutral spectra for different toroidal fields and corresponding fundamental cyclotron resonance layers for hydrogen. ε_p is kept at 5 - 10 %.

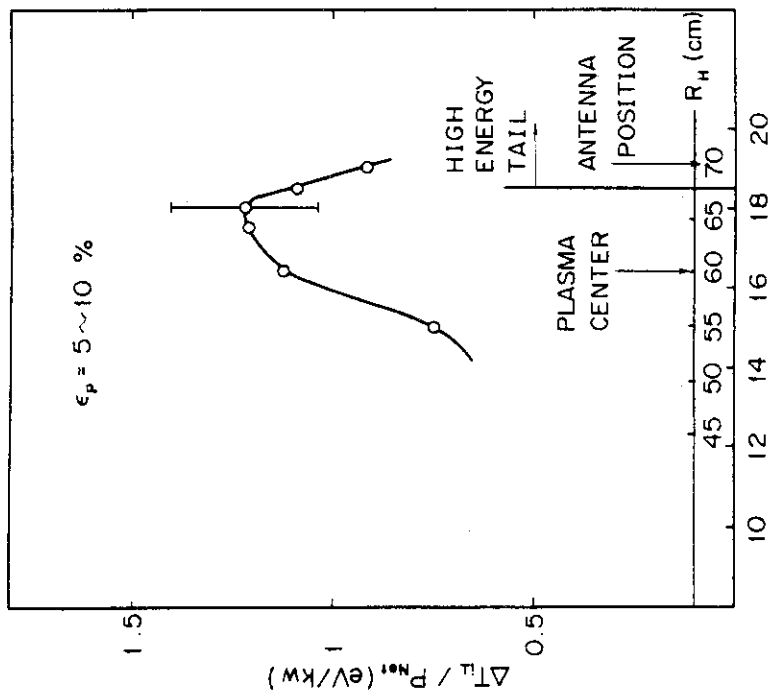

Fig. 7 Increase in ion temperature per unit RF net power versus toroidal field or position of cyclotron resonance layer for hydrogen. ε_p is kept at 5 - 10 %.

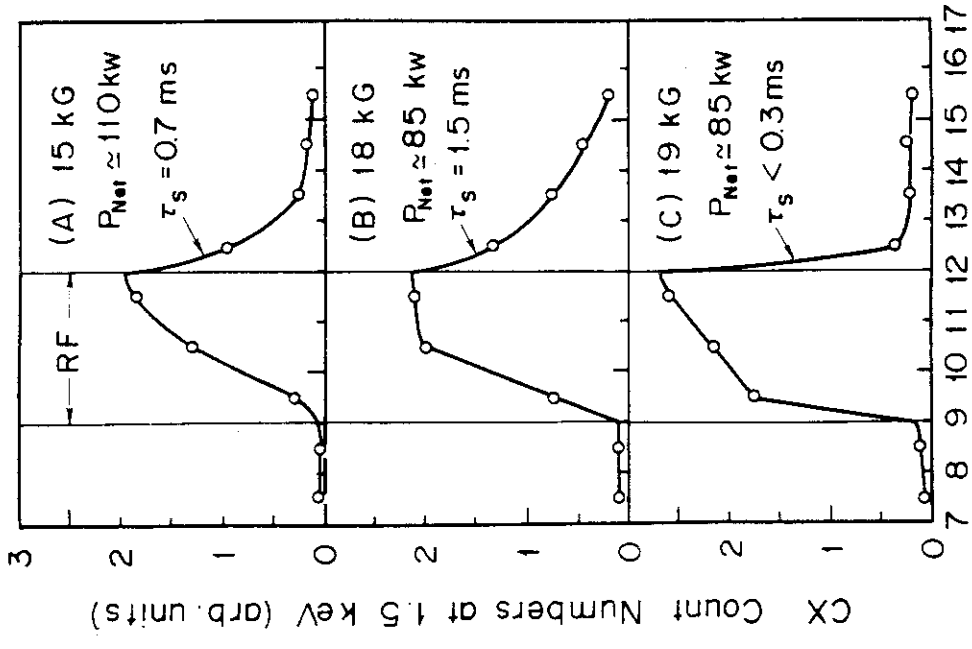

Fig. 6 Time evolution of count numbers of charge-exchange neutrals at 1.5 keV corresponding to the spectra shown in Fig. 5.

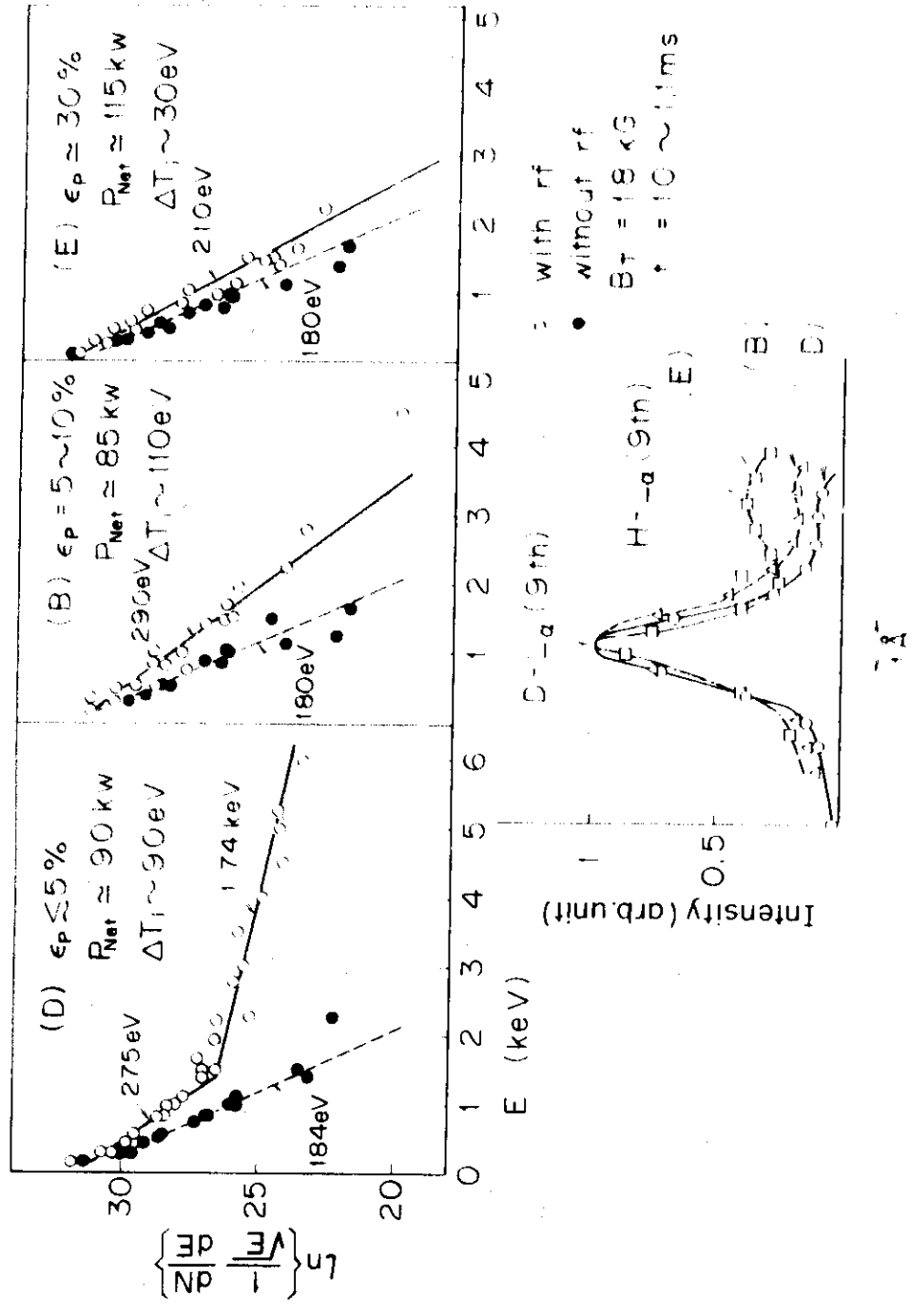

Fig. 8 Charge-exchange neutral spectra for different values of ϵ_p and corresponding profiles of L_α lines of deuterium and hydrogen. The toroidal field was fixed at 18 kG.

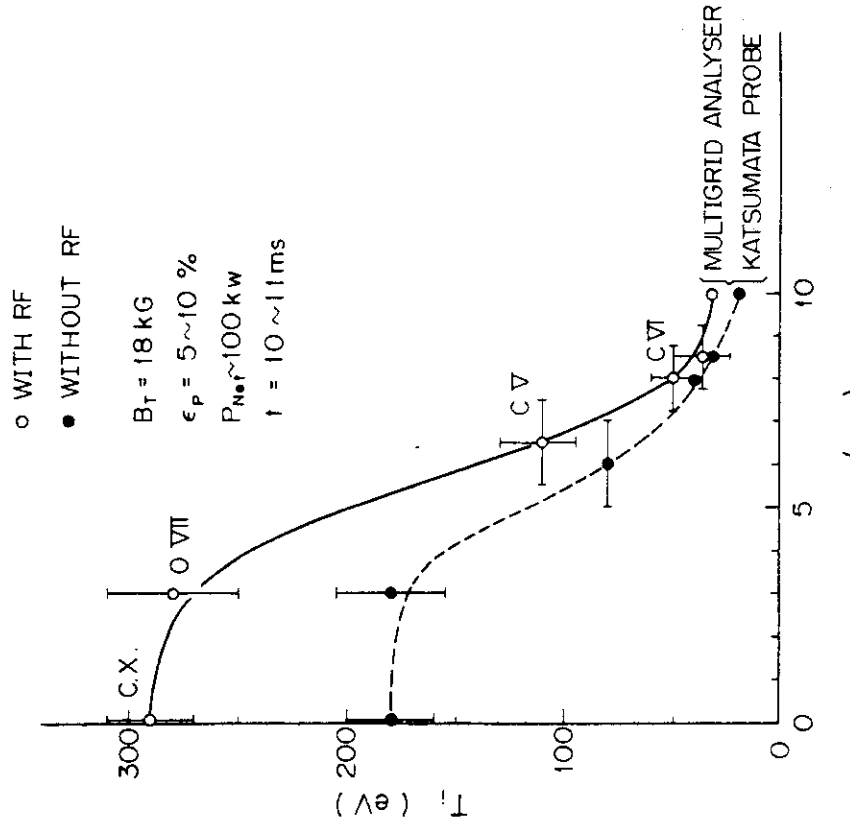

Fig.10 Radial profiles of ion temperature with and without RF power in the case of ε_p = 5 - 10 % and B_T = 18 kG.

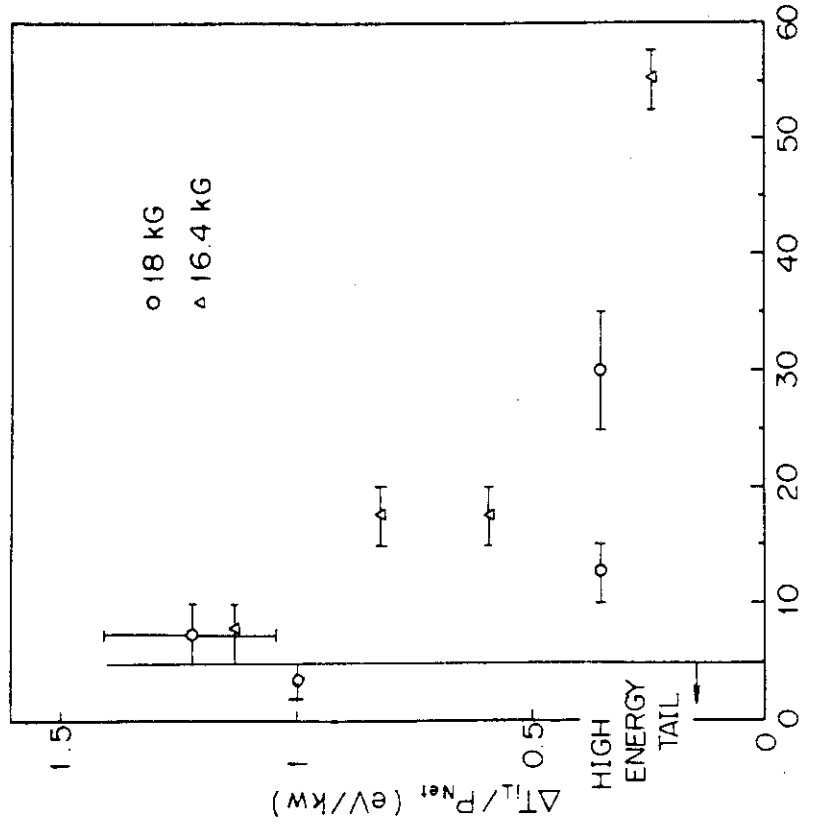

Fig. 9 Increase in ion temperature per unit RF net power as a function of ε_p. The toroidal field is fixed at 18 and 16.4 kG.

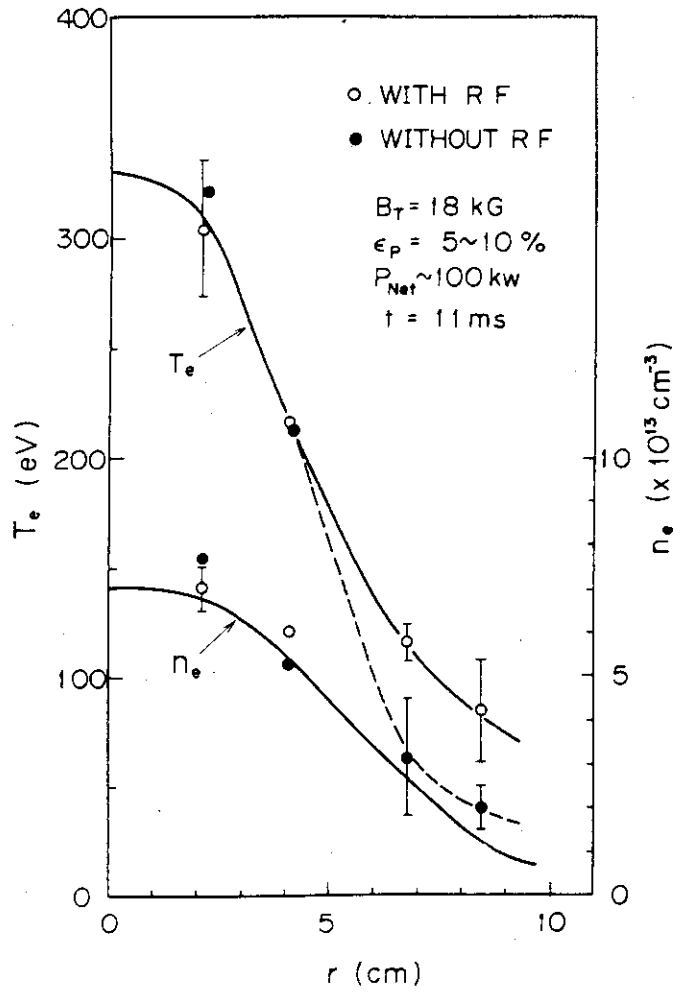

Fig.11 Radial profiles of electron temperature and density with and without RF power in the case of ε_p = 5 - 10 %, B_T = 18 kG.

Table 1 Power balances with and without RF power.
$P_{OH} \simeq 85$ kW, $P_{Net} \simeq 100$ kW, ε_p = 5 - 10 %, B_T = 18 kG.

W_e	W_i	P_{ei}	τ_{Ee}	τ_{Ei}					WITHOUT RF
141 Joule	95 Joule	20 kW	2.2 ms	4.8 ms					
W'_e	W'_i	P'_{ei}	τ'_{Ee}	τ'_{Ei}	P^e_{RF}	P^i_{RF}	η_e	η_i	WITH RF
158 Joule	151 Joule	3 kW	$\lesssim$1.9 ms	3.7 ms	?	38 kW	?	~40%	

6.2 Power Balance During ICRF Heating

6.2.1 Introduction

In the previous section, we obtained the ion heating efficiency η_i of about 40 % for the best case. The rest of the RF power was deposited directly to the boundary plasma. A rapid increase of the boundary electron temperature was observed on applying the RF pulse. The surface heating is mainly due to the acceleration of plasma particles by the electric field between the antenna and the shell.

This time, we have installed a Faraday shield [1] closely over the antenna ceramic cover in order to avoid the electrostatic coupling. The antenna loading impedance and the boundary plasma temperature are compared between the cases with and without the Faraday shield. The Faraday shield reduces the antenna impedance significantly and increases the heating efficiency by a factor of 2.3; which is due to the cancellation of the potential gap between the antenna and the shell. We obtain the heating efficiency η_i = 61 $\sim$ 85 % with the Faraday shield and η_i' = 27 $\sim$ 33 % without it from the consideration of the gross power balance including the boundary plasma. η_i' = 27 $\sim$ 33 % is consistent with one derived from the decay of the ion temperature after the end of the RF pulse as described in the previous section.

The heating efficiency is also evaluated from a 1-D tokamak simulation code. The time evolution and the radial profile of the ion temperature are well simulated with a 1-D tokamak code having 2 $\sim$ 3 times enhancement of the ion thermal conduction over the neoclassical value, assuming a rectangular profile of the RF-power deposition of 3 cm radius; the narrow power deposition is consistent with a fact that the excited fast wave is converted to the ion Bernstein wave [2] and damped strongly by the plasma particles near the two-ion hybrid resonance layer which is located near the plasma centre. We obtain the heating efficiency of 83 % from the simulation for the case with the Faraday shield.

From PLT [3] and TFR [4], it was reported that a greater part of the RF-power entered into the minority proton component and then the majority deuteron was heated by collisional process. Indeed in our experiment, a slightly higher energy component is present in the charge-exchange neutral spectrum, where the analyzer is not capable of discriminating the mass difference. We regard this as a proton component since the average energy

of the high-energy component increases with decreasing proton-to-deuteron density ratio; this is the consequence of the mode-conversion theory [5]. However, the analysis similar to PLT and TFR on the basis of the Fokker-Planck equation shows that the power transferred from protons to deuterons alone cannot sustain the observed deuteron temperature. We conclude that about 70 % of the RF power goes directly to deuterons and the power transferred from protons to deuterons via collisions is less than 15 %.

Thus, we have succeeded in the very high efficiency majority deuteron heating in the plasma core and confirmed it from the power balance study.

6.2.2 Faraday Shield and Other Improvements [6]

The Faraday shield is made of molybdenum strips (5 mm azimuthally × 1 mm radially, separated by a 5 mm gap) and U-shaped stainless-steel covers which surround back and side surfaces of the ceramic cover and has two gaps azimuthally. The ends of the strips are connected to the stainless-steel covers, which are terminated to the shells.

One of the other problems associated with ICRF heating experiment is RF breakdown. It occurs at the antenna and the power feed-through insulator. In order to prevent RF breakdown, the antenna cleaning is performed by supplying the RF power in the absence of the plasma and generating RF discharges. If they do not occur, the RF power is raised gradually till they begin to occur again. These procedures are continued up to a desirable RF current level. In the previous experiment, the end of the antenna is terminated to the vacuum vessel. This time we connect $\sim \frac{\lambda}{2}$ coaxial cable with an adjustable short-circuit end, and set the midpoint of the antenna to be a voltage null point (see Fig. 1 in Section 6.1). The voltage at the power feed-through is reduced to 50 % for the same RF input power.

By means of above-mentioned improvements, the antenna current has increased by a factor of 2, suggesting the effective RF power which is absorbed by the plasma has become about 4 times higher than in the previous experiment described in Section 6.1.

6.2.3 Gross Power Balance Including the Boundary Plasma

6.2.3.1 Loading impedance

The measurement by the directional coupler and the antenna current probe yields the loading impedance R_s. Figure 1 shows time evolutions of the loading impedance with and without the Faraday shield. It is shown

that the loading impedance with the Faraday shield is reduced to less than half of that without the Faraday shield. The reduction is due to the cancellation of the electrostatic coupling by the Faraday shield.

The loading impedances change with time irrespective of the Faraday shield. The correlation between R_s and the plasma edge density is clear. Figure 2 shows a time evolution of the divertor ion saturation current together with the loading impedance. The divertor particle flux, hence the plasma density at the antenna edge, decreases on applying the RF pulse. The loading impedance decreases with decreasing edge density. From ATC [7], it was reported that the cross-field diffusion was enhanced at the plasma edge by the RF power. Similar phenomena are observed in DIVA. Particle flux to the wall increases, while one to the divertor decreases. The particle divertor efficiency [8] is reduced from 22 % without RF to 16 % with RF for the case with the Faraday shield and $P_{Net} \sim$ 115 kW. The physical mechanism of the enhancement of the cross-field diffusion has not been made clear. The formulation of the antenna impedance which explains the experimental values and the dependence on the plasma edge density is needed.

The reduction of the loading impedance induces the decrease of the RF net power since a ratio of the circuit loss to the plasma loading becomes larger with decreasing loading impedance. Figure 2(c) shows the temporal change of the RF net power.

6.2.3.2 Heating efficiency

The equivalent antenna loading impedance R_s is divided into three components.

$$R_s = R_1 + R_2 + R_c \qquad (1)$$

R_1, R_2 and R_c are impedances related to a core heating, a surface heating and a circuit loss, respectively. The surface heating is due to the acceleration of plasma particles by the potential gap between the antenna and the shell as well as due to the wave heating if the wave has a large damping decrement in the surface. R_c is earily measured by applying the RF pulse in the absence of the plasma.

One can write $P_{RF} = R_1 I_c^2$, $P_{Net} = (R_1+R_2) I_c^2$ amd $\eta_i = \frac{R_1}{R_1+R_2}$, where P_{RF} and I_c are the RF power absorbed in the plasma core and the antenna

current, respectively. It is confirmed that P_{Net} is roughly equal to the sum of the increases of the heat fluxes to the shell and the divertor (see Chapter 5). The results are tabulated in Table 1 for the case without the Faraday shield and of B_T = 18 kG and $\varepsilon_p \sim 15$ %. The RF power, once spent to the core ion heating and the surface heating, is finally transformed to the conduction-convection loss to the material surfaces, whether the core ion heating is large or small.

The ratio of the core heating to the surface heating is evaluated in the following way: Figure 3 shows ΔT_i as a function of P_{Net} for the cases of B_T = 17.5 $\sim$ 18 kG and ε_p = 5 $\sim$ 10 % with and without the Faraday shield. It is shown that ΔT_i is in proportion to P_{Net}. Data with the Faraday shield lie on the line of 2.3 eV/kW, those without one on the line of 1 eV/kW. The proportional coefficient is written as

$$\Delta T_i \propto R_1 I_c^2 = \frac{R_1}{R_s - R_c} P_{Net} \tag{2}$$

Figure 4 shows the increase of the boundary electron temperature ΔT_{eb} versus P_{Net}. In addition to the cases in Fig. 3, a case of $\varepsilon_p \sim 15$ % and without the Faraday shield is included. Similarly to the equation (2),

$$\Delta T_{eb} \propto R_2 I_c^2 = \frac{R_2}{R_s - R_c} P_{Net} \tag{3}$$

It is noted that the slope with the Faraday shield, in turn, is smaller than that without the Faraday shield.

The ratios of the proportional coefficients between the cases with and without the Faraday shield are

$$\frac{R_1}{R_s - R_c} \Big/ \frac{R_1'}{R_s' - R_c'} = \alpha \qquad \text{for } \Delta T_i \text{ ,} \tag{4}$$

$$\frac{R_2}{R_s - R_c} \Big/ \frac{R_2'}{R_s' - R_c'} = \beta \qquad \text{for } \Delta T_{eb} \tag{5}$$

where the prime denotes the quantity of the case without the Faraday shield.

From Eqs. (4) and (5), η_i and η_i' are derived.

$$\eta_i = \frac{\alpha(1-\beta)}{\alpha - \beta} \tag{6}$$

$$\eta_i' = \frac{1-\beta}{\alpha - \beta} \tag{7}$$

One can known α and β from each pair of lines in Figs.3 and 4 (the proportional coefficient of ΔT_i for the case of $\varepsilon_p \sim 15$ % is about half of the case of $\varepsilon_p = 5 \sim 10$ % as shown in Fig. 9 of Section 6.1). We then obtain η_i and η_i' from equations (6) and (7). The results are shown in Table 2. Inspite of the limited data with large error bars for the case without the Faraday shield, the result is reasonable. From the decay of the ion temperature, we obtained the heating efficiency of about 40 % for the case of $\varepsilon_p = 5 \sim 10$ % and without the Faraday shield as described in Section 6.1. The obtained value of η_i is somewhat underestimated since the increase of the edge temperature is partly due to the conduction-convection loss from the additionally heated core plasma. Fortunately, however, electron heating in the core plasma is small in the present experiment.

In the case with the Faraday shield, the increase of the boundary electron temperature is not wholly explained by the electrostatic coupling. Figure 5 compares time evolutions of the boundary ion and electron temperatures measured by the multigrid energy analyzer for various toroidal magnetic fields. It is shown that the increase of the electron temperature is dependent on the toroidal field. In the case of $B_T = 20$ kG, the cyclotron resonance layer is outside the plasma cross-section and the electron temperature increase is small. This indicates that the surface heating due to the electrostatic coupling is also small for the cases of $B_T = 17.5$ and 19 kG since the electrostatic coupling must be independent of the toroidal field.

Therefore, the surface heating in the case with the Faraday shield is explained mainly by the wave damping in the plasma boundary. The surface heating is most prominent in the 19 kG-case, where the cyclotron resonance layer is tangent to the antenna. The ion heating in the 20 kG-case is comparable with that of the 19 kG-case; the result differs from that of the electron heating. This suggests that the ion heating takes place near the mode conversion layer which is still in the plasma cross-section even in the 20 kG-case, and that the electron heating is localized near the cyclotron resonance layer. The suggestion is justified from the profile of the wave damping decrement along the major radius direction shown in Fig. 10.

In summary, we have evaluated the heating efficiency from the point of view of the partition of the heating power to the core plasma and the

boundary plasma. We have obtained η_i = 61 ∿ 85 % in the case of B_T = 17.5 kG and ε_p = 7 ∿ 9 % and with the Faraday shield.

6.2.4 Power Balance of the Core Plasma

6.2.4.1 Experimental results

As discussed in Section 6.1, the optimum ion heating occurs at B_T = 17.5 - 18 kG and ε_p = 5 ∿ 10 %. In this conditions, the two-ion hybrid resonance layer lies in the vicinity of the magnetic axis. It has been shown that 61 ∿ 85 % of the RF net power is absorbed by the ions in the plasma core for the case with the Faraday shield, from the consideration of the gross power balance.

Here, more detailed results on the ion heating with the Faraday shield under the optimum conditions, i.e. B_T = 17.5 - 18 kG, ε_p = 7 ∿ 9 % and $\bar{n}_e = 3.5 \times 10^{13}$ cm^{-3}, is described.

Figure 6 shows the time evolution of the ion temperature measured by the charge-exchange neutral energy analyzer. It is shown that the ion temperature increased from 160 eV to 430 eV in application of the 115 kW RF net power. Charge-exchange neutral spectra sampled from 10 to 12 ms are shown in Fig. 7. The charge-exchange analyser is not capable of discriminating mass differences and its signal contains both contributions from deuterium and hydrogen. The ion temperature is determined from the linear part of the spectra up to the neutral energy of 2.0 keV. A significant amount of slightly higher energy component is present. The decay time of the higher energy component after the end of the RF pulse is about 0.6 ms, which is comparable with that of the bulk component. The origin of the higher energy component is discussed later.

Radial profiles of the ion temperature are shown in Fig. 8, which were measured with the technique described in Section 6.1. The ion temperature profile is peaked by the RF power. The result suggests that the RF power is absorbed in the central region of the plasma column.

Unfortunately, those of the electron temperature were not measured for the present case. However, the electron temperature increase may be at most 20 % because we can extrapolate it from the 10 % increase in the case of P_{Net} ∿ 70 kW. Comparing Fig. 11 in Section 6.1 and Fig. 8, it is found that the ion temperature exceeded the electron temperature over the whole plasma cross-section.

Figure 9 shows the ion temperature increases versus the RF net power.

The solid curve is a neoclassical heat conduction loss power density near the centre of the column, assuming the platean regime with the same coefficient as that obtained for the Ohmically heated plasmas [8]. The ion temperature should be determined from the balance between the RF input power and sum of various loss powers. Therefore, the RF input power density near the centre is at least as same as the thermal conduction loss power density based on the neoclassical theory. The thermal conduction occupys a main part of the loss power in DIVA, which is larger by a factor of ten than that of the base plasma for the maximum RF input power.

Comparing both abscissa in Fig. 9, we can know that the RF input power is absorbed inside the central column with radius 3-3.5 cm, assuming that all of the RF power heats ions. From this consideration, it can be concluded that a large part of the RF power is absorbed by ions in the narrow central region.

6.2.4.2 Numerical simulation

A one-dimensional tokamak code [9] is used to simulate the ion heating. The ion heat conduction coefficient is taken to be neoclassical with an anomaly factor of three. The electron heat conduction and the particle diffusion are assumed to follow the Alcator scaling. As mentioned above, the RF input power is absorbed inside the central column with a radius of 3-3.5 cm. We assume a rectangular power deposition profile with a radius of 3 cm for the majority deuterons. This narrow power deposition is consistent with the calculation of the wave damping decrement along the major radius direction shown in Fig. 10. The power absorption is through the wave damping of a slow electrostatic mode by each species near the mode conversion region [5]. Damping due to deuterons is most dominant and localized in the central region. However, the calculation is only preliminary. We must integrate the damping decrement along the ray trajectory to obtain the power deposition profile.

As discussed in 6.2.3.1, the RF input power changes with time, whose time variation is shown in Fig. 6.

The solid lines in Figs. 6 and 8 show the results of the numerical simulation. The heating efficiency is taken 83 %. The time evolution and the radial profile of the ion temperature are well simulated in spite of the rough estimation of the power deposition profile. As mentioned

above, a main part of the loss power is the ion thermal conduction loss. Heat transfer from ions to electrons is small because of small difference between the ion and electron temperatures. Change-exchange loss is also small because of the high density. The ion energy confinement time τ_{Ei} in the central region is derived from the decay of the charge-exchange neutral temperature after the end of the RF pulse; τ_{Ei} is reduced from 3.6 ms before heating to 0.8 ms during heating. The reduction is explained by the neoclassical scaling in the plateau regime [10] of the ion energy confinement time $\tau_{Ei} \propto T_i^{-3/2}$.

It is concluded that the transport of the RF-heated ions is neoclassical within a factor of 3. The wave excitation, whose power density is higher by ten times than that of the power transferred from electrons to ions in the absence of the RF power, gives no adverse effect to the ion confinement.

6.2.4.3 Heating powers to D^+ and H^+

In the previous paragraph, it has been shown that the increase of the bulk ion temperature is explained by 83 % of the applied P_{Net}. However, a slightly higher energy component appears in the charge-exchange neutral spectrum as shown in Fig. 7. The average energy of the higher energy component is proportional to the RF power. We regard this as a proton component since the average energy of the higher energy component increases with decreasing ε_p as shown in Fig. 8 in Section 6.1 and Fig. 12, which agrees with the theory that the minority proton heating becomes dominant with decreasing ε_p [5]. The value of ε_p at which the proton damping has a maximum is 2.3 %, calculated from Eq. (4) in Ref. [5] using $k_z \sim 0.15$ cm^{-1} [11].

We estimate the heating powers to protons and deuterons in the following way: The solid line in Fig. 7 is a superposition of the theoretical deuterium and hydrogen spectra. For deuterium, we assume one-component Maxwell distribution with the temperature of T_D = 430 eV, and for hydrogen, we use a steady-state solution of the Fokker-Planck equation by Stix [12]. The average energy of the hydrogen $\langle T_H \rangle$ is about 740 eV. One can obtain the local heating power to protons $\langle P \rangle \simeq 1.3$ W/cm . However, this treatment neglects the proton loss channel except the energy transfer from protons to deuterons and electrons.

In order to obtain heating powers to deuterons and protons including

the heat conduction loss, which is the most dominant loss process, we solve a point-model power balance equation for the core plasma:

$$\frac{dw_D}{dt} = p_{eD} + p_{rf}^{D} + p_{HD} - \frac{w_D}{\tau_{ED}} \tag{8}$$

$$\frac{dw_H}{dt} = p_{eH} + p_{rf}^{H} - p_{HD} - \frac{w_H}{\tau_{EH}} \tag{9}$$

where w_j, p_{ej}, p_{rf}^{j}, p_{HD} and τ_{Ej} (j = D, H) are densities of the internal energy of j species, the power transferred from electrons to j species, the RF power to j species and the power transferred from protons to deuterons, and the energy confinement time of j species, respectively. Here, the electron temperature is assumed constant since the increase of the electron temperature was small. The main loss channel of ions is the thermal conduction. Therefore, we assume that τ_{Ej} has the neoclassical scaling in the plateau regime, i.e. $\tau_{Ej} \propto A_j^{-1/2} T_j^{-3/2}$, where A_j is a mass number of j species.

Figure 11 is the result of the computation. In order to match the results with the experimental data, i.e. $T_D \sim 430$ eV and $\langle T_H \rangle \sim 740$ eV, we obtain $p_{RF}^{D} \sim 7.5$ W/cm^3 and $p_{RF}^{H} \sim 3.5$ W/cm^3. The sum of $|p_{eH}|$ and p_{HD} is 1.5 W/cm^3, which is roughly in agreement with one derived from the Stix's formula. The total input power to deuterons including the power transferred from protons is 8.6 W/cm^3. Then the deuteron heating efficiency amounts to 80 %, which is consistent with one derived from the 1-D simulation code, where the proton heating is not taken into account.

It is concluded that the heating power coupled directly to deuterons is more than twice as large as that to protons, for the case of B_T = 17.5 kG, $\varepsilon_p \sim 9$ % and $\bar{n}_e \sim 3.5 \times 10^{13}$ cm^{-3}.

For smaller ε_p, the heating power to protons increases as mentioned above. Figure 12 compares charge-exchange neutral spectra for the cases of $\varepsilon_p \sim 4$ % (close circles) and $\varepsilon_p \sim 8$ % (open circles). The RF net powers are almost same for the two cases. The curves are calculated by using the Stix's formula with the local heating powers to protons $\langle P \rangle = 1.0 \sim 1.2$ W/cm^3 for $\varepsilon_p \sim 4$ % and $\langle P \rangle = 0.4 \sim 0.6$ W/cm^3 for $\varepsilon_p \sim 8$ %. From the power balance equations (8) and (9), one can obtain $p_{RF}^{D} \sim 2.5$ W/cm^3, $p_{RF}^{H} \sim 3.8$ W/cm^3, $|p_{eH}| + p_{HD} \sim 1.1$ W/cm^3 for $\varepsilon_p \sim 4$ % and $p_{RF}^{D} \sim 2.5$ W/cm^3, $p_{RF}^{H} \sim 1.1$ W/cm^3, $|p_{eH}| + p_{HD} \sim 0.73$ W/cm^3 for $\varepsilon_p \sim 8$ %. The results show that the heating power to protons for the case of $\varepsilon_p \sim 4$ % is more than three times of that

for $\varepsilon_p \sim 8$ %. From PLT [3] and TFR [4], it was reported that almost all the RF power is directly absorbed by protons for $\varepsilon_p \sim 5$ %. We have shown that we can control the partition of the heating power to the majority and minority components by selecting the value of ε_p.

References

[1] ROTHMAN, M.A., SINCLAIR, R.M., YOSHIKAWA, S., Plasma Physics 8 (1966) 241.

[2] SWANSON, D.G., Phys. Rev. Lett. 36 (1976) 316.

[3] HOSEA, J., BERNABEI, S., COLESTOCK, P., DAVIS, S.L., EFTHIMION, P., et al., Phys. Rev. Lett. 43 (1979) 1802; HWANG, D., ARUNASALAM, V., BERNABEI, S., BITTER, M., BOYD, D., in Controlled Fusion and Plasma Physics (Proc. 9th Europ. Conf., Oxford, 1979).

[4] TFR GROUP, in Controlled Fusion and Plasma Physics (Proc. 9th Europ. Conf., Oxford, 1979).

[5] JACQUINOT, J., in Heating in Toroidal Plasmas (Proc. Joint Varenna-Grenoble Int. Symp. Grenoble, 1978) Vol. I (1978) 127.

[6] KIMURA, H., ODAJIMA, K., SENGOKU, S., IIZUKA, S., SUGIE, T., et al., ICRF Heating in DIVA: Parameter Survey and Very High Efficiency Ion Heating Experiment, JAERI-M 8429 (1979).

[7] HSUAN, H., HAWRYLUK, R.J., SUCKEWER, S., TAKAHASHI, H., 3rd Topical Conf. on RF Plasma Heating (Pasadena) C8-1 (1978).

[8] DIVA GROUP, Nucl. Fusion 18 (1978) 1619.

[9] TAJIMA, T., Particle and Energy Balances in Tokamak Plasmas, Japan Atomic Energy Research Institute Report JAERI-M 7717 (1978) [in Japanese].

[10] GALEEV, A.A., and SAGDEEV, R.Z., Sov. Phys. JETP 26 (1968) 233.

[11] IIZUKA, S., ODAJIMA, K., KIMURA, H., DIVA DIAGNOSTICS·OPERATIONAL GROUP, Propagation and Absorption of the Fast Magnetosonic Wave near the Two-Ion Hybrid Resonance Layer, Japan Atomic Energy Research Institute Report JAERI-M 8595 (1979) [to be published in Phys. Rev. Lett.].

[12] STIX, T.H., Nucl. Fusion 15 (1975) 737.

Table 1 Power balances with and without the RF power for the case of B_T = 18 kG and $\varepsilon_p \sim 15$ % and without the Faraday shield. The method of the measurement of each loss power is described in Chapter 5.

Loss (kW)	Conduction-Convection		Radiation and Charge-exchange	Total loss	P_{Net}
	to shell	to divertor			
without RF	35	20	15	70	
with RF	55	40	15	110	40

Table 2 Heating efficiency derived from equations (6) and (7). A, B and C indicate the heating conditions.

Pair of data	A, B	A, C
α	$\sim$2.3	$\sim$4.6
β	0.35 $\sim$ 0.53	0.18 $\sim$ 0.27
η_A (%)	61 $\sim$ 77	78 $\sim$ 85
η_B (%)	27 $\sim$ 33	
η_C (%)		17 $\sim$ 19

A: ε_p = 5$\sim$10 % with Faraday Shield

B: ε_p = 5$\sim$10 % without Faraday Shield

C: $\varepsilon_p \sim$ 15 % without Faraday Shield

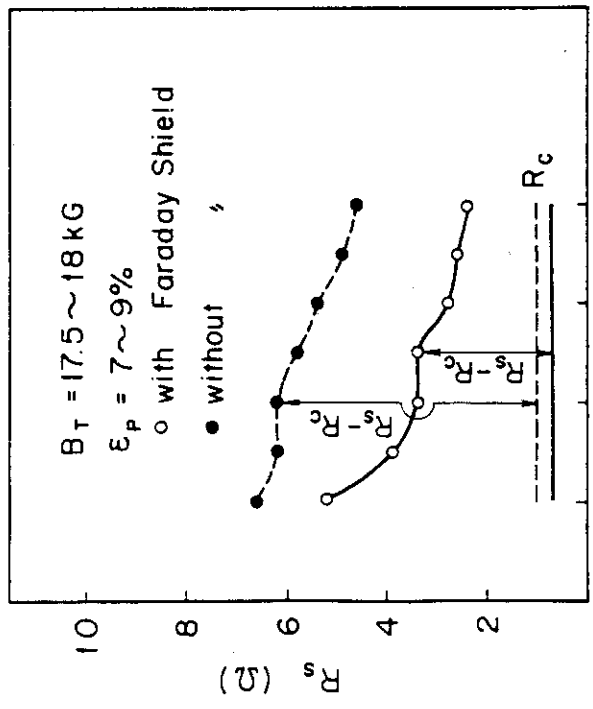

Fig. 1 Comparison of time evolutions of the antenna loading impedance R_s between the cases with and without the Faraday shield. R_c is the circuit loss.

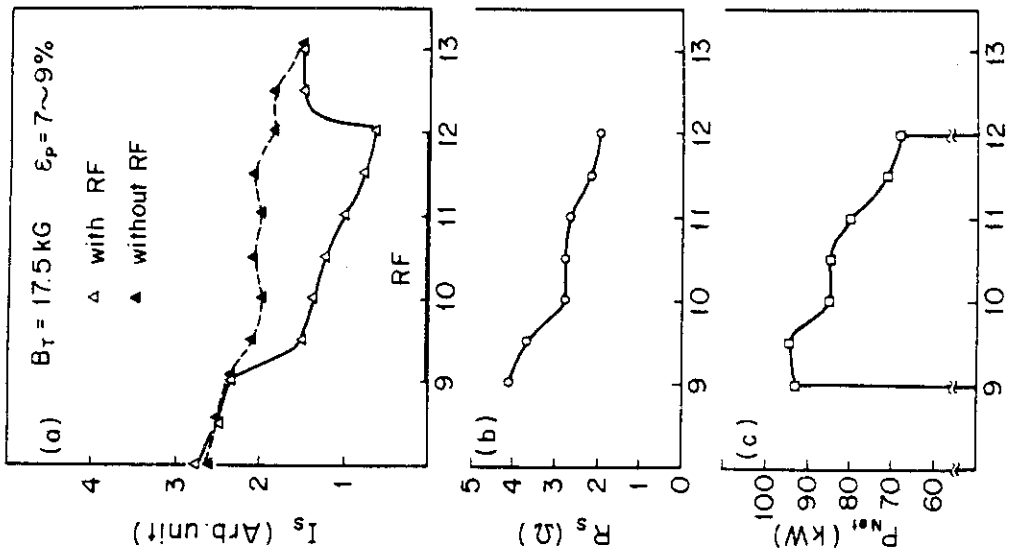

Fig. 2 Time evolutions of (a) ion saturation current, I_s, in the divertor region at R = 40 cm, Z = -6 cm (b) antenna loading impedance, R_s, and (c) resulting reduction of the RF net power, P_{Net}.

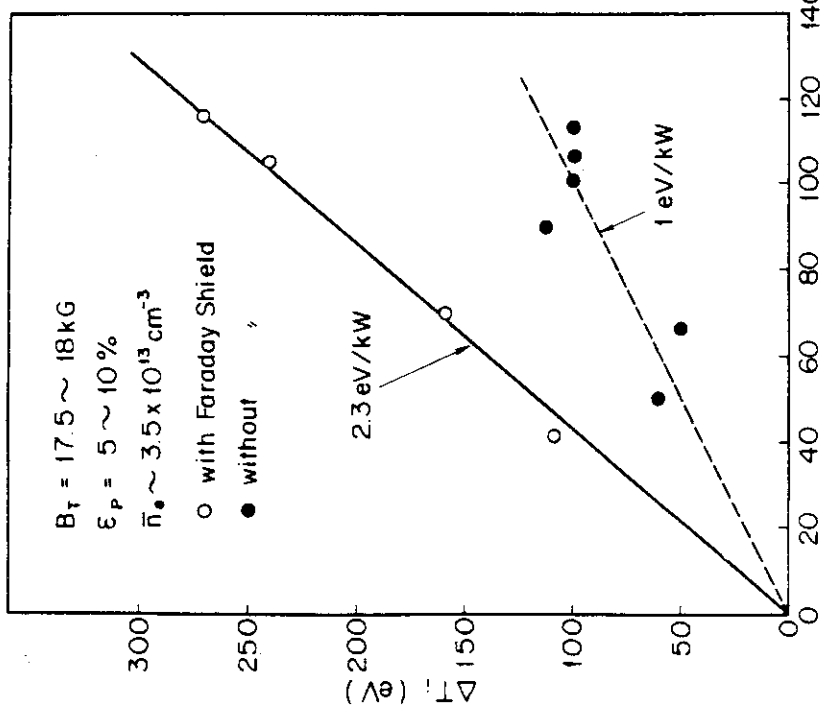

Fig. 3 Bulk ion temperature increase, ΔT_i, versus RF net power, P_{Net}, for the cases with and without the Faraday shield.

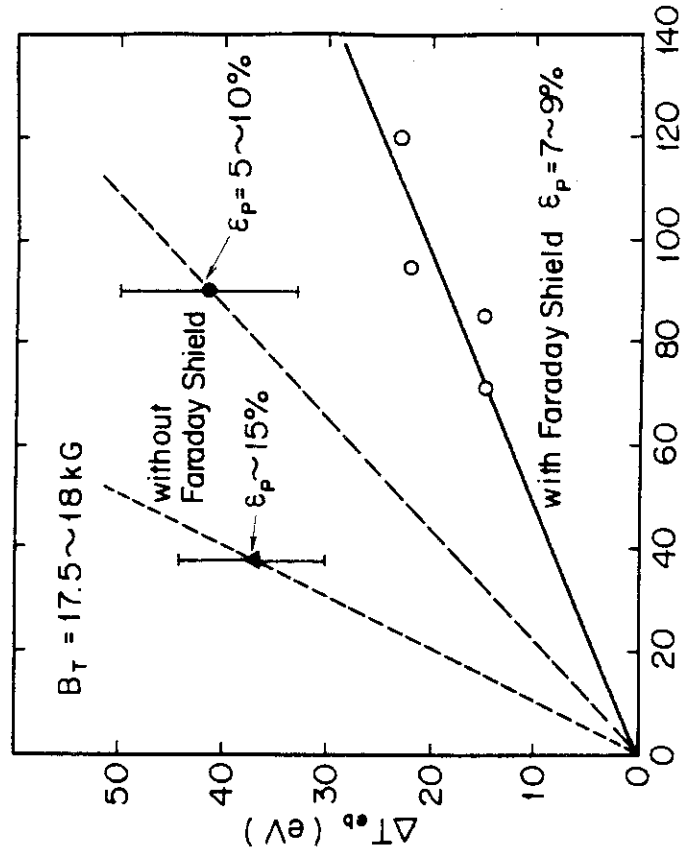

Fig. 4 Boundary electron temperature increase, ΔT_{eb}, versus RF net power, P_{Net}, for the cases with and without the Faraday shield.

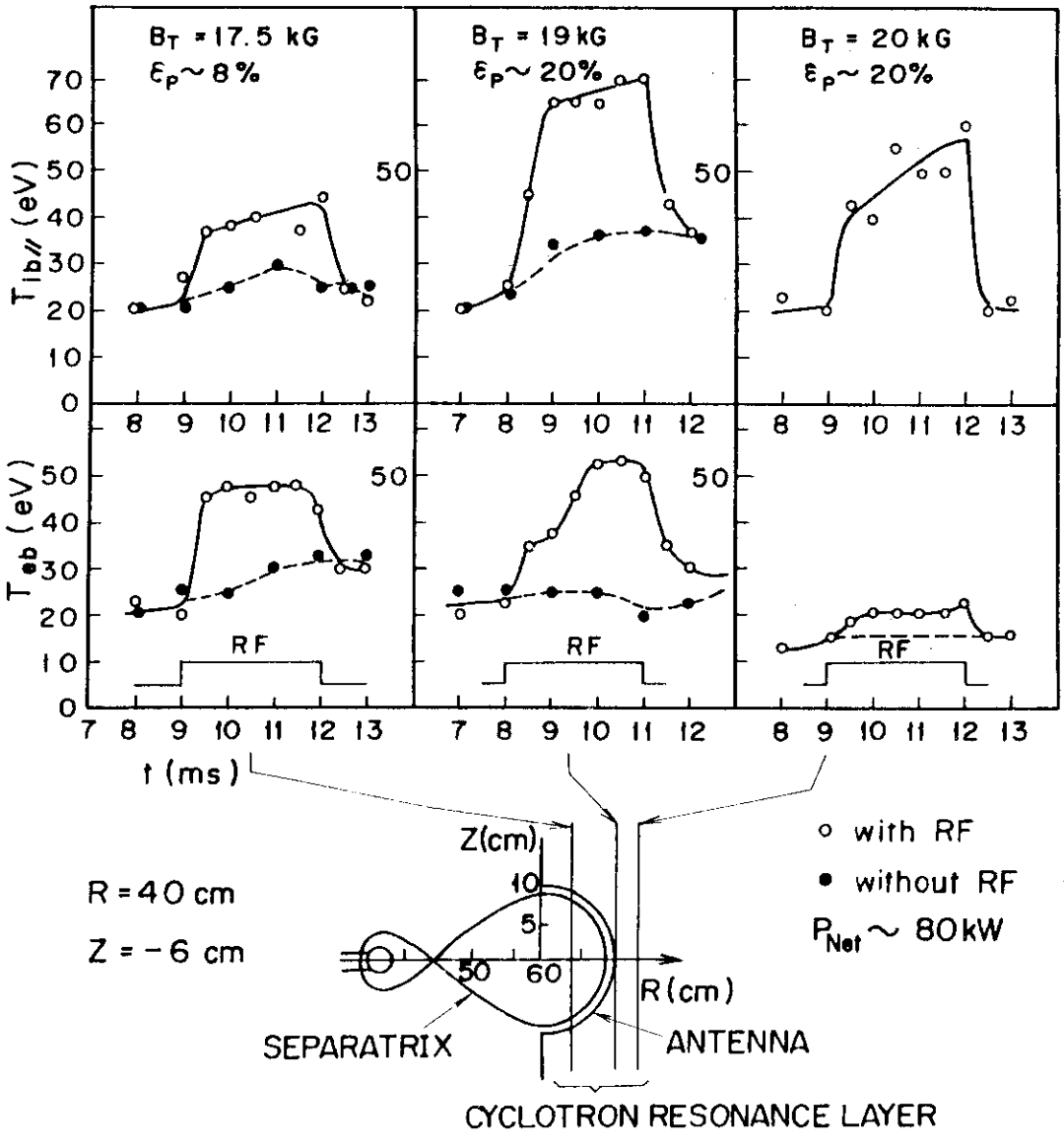

Fig. 5 Time evolutions of the boundary ion and electron temperatures for various toroidal magnetic fields, in the case with the Faraday shield. These were measured by the multigrid energy analyzer placed at R = 40 cm and Z = −6 cm.

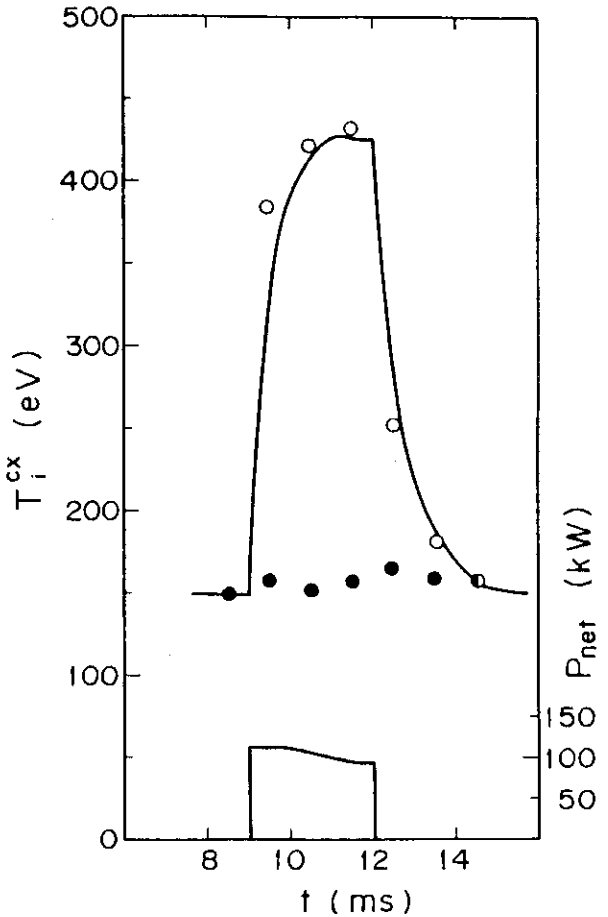

Fig. 6 Time evolutions of the perpendicular ion temperature measured by the charge-exchange neutral energy analyzer; o with RF heating, ● without RF heating. B_T = 17.5 kG, $\varepsilon_p \sim 9$ % $\bar{n}_e \sim 3.5\times10^{13}$ cm^{-3} and $P_{Net} \sim 115$ kW. The solid line is the result of the numerical simulation, assuming the indicated time variation of the RF input power and the heating efficiency of 83 %.

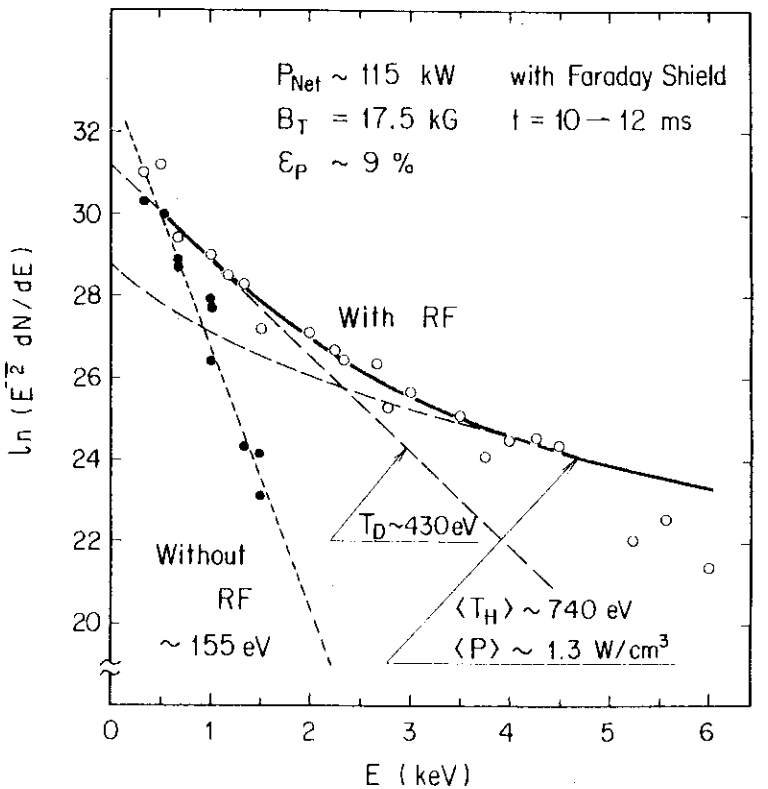

Fig. 7 Energy spectra of charge-exchange neutrals consisting of deuterium and hydrogen components for the same condition of Fig. 6. The solid lines are calculated from the sum of one-component Maxwell distribution for deuteriums and the Stix's formula for hydrogens, assuming T_e = 330 eV, $n_e = 7\times10^{13}$ cm^{-3} and Z_{eff} = 1.

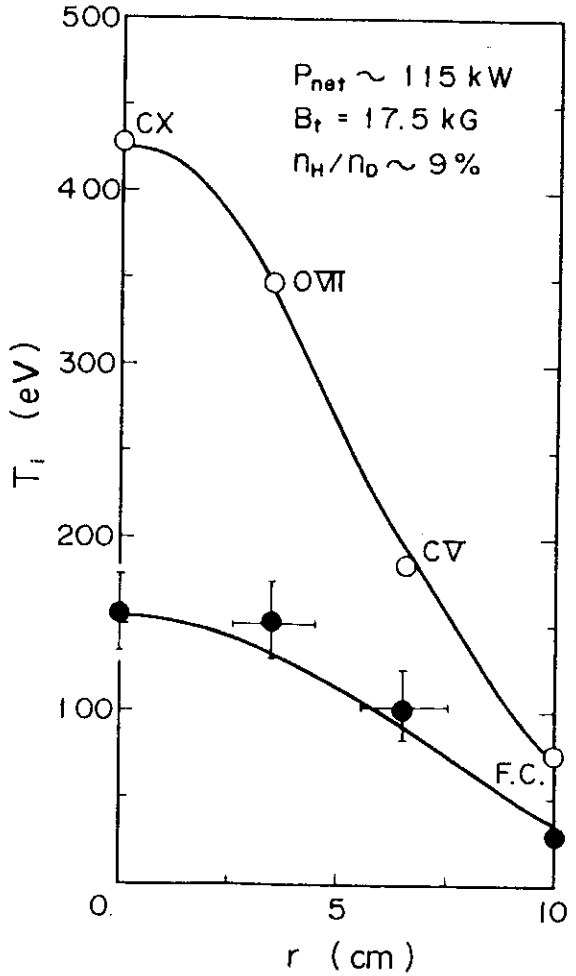

Fig. 8 Radial profiles of the ion temperature obtained by combining data of the charge-exchange neutral, the impurity Doppler broadening and the multigrid energy analyzer (Faraday cup) at 11∿12 ms; ○ with RF, ● without RF. The solid line is the result of the numerical simulation.

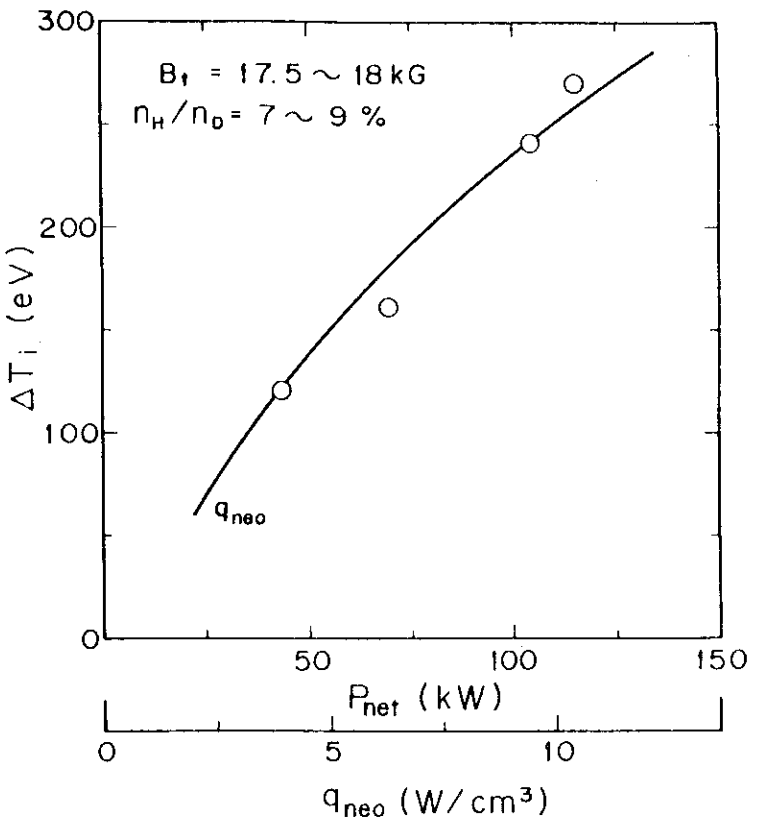

Fig. 9 Bulk ion temperature increase ΔT_i versus RF net power. B_T=17.5 kG, ε_p=7∿9 % and $\bar{n}_e \sim 3.5\times10^{13}$ cm^{-3}. The solid curve is a neoclassical heat conduction loss power density near the center of the plasma column, q_{neo}, as a function of ΔT_i.

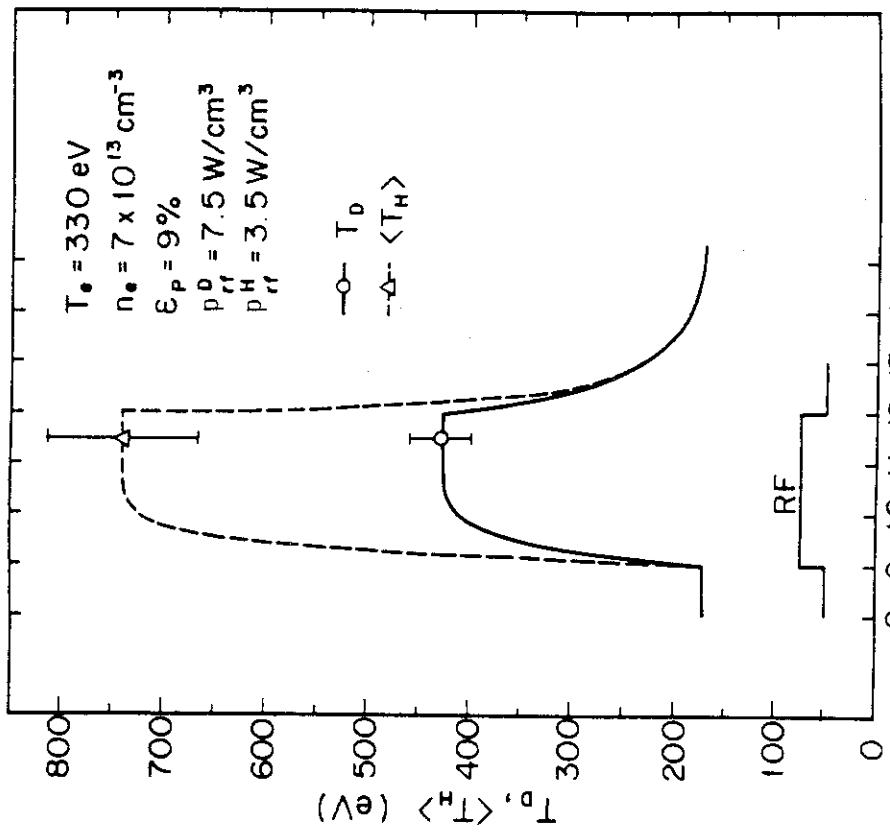

Fig.11 Calculation of the time evolution of the deuteron and proton temperature from the point-model power balance equations (8) and (9).

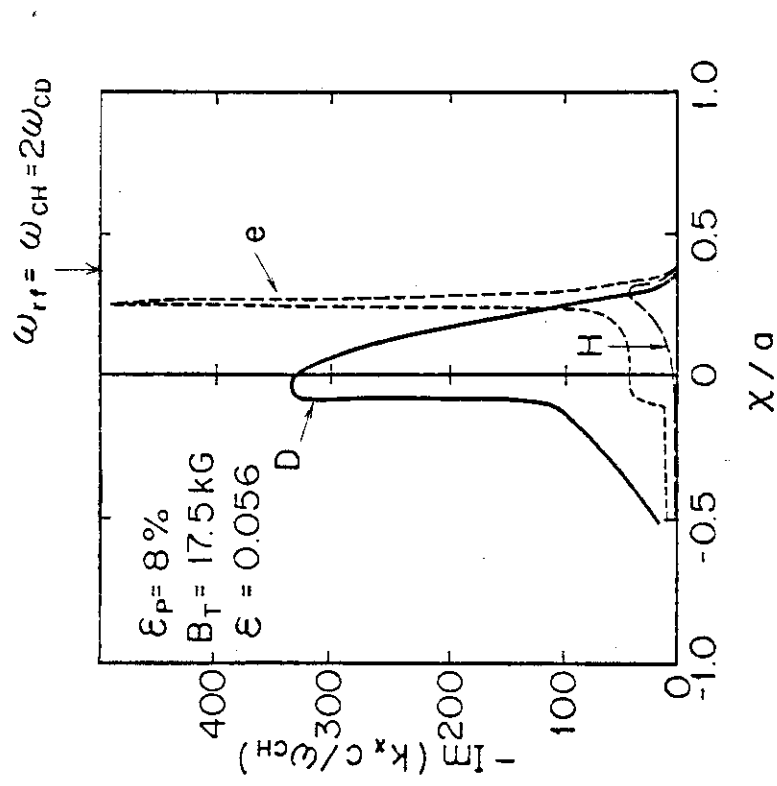

Fig.10 Damping decrement of the slow electrostatic mode by each species along the major radius direction for the case of ε_p = 8 %, B_T = 17.5 kG and ε = 0.056, ε[5] is a parameter indicating a role of a rotational transform.

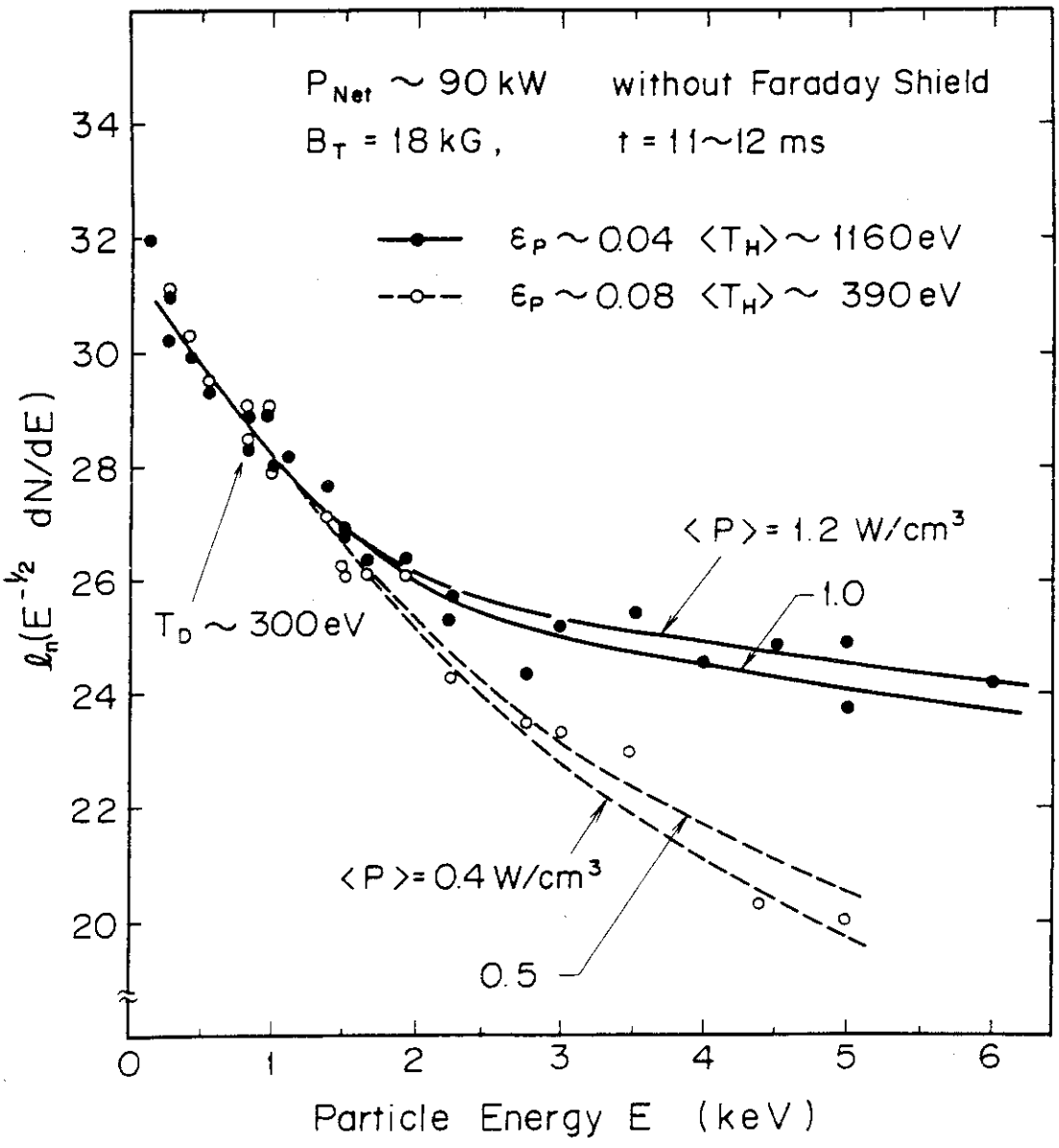

Fig.12 Comparison of charge-exchange neutral spectra for $\varepsilon_p \sim 4$ % (closed circles) and $\varepsilon_p \sim 8$ % (open circles). The solid and broken lines are calculated similarly to Fig. 7.

6.3 Summary

The ICRF heating experiment using 2 ω_{CD} frequency for a deuteron plasma with a minority proton component was performed under the extremely pure wall condition ($Z_{eff} \simeq 1$). The optimum heating conditions were surveyed, varying the toroidal magnetic field, B_T, and the proton-to-deuteron density ratio, ε_p. The most favourable majority deuteron heating was observed for the case of B_T = 17.5 ∿ 18 kG and ε_p = 5 ∿ 10 %. The result was well explained by the mode conversion theory. Heating efficiency, however, was only up to 40 %. The rest of the RF power went to the edge plasma by the electrostatic coupling between the antenna and the edge plasma.

In the next stage, the antenna was electrostatically shielded by the full Faraday shield. The power balances were investigated by the following approaches:

(1) The partition of the heating power to the core and boundary plasmas was determined from the measurement of the antenna loading impedance and the boundary plasma.

(2) The experimental time evolution and radial profile of the bulk ion temperature were compared with the 1-D tokamak simulation assuming the rectangular power deposition profile and the heating efficiency.

(3) The heating powers to majority and minority components were evaluated from the point-model power balance equation.

In the case with the Faraday shield and of B_T = 17.5 kG, ε_p ∿ 9 %, $\bar{n}_e$ ∿ 3.5 × 10^{13} cm^{-3} and P_{Net} ∿ 115 kW, we observed T_D ∿ 430 eV and $\langle T_H \rangle$ ∿ 740 eV from the base ion temperature of 160 eV.
The following results have been obtained:

(1) The antenna loading impedance became less than half of that without the Faraday shield. The loading impednace decreased with decreasing edge density irrespective of the Faraday shield.

(2) About 80 % of the RF net power was coupled to the majority deuterons in the core plasma.

(3) The heating power densities to deuterons and protons were respectively 7.5 W/cm^3 and 3.5 W/cm^3; the result is consistent with that of (2) if we take into account the D-H power transfer.

(4) The ratio of the heating powers to majority and minority components can be controlled by selecting the value of ε_p.

(5) The behaviour of the RF-heated ions were well explained by the neoclassical transport theory within a factor of three, even in application of the RF power density ten times larger than the power transferred from electrons to ions in the absence of the RF power.

ACKNOWLEDGEMENTS

The author would like to express his sincere gratitude to Professor Kuniya Fukuda of Kyoto University whose continuous encouragement, support and advice have been invaluable.

The author also wishes to express his appreciation to Professor Hiroshi Nishihara of Kyoto University for his enthusiastic encouragement and advice.

Thanks are also due to Professor Atsuo Iiyoshi of Kyoto University for his advice and criticism.

The support of the members of the DIVA Group of the Japan Atomic Energy Research Institute is gratefully acknowledged. In particular, the excellent guidances by Drs. Yasuo Shimomura and Hikosuke Maeda were fundamental to this work. Discussions and cooperations with Drs. Hideo Ohtsuka, Shin Yamamoto, Kazuo Odajima, Masayuki Nagami, Seio Sengoku, Kazumi Ohasa, Toshiaki Matsuda and Hiroshi Matsumoto were extremely useful and fruitful.

Specifically, the author is much indebted to Drs. K. Odajima and Tatsuo Sugie for the measurement of the ion temperature in the scrape-off layer in Chapter 2; to Drs. H. Ohtsuka, S. Yamamoto, S. Sengoku and Masashi Azumi for cooperation in the investigation of the scrape-off layer plasma in Chapter 3; to Dr. Noriaki Ueda of the Mitsubishi Atomic Power Industry and Drs. Masahiro Seki and Hiroshi Kawamura of the Division of Reactor Engineering, for the development of the thermometer and the measurement by the thermometer in Chapter 4; to Drs. K. Odajima and Makoto Shiho for the measurement of the radiation loss and the coworks in the investigation of the gross power balance in Chapter 5; finally, in Chapter 6, to Dr. K. Odajima and Dr. Satoru Iizuka of Tohoku University for valuable discussions on experiment and theory of the ICRF Heating, to Dr. Akimasa Funahashi for the arrangements of various diagnostics, to the late Mr. Koki Takahashi and Dr. Hiroshi Takeuchi for the measurement by the charge-exchange neutral analyser, to Dr. T. Sugie for the measurement of the impurity Doppler broadening, to Mr. Katsuaki Kumagai and Dr. Toshihiko Yamauchi for the measurement by laser scattering, to Drs. M. Azumi and Toshio Hirayama for the analysis of the experimental results, to Drs. Takashi Nagashima and S. Sengoku and Messrs. Katsuto Anno and Takatoshi Shibata for the construction of the ICRF generator, and to Drs. K. Ohasa and Akira Nagashima for helps with the construction of the stub tuner.

It is a pleasure to thank Messrs. Toshikuni Tokutake and K. Anno and the other members of the operational group of DIVA for the excellent support in the experiment.

The author would like to thank Dr. Masayuki Fukao of the University of California Los Angeles, who first introduced him to the thermonuclear field, for his continuous encouragement and enthusiasm.

Finally, the author would like to express his appreciation to Drs. Yuji Tanaka, Masatoshi Tanaka, Yukio Obata and Shigeru Mori of the Japan Atomic Energy Research Institute for their continuous suppors and encouragements.

PUBLICATION LIST

Chapter 2

(1) KIMURA, H., ODAJIMA, K., SUGIE, T., MAEDA, H.,
Application of Multigrid Energy Analyzer to the Scrape-Off Layer Plasma in DIVA, Jpn. J. Appl. Phys. 18 (1979) 2281.

(2) KIMURA, H., NAGAMI, M., YAMAMOTO, S., UEDA, N., OHTSUKA, H., et al.,
Diagnostics of a Scrape-Off Layer Plasma, JAERI-M 6971 (1977).

Chapter 3

(1) KIMURA, H., OHTSUKA, H., MAEDA, H., SHIMOMURA, Y., YAMAMOTO, S., et al.,
Electrostatic Diagnostics of JFT-2a (DIVA), JAERI-M 6861 (1977).

(2) OHTSUKA, H., KIMURA, H., SHIMOMURA, Y., MAEDA, H., YAMAMOTO, S., et al.,
Probe Measurements in the Scrape-Off Layer of a Tokamak, Plasma Physics, 20 (1978) 749.

(3) ODAJIMA, K., KIMURA, H., MAEDA, H., OHASA, K.,
Jpn. J. Appl. Phys. 17 (1978) 1281.

Chapter 4

KIMURA, H., MAEDA, H., UEDA, N., SEKI, M., KAWAMURA, H., et al.,
Heat Flux to the Material Surfaces in a Tokamak, Nucl. Fusion 18 (1978) 1195.

Chapter 5

ODAJIMA, K., MAEDA, H., SHIHO, M., KIMURA, H., YAMAMOTO, S., et al.,
Radiation Loss and Power Balance in DIVA, Nucl. Fusion 18 (1978) 1337.

Chapter 6

(1) KIMURA, H., ODAJIMA, K., SENGOKU, S., OHASA, K., SUGIE, T., et al.,
ICRF Heating of a D^+ Plasma with a Minority H^+ Component in DIVA, Nucl. Fusion 19 (1979) 1499.

(2) KIMURA, H., ODAJIMA, K., SENGOKU, S., IIZUKA, S., SUGIE, T., et al.,
ICRF Heating in DIVA: Parameter Survey and Very High Efficiency Ion Heating Experiment, JAERI-M 8429 (1979).

(3) ODAJIMA, K., KIMURA, H., IIZUKA, S., SUGIE, T., TAKAHASHI, K., et al., High Efficiency ICRF Heating in DIVA, to be published in Nucl. Fusion.

(4) KIMURA, H., ODAJIMA, K., IIZUKA, S., SENGOKU, S., SUGIE, T., et al., High Efficiency ICRF Heating Experiment in DIVA, to be presented at the 8th Int. Conf. on Plasma Physics and Controlled Nuclear Fusion Research, Brussels, 1-10 July 1980.